:: csem

unine
UNIVERSITÉ DE
NEUCHÂTEL

Fabrication and characterization of MEMS alkali vapor cells used in chip-scale atomic clocks and other atomic devices

Sylvain Karlen

IMPRIMATUR POUR THESE DE DOCTORAT

**La Faculté des sciences de l'Université de Neuchâtel
autorise l'impression de la présente thèse soutenue par**

Monsieur Sylvain KARLEN

Titre:

" Fabrication and characterization of MEMS alkali vapor cells used in chip-scale atomic clocks and other atomic devices "

sur le rapport des membres du jury composé comme suit:

- Prof. Gaetano Mileti, directeur de thèse, Université de Neuchâtel, Suisse
- Prof. Nico de Rooij, EPFL, Neuchâtel, Suisse
- Dr John Kitching, NIST, Boulder, Colorado, United States
- Dr Steve Lecomte, CSEM, Neuchâtel, Suisse
- Dr Pierre Waller, ESA-ESTEC, Noordwijk, Netherlands
- Dr Christoph Affolderbach, Université de Neuchâtel, Suisse
- Dr Jacques Haesler, CSEM, Neuchâtel, Suisse

Neuchâtel, le 25 janvier 2018   Le Doyen, Prof. R. Bshary

Abstract

Atomic clocks are timekeeping devices that can achieve extreme performance in terms of stability and accuracy. Behind this name, hides a variety of different systems which size and complexity can be considerably different depending on their applications. The primary frequency standards used for the realization of the second and the clocks mounted on the Galileo satellite positioning system are two well-known examples.

In recent years, considerable efforts lead to miniaturization and reduction of the power consumption of such systems, giving rise to the first chip-scale atomic clocks (CSACs). The performance of these devices is potentially superior to high-performance quartz of comparable size. Their manufacturing is made possible by the use of micro-technology-specific manufacturing processes techniques and the use of a purely optical interrogation scheme called coherent population trapping (CPT). At the heart of a CPT clock is the micro-fabricated (MEMS) cell. It consists of a sealed cavity having an optical access and containing an alkali metal vapor as well as a buffer gas. It should however be noted that the use of such MEMS cells is not limited to CSACs but can be extended to other atomic sensors such as atomic gyroscopes and atomic magnetometers.

The present thesis deals with two main subjects of study concerning micro-manufactured atomic cells. First, various aspects related to cells fabrication are reviewed and new micro-fabrication techniques are studied. In a second step, the performances of atomic cells manufactured with these techniques are measured for their use in CSACs and atomic gyroscopes.

The first micro-fabrication technology proposed here is the application of copper-copper thermo-compression as an alternative hermetic sealing technology. This method allows to overcome some of the limitation inherent to the established anodic bonding. By limiting the cavity contamination and allowing the bonding of other alternative materials, it potentially allows to lengthen the cell lifetime and improve the long-term clock frequency stability. In particular a preliminary study on the manufacturing of the sapphire-sapphire cells is presented and a study of the residual gas contamination inside the cavity is realized.

The second technique of micro-fabrication presented here is the application of an aluminum oxide coating on the inner walls of the cells. This coating allows to reduce the reaction between the alkali metal and the cell walls and to improve their lifetime which is particularly interesting in the case of cells filled by UV-decomposed rubidium azide for which the amount of alkali metal is limited. In this context, a new method for measuring the partial pressure of nitrogen by Raman spectroscopy is presented and compared with a similar measurement carried out by atomic spectroscopy. The results made with this novel technique are used in a lifetime study of cells filled by rubidium azide decomposition and sealed by anodic bonding.

The use of rubidium micro-pills as an alkali metal source is then studied. Cells filled with this method are characterized with respects to their application in CSACs. In particular, a new argon-neon buffer gas mixture developed for this filling method is assessed and the dependence of the atomic frequency to the temperature and its thermal inversion point are studied.

The latest technology studied here is the use of gold micro-disks as preferential nucleation sites for rubidium. By condensing the rubidium out of the laser light-path, these micro-structures prevent the

migration of alkali metal droplets and the induced clock frequency instabilities. Long-term stability studies are therefore presented to highlight this phenomenon and demonstrate the effectiveness of this technology.

Finally, a preliminary characterization of the Xe relaxation time in MEMS cells in presented in view of their use in atomic gyroscopes.

Keywords:

Alkali metal atomic vapor cells, rubidium, microfabrication, atomic clocks, atomic spectroscopy, Raman spectroscopy, image analysis, buffer gas, MEMS, CSAC, atomic gyroscope

Résumé

Les horloges atomiques sont des gardiens de temps pouvant atteindre des performances extrêmes en termes de stabilité et de précision. Sous ce terme, se cache cependant une grande variété de systèmes très différents dont la taille et la complexité peuvent varier considérablement en fonction de leurs applications. On citera par exemple les étalons primaires de fréquence utilisés pour la réalisation de la seconde ou les horloges embarquées dans le système de positionnement par satellite Galileo.

Ces dernières années, des efforts importants de miniaturisation et de réduction de la consommation ont donné naissance aux toutes premières horloges atomiques miniatures dont les performances sont potentiellement supérieures à des quartz de haute performance de taille comparable. La fabrication de telles horloges est rendue possible par l'utilisation de techniques de fabrication spécifiques à la micro-technologie et d'un schéma d'interrogation purement optique appelé piégeage cohérent de population. La partie centrale d'une telle horloge est la cellule micro-fabriquée. Celle-ci consiste en une cavité ayant un accès optique et contenant une vapeur de métal alcalin ainsi qu'un gaz tampon. On notera en outre que leur utilisation n'est pas limitée aux horloges miniatures, mais peut être étendue à d'autres senseurs atomiques tels que les gyroscopes atomiques et les magnétomètres atomiques.

La présente thèse de doctorat s'articule autour de deux principaux sujets d'étude concernant les cellules atomiques micro-fabriquées. Premièrement, différents aspects liés aux techniques de micro-fabrications sont passées en revue et de nouvelles techniques sont étudiées. Dans un second temps, les performances de cellules atomiques fabriquées selon ces techniques sont mesurées afin d'évaluer leur utilisation en micro-horloge ainsi qu'en gyroscope.

La première technologie de micro-fabrication proposée ici est l'application de la thermocompression cuivre-cuivre comme méthode alternative à la soudure anodique pour le scellage hermétique. Cette technique permet de réduire les contaminations internes à la cavité ainsi que d'utiliser des matériaux différents que le silicium et le borosilicate comme constituants de la cellule, allongeant potentiellement leur durée de vie et leur stabilité sur le long-terme. La contamination gazeuse des cellules scellées par thermocompression cuivre-cuivre est en particulier étudiée et une étude préliminaire sur la fabrication de cellules saphir-saphir est présentée.

La deuxième technique de micro-fabrication étudiée est l'application d'un revêtement d'oxyde d'aluminium sur les parois intérieures des cellules. Celle-ci permet de réduire la réaction entre le métal alcalin et les parois des cellules et/ou d'agir comme barrière étanche entre la cavité et le verre et l'extérieur et ainsi d'améliorer leur durée de vie. Cette technologie est en particulier utilisée dans le cas de cellules remplies par décomposition d'azoture de rubidium pour lesquelles la quantité de métal alcalin est limitée. Dans ce cadre, une nouvelle méthode de mesure de la pression partielle d'azote par spectroscopie Raman est présentée et comparée à une mesure similaire réalisée par spectroscopie atomique. Ces résultats sont utilisés dans le cadre d'une étude de durée de vie de cellules remplies par cette méthode et scellées par soudure anodique.

L'utilisation de micropilules rubidium comme source de métal alcalin est ensuite étudiée. Des cellules de ce type sont caractérisées selon plusieurs aspects. En particulier un nouveau mélange de gaz tampon argon-néon développé pour cette méthode de remplissage est examinée et la dépendance de la fréquence atomique à la température et le "point d'inversion" thermique sont étudiés.

La dernière technologie décrite est l'utilisation de micro-disques en or comme point de nucléation du rubidium. En condensant le rubidium hors du chemin optique du laser, ceux-ci permettent d'éviter la migration de gouttelettes de métal alcalin et les instabilités de fréquence d'horloges induites. Des études de stabilité long-terme sont présentées pour mettre en évidence phénomène et prouver l'efficacité de cette technologie.

Finalement, une étude préliminaire sur le temps de relaxation du xénon dans des cellules micro-fabriquées est présentée en vue de leur utilisation dans des gyroscopes atomiques.

Mots clés :

Cellules atomiques à vapeur de métal alcalin, rubidium, micro-fabrication, horloges atomiques, piégeage cohérent de population, spectroscopie atomique, spectroscopie Raman, analyse d'image, gaz tampon, gyroscopes atomiques

Acknowledgement

I would like to thank all the people who have helped, guided, advised or supported me, directly or indirectly, during the realization and the writing of this thesis:

- First and foremost, I would like to express my sincere gratitude to Dr. Jacques Haesler and Dr. Steve Lecomte, my supervisors at CSEM where I performed most of my research. Their availability, enthusiasm and expertise helped me in all the time of research and writing of this thesis. I could not have imagined having better advisors and mentors for my PhD study.

- My sincere thanks goes to my thesis director and supervisor at the University of Neuchâtel, Prof. Gaetano Mileti, for the continuous support of my study and related research, for his advices and great knowledge. His guidance greatly helped me in the structuring of my research and writing of this thesis.

- Besides my supervisors, I would like to thank the rest of my thesis experts committee: Prof. N. de Rooij, Dr. John Kitching, Dr. Pierre Waller and Dr. Christoph Affolderbach , for their insightful comments and encouragement, but also for the questions which encouraged me to widen my research from various perspectives.

- A very special thank goes to my colleagues from the Time and Frequency sector at CSEM and in particular Dr. Laurent Balet, Dr. Gilles Buchs, Dr Dmitri Boiko and Dr. Stefan Kunderman whose availability, kindness and motivation helped me with the technical aspects of my thesis and more generally all my colleagues from the Systems division at CSEM.

- I would also like to show my gratitude to Dr. Thomas Overstolz and Dr. Jean Gobet who supervised and guided me through all the technical aspects of MEMS fabrication and characterization. Their huge expertise in the domain allowed to orient my research in a much faster path toward its goal. The results presented here could not have been obtained without their help.

- A special thank also goes to the technical staff of the clean room and to my other colleagues of the Micro & Nano Systems division at CSEM in particular Giovanni Bergonzi but also Mehretab Amine, Florence Rigoletti, Sylviane Pochon, Pierre-André Clerc, Stéphane Ischer, Angélique Bionaz, Dr. Mohammad Mehdi Dadras, Silvia Biselli and Dr. Kaushik Vaideeswaran. Their knowledge and availability was an invaluable help.

- During my stay at ESTEC, I had the chance to collaborate with the time and frequency best-in-class people in the space domain. Thereby, I would like to thank Dr. Pierre Waller and Marco Belloni but also Dr. Piero Angeletti and the other members of the RF Equipment & Technology Section at ESA ESTEC for their warm welcome and the vast experience they shared with me during the three months I spent with them.

- During my PhD study, I also had the chance to collaborate directly with the members of the Time and Frequency Laboratory at the Universtiy of Neuchâtel and to use their research facilities. Thereby, I would like to thank Dr. Matthieu Pellaton, Dr. Renaud Matthey, Dr. Stéphane Schilt, Mohammadreza Gharavipour and William Moreno for the experience they shared with me and for the fruitful discussion we had.

- Last but not least, I want to thank my family and my friends (some are also colleagues) for their support, love and affection through the years spent on my PhD study but also before and after that.

Sylvain Karlen

Contents

List of Figures

List of Tables

Author's contribution

Articles in peer-reviewed journals

[1] S. Karlen, J. Gobet, T. Overstolz, J. Haesler, and S. Lecomte. Lifetime assessment of RbN$_3$-filled MEMS atomic vapor cells with Al$_2$O$_3$ coating. *Optics express*, 25(3):2187–2194, 2017.

[2] S. Karlen, J. Gobet, T. Overstolz, J. Haesler, and S. Lecomte. Quantitative micro-Raman spectroscopy for partial pressure measurement in small volumes. *Applied Spectroscopy*, 71(12):2707–2713, 2017.

International conferences with proceedings

[1] S. Karlen, J. Gobet, T. Overstolz, and J. Haesler. Non-destructive MEMS atomic vapor cells characterization by Raman spectroscopy and image analysis. In *29th European Frequency and Time Forum (EFTF)*, York, United Kingdom, 2016. IEEE.

[2] S. Karlen, J. Haesler, T. Overstolz, G. Bergonzi, and S. Lecomte. Cu-Cu thermocompression bonding as an innovative sealing method for MEMS atomic vapor cells. In *ESA Workshop on Microwave Technology and Techniques (MTT)*, Noordwijk, The Netherlands, 2017.

[3] S. Karlen, G. Buchs, T. Overstolz, N. Torcheboeuf, E. Onillon, J. Haesler, and D. Boiko. MEMS atomic vapor cells for gyroscope applications. In *International Frequency Control Symposium (IFCS), Joint with the 31st European Frequency and Time Forum (EFTF)*, pages 315–316, Besançon, France, 2017.

[4] S. Karlen, J. Haesler, T. Overstolz, G. Bergonzi, and S. Lecomte. MEMS atomic vapor cells sealed by Cu-Cu thermocompression bonding. In *International Frequency Control Symposium (IFCS), Joint with the 31st European Frequency and Time Forum (EFTF)*, pages 625–627, Besançon, France, 2017.

[5] J. Haesler, K. Kautio, L. Balet, S. Karlen, T. Overstolz, and B. Gallinet. Ceramic based flat form factor miniature atomic clock physics package (C-MAC). In *ESA Workshop on Microwave Technology and Techniques (MTT)*, Noordwijk, The Netherlands, 2017.

[6] J. Haesler, K. Kautio, L. Balet, S. Karlen, T. Overstolz, and B. Gallinet. Ceramic based flat form factor miniature atomic clock physics package (C-MAC). In *International Frequency Control Symposium (IFCS), Joint with the 31st European Frequency and Time Forum (EFTF)*, pages 55–56, Besançon, France, 2017.

[7] G. Buchs, S. Karlen, T. Overstolz, N. Torcheboeuf, E. Onillon, J. Haesler, and D. Boiko. Nuclear spin decoherence time in MEMS atomic vapor cells for applications in quantum technologies. In *4th International Conference on Quantum Technologies (ICQT)*, Moscow, Russia, 2017.

[8] J. Haesler, L. Balet, S. Karlen, T. Overstolz, B. Gallinet, S. Lecomte, F. Droz, K. Kautio, P. Karioja, and M. Lahti. Ceramic based flat form factor miniature atomic clock physics package (C-MAC). In *6th International Colloquium on Scientific and Fundamental Aspects of GNSS / Galileo*, Valencia, Spain, 2017.

Articles in preparation

[1] S. Karlen, J. Gobet, F. Droz, T. Overstolz, J. Haesler, and S. Lecomte. Reduction of light-shift induced long-term frequency instabilities in alkali vapor cell clock by Au microdiscs.

[2] S. Karlen, J. Haesler, T. Overstolz, G. Bergonzi, and S. Lecomte. Rubidium MEMS atomic vapor cells sealing by Cu-Cu thermocompression bonding.

Abbreviations

AM	Amplitude modulation
BHF	Buffered hydrofluoric acid
CAD	Computer aided design
C-MAC	Ceramic miniature atomic clock
CMOS	Complementary metal-oxide-semiconductor
CO	Cross-over
CPT	Coherent population trapping
CSAC	Chip-scale atomic clock
CSEM	Centre suisse d'électronique et de microtechnique
CTE	Coefficient of thermal expansion
DBR	Distributed Bragg reflector
DFB	Distributed feedback laser
DC	Direct current
DRIE	Deep reactive ion etching
ESA	European space agency
ESTEC	European space research and technology center (ESA)
FFT	Fast Fourier transform
FIB	Focused ion beam
FM	Frequency modulation
FoM	Figure of merit
FWHM	Full width at half maximum
KOH	Potassium hydroxide
LS	Light-shift
LTCC	Low temperature co-fired ceramic
LTF	Laboratoire temps-fréquence (University of Neuchâtel)
MAC	Miniature atomic clock
MAC-TFC	MEMS atomic clocks for timing, frequency control and communications
MEMS	Microelectromechanical system
mTS	Miniaturized Timing Source
MVD	Molecular vapor deposition$^{®}$
NEG	Non evaporable getters
NIST	National institute of standards and technology

NMP	N-Methyl-2-pyrrolidone
NMR	Nuclear magnetic resonance
NMRG	Nuclear magnetic resonance gyroscope
NTC	Negative temperature coefficient (thermistor)
OCXO	Oven-controlled crystal oscillator
PD	Photodiode (or photodetector)
PER	Polarization extinction ratio
PID	Proportional integral derivative (controller)
PP	Physics package
RF	Radio frequency
RIE	Reactive ion etching
RQ	Requirement
SEM	Scanning electron microscope
SEOP	Spin-exchange optical pumping
SMSR	Side mode suppression ratio
SOA	State-of-the-art
TLP	Transient liquid phase
TN	Technical note
TTV	Total thickness variation
UV	Ultra-violet
VCSEL	Vertical cavity surface emitting laser

1 Introduction

1.1 Scope and objective

The present work represents the outcome of the research performed on the subject of MEMS atomic vapor cells for chip-scale atomic clocks and other atomic devices at CSEM SA (Centre Suisse d'Électronique et de Microtechnique), a private, non-profit Swiss research and technology organization. It was realized under the supervision of the University of Neuchâtel between August 2014 and December 2017 under the financing of CSEM internal funding, financed by the canton of Neuchâtel and the Swiss confederation and by the European Space Agency (ESA) under the Networking/Partnering Initiative (NPI). In the frame of this program, a 3 month internship at ESA ESTEC (European Space Research and Technology Center) in Noordwijk, the Netherlands was performed.

MEMS (microelectromechanical systems) atomic vapor cells consist in sealed cavities having an optical access. They are filled with an alkali metal vapor and possibly with other gases. Current applications are found in chip-scale atomic clocks (CSACs) [1], atomic magnetometers [2] and atomic gyroscopes [3]. Here, various aspects related to cells fabrication are reviewed and new microfabrication techniques are studied. Moreover, the performances of atomic cells manufactured with these techniques are measured for their use in CSACs and atomic gyroscopes. The different types of MEMS cells characterized in the frame of the present work are summarized in Tab. 1.1

In the first chapter of this document, a general overview of the working principle of an atomic clock is given. A particular attention is given to the two main interrogation techniques for atomic vapor cell clocks. The different scientific publications on the subject of microfabricated atomic vapor cells for chip scale atomic clock and other atomic devices are then reviewed. The early developments realized in the USA from 2002 to 2008 with the first anodically bonded atomic vapor cell are described. The focus is then given on one of the main research directions taken in Europe which is the use of internal alkali metal dispenser for the cell filling. The researches undertaken on low-temperature bonding and in particular indium bonding for cells with anti-relaxation coatings is then reviewed. The cell functionalization technique proposed by CSEM is then discussed as well as the research made on long light-path cells. Finally, an overview of the publications that were not treated so-far is realized.

The second chapter of this document presents the theoretical aspects in relation with the MEMS atomic vapor cells for CPT atomic clocks and atomic gyroscopes. A general description of the coherent population trapping (CPT) phenomena is given. The structure of the Rb atom is then presented. Details on the optical absorption of rubidium are then given as well as the different relevant aspects for the spectroscopy of the CPT resonance. The link is made with the atomic clock frequency stability and the influence of the different parameters. Based on the requirements for a full chip-scale atomic clock given by ESA, the requirements for a MEMS atomic vapor cell are extracted. The impact of these requirements on particularly relevant technological aspects are deduced. Finally, the theoretical aspects in relation with nuclear magnetic resonance gyroscopes and in particular the

Bonding technology	Isotope	Filling method	Buffer gas	Coating	Other	Chap. / Sec.
Anodic	^{87}Rb	RbN$_3$	Ar-N$_2$	-	-	5.1, 4.1.7
Anodic	^{87}Rb	RbN$_3$	Ar-N$_2$	Al$_2$O$_3$	-	5, 6.2.1
Anodic	natural Rb	RbN$_3$	Ar-N$_2$	Al$_2$O$_3$	-	4.1.6, 4.2
Anodic	natural Rb	dispensing micro-pill	Ar-Ne	Al$_2$O$_3$	-	4.1.3, 4.1.4
Anodic	natural Rb	dispensing micro-pill	Ar-Ne	Al$_2$O$_3$	Au micro-dics	6.2.2
Cu-Cu thermo-compression	natural Rb	dispensing micro-pill	Ar-Ne	Al$_2$O$_3$	-	4.1.5
Cu-Cu thermo-compression	natural Rb	dispensing micro-pill	-	Al$_2$O$_3$	-	4.3
Anodic	natural Rb	RbN$_3$	N$_2$-Xe	Al$_2$O$_3$	4 mm diameter cavity	4.4

Table 1.1: Summary of the different types of MEMS atomic vapor cells characterized in the frame of the present work. "RbN$_3$" stands for RbN$_3$ UV-decomposition. If not otherwise mentioned, the measurement cavity is 2 mm diameter. A simple cavity design is used with RbN$_3$ UV-decomposition and a two cavity design is used with dispensing micro-pills.

measurement of xenon nuclear spin decoherence time is reviewed.

The third chapter of this document focuses on the microfabrication of atomic vapor cells. A detailed literature review on microfabrication techniques applied to MEMS atomic vapor cells is given. In particular the materials, bonding technologies, alkali dispensing methods, getters and anti-permeation techniques are review. Based on the conclusion of the requirements and of the literature review, different cells design are proposed and their microfabrication is described. In particular, Cu-Cu thermocompression as sealing method, alkali azide and Rb micro-dispensing pills as filling method, Al$_2$O$_3$ as anti-permeation barrier and CSEM patent pending gold micro-discs as alkali preferential condensing spots are explored.

The fourth chapter describes the different spectroscopic characterization realized on MEMS atomic vapor cells which fabrication is described in the third chapter. The methods used to characterize the gas content of MEMS cells is presented: first CPT hyperfine frequency spectroscopy is used. Ar-Ne cells are measured in order to determine the buffer gas pressure as well as its dependance to temperature and to find the thermal inversion point. The CPT contrast and linewidth are moreover measured for different temperature and light intensity and the optimal working conditions are determined for Ar-Ne and Ar-N$_2$ cells. A preliminary measurement of a CPT signal in Cu-Cu thermocompression bonding cell is presented as well. Secondly, micro-Raman spectroscopy is presented. This technique is used as a fast technique to measure the N$_2$ partial pressure inside Ar-N$_2$ RbN$_3$ filled cells. The results are compared with CPT hyperfine frequency spectroscopy results made on same cells. Saturated absorption spectroscopy measurements used to assess the vacuum level in evacuated Cu-Cu thermocompression bonded cells are then presented. Finally, preliminary measurements of Xe nuclear spin decoherence time in cells dedicated to gyroscope application are outlined as well as the setup used for it.

The fifth chapter describes the lifetime estimation made on Al$_2$O$_3$ coated MEMS atomic vapor cells filled with RbN$_3$ UV decomposition and sealed by anodic bonding. The main failure mode being identified as disappearing of metallic alkali metal inside the cell, first a consumption model used to estimate the evolution of the alkali metal amount inside the cell is presented. The image analysis

method used to measure this amount over time is then presented and a total lifetime is estimated.

The sixth and last chapter describes the long-term frequency stability measurement realized of MEMS atomic vapor cells in clock operation. A first measurement realized on a classical MEMS cell evidences that the main source of long-term instabilities is due to migration of alkali droplets on the cell window. Therefore, a second measurement shows that the Au micro-disc solution proposed in the third chapter allows to circumvent this limitation and enhance the long-term frequency stability of CPT clocks realized with microfabricated atomic vapor cells.

1.2 Basic operating principle of an atomic clock

The basic operating principle of a vapor cell atomic clock is shown on Fig. 1.1. It consists of a local oscillator (quartz) and a group of atoms (Rb or Cs). The output frequency of a quartz is servo controlled and locked to the frequency of an atomic transition between two atomic levels of the atoms. The frequency stability of the atoms is therefore transferred to the quartz giving the atomic clock its excellent frequency stability over time.
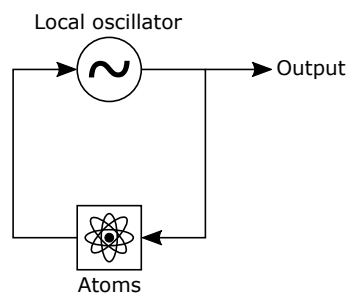
Figure 1.1: Basic operating principle of a passive atomic clock

The selected atomic transition is typically the transition between the hyperfine ground-states levels of the atoms. The quartz frequency (in the MHz range) must therefore be converted to the GHz range in order to interrogate the hyperfine frequency of the atoms. Moreover, in cell clocks, a third level is required in order to interrogate the atoms. This third level is typically an excited state of the atom separated from the ground states by an optical transition. Two interrogation schemes are commonly used for interrogation: Double Resonance (DR) or Coherent Population Trapping(CPT).
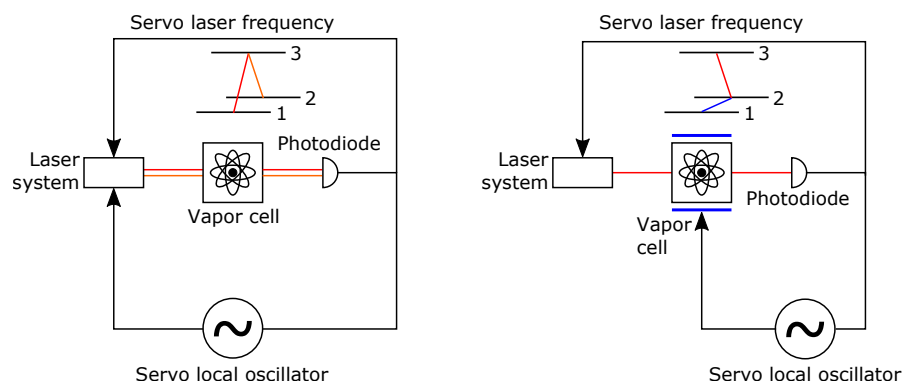
Figure 1.2: Coherent Population Trapping interrogation scheme (left) and Double Resonance interrogation scheme (right) - The fluorescence can also be detected in the case of CPT.

In the DR interrogation scheme, two fields are applied to the atoms: a microwave field and

an optical field (see Fig. 1.2 right). The microwave field, created by multiplication of the quartz frequency, is resonant with the atom hyperfine frequency. The optical field is used to interrogate the absorption between one of the ground states and the excited state and is locked to this transition. Due to absorption, the light field depopulates the observed ground state level which increases the transmission. When the microwave frequency is resonant with the hyperfine frequency, the observed ground state level is repopulated and the transmission decreases. This phenomenon creates an absorption peak on which the quartz frequency can be servo controlled. A detailed description of the phenomena can be found in [4].

In the CPT interrogation scheme, a bichromatic optical field with a frequency difference in the GHz range is applied to the atoms (see Fig. 1.2 - left). The microwave frequency is obtained by the multiplication of the quartz frequency and the generated optical fields are servo controlled to be resonant with the optical transition between the ground states and the excited state. When the frequency detuning between the two components of the bichromatic light field is resonant with the hyperfine frequency, a coherent effect traps the atoms in a so-called dark state. As a consequence, the absorption reduces. As in the DR scheme, the quartz frequency can the be servo controlled to this peak. A detailed description of this effect can be found in Chap. 2.

These two continuous-wave (CW) interrogation techniques imply a high level of coupling between the microwave frequency and the optical field which implies a transfer of laser instabilities to the clock transition. Pulsed schemes were therefore proposed inspired by the Cs beam tube working principle [5]. Pulsed schemes however require a more complex setup with an acousto-optical modulator (AOM) or any other light shutters for the clock operation. They are therefore not excellent candidate for chip-scale atomic clock with a high level of integration and will not be described here.

1.3 Chip-scale atomic clock and MEMS atomic vapor cells: State of the art

1.3.1 Early development

The early development of a chip-scale atomic clock were realized in 2002 [6]. The requirements for the overall device were a volume of 1 cm^3, a short term frequency stability of $1 \cdot 10^{-11}$ at 1h integration time and a total power consumption of 30 mW. As the total clock dimensions are relatively small, these requirements are transferred to the atomic cell for which a maximal volume of 5 mm^3 is allowed. Such small cells cannot be realized with the conventional glass blowing technology. The MEMS technology is therefore the best way to produce such small size cells. Anodically bonded cells with a stacking of glass, DRIE etched silicon and glass were then realized. As the filling technique of the cells was still not developed, these cells were linked to an external glass blown tube and filled using cesium with conventional distillation techniques.

The first fully microfabricated atomic vapor cell was realized by NIST in 2004 [7]. As for the first prototypes, the cell was composed of an etched silicon wafer, anodically bonded to two Pyrex wafers. Two etching techniques were compared (DRIE and KOH) as well as two cesium filling techniques: Barium azide decomposition technique (see Sec. 3.1.3.2) and direct dispensing (see Sec. 3.1.3.3). End of 2004, cells of the second type were used to build the first microfabricated atomic clock ever demonstrated [1], and later the same year the first microfabricated magnetometer based on MEMS atomic vapor cells was demonstrated [2].

As the Barium azide decomposition technique showed some long term stability issues, in 2005 a new filling technique was tested by NIST with rubidium which basically moved the barium azide decomposition to the outside of the cell [8]. This improved the cell purity and therefore its long term performances. A relative drift value of $5 \cdot 10^{-11}$/day could then be reached. In 2007 finally, a new alkali metal filling technique using the UV decomposition of CsN$_3$ [9] was demonstrated (see Sec.

3.1.3.2).

On a commercial point of view, the SA.45s CSAC was released in 2011 by the commercial company Symmetricom[1] with a total volume of 16 cm^3, a full clock short term frequency stability of $2.5 \cdot 10^{-10} \tau^{-1/2}$ and a frequency drift of $9 \cdot 10^{-10}$/month with a total power consumption of 115 mW [6, 10, 11, 12, 13, 14]. Recently, another commercial product was proposed by AccuBeat, Israel [15]. However this product relies on small glass-blown cells.

Shortly after the first researches undertaken by NIST, Teledyne technology Inc. (USA), another company, started the development of atomic vapor cells for atomic clocks. In 2004, a micro-machined chip-scale atomic clock project sponsored by DARPA was reported [16]. The atomic cells were realized with the standard anodic bonding of glass-silicon-glass technique. The design of the Cesium-filled cell was realized such that the alkali-metal containing cavity was surrounded by vacuum-filled cavities for a better thermal management and a better pressure homogeneity. As for the first prototype of NIST, the cells were filled with the help of an external glass tube. In 2008, a new design of the chip-scale atomic clock was reported [17]. The external glass tube approach was forsaken and the Rb filling was realized by a "tube free filling method". No new publication were reported after that on this project to my knowledge.

1.3.2 Internal alkali dispenser

Research on chip scale atomic clocks were undertaken in Europe through various projects since 2006: MACQS (2009-2014 financed by SNF), CIMENT (2006-2008 financed by CUS), mUSO (2007-2009 financed by ESA), MAC-TFC (2008-2011 financed by EU through the 7th framework program). On the cell point of view, two main research directions were taken in these projects: The first, driven by the MAC-TFC project, explored the use of micro alkali dispenser inside anodically bonded cells. The second, driven in the other projects, explored, among others, Indium as bonding techniques for cell microfabrication with an external alkali dispensing technique.

The first reporting of the realization of a miniature atomic vapor cell in Europe was made in 2007 by Douhai et al. [18, 19, 20]. The cesium cells were realized with the standard Pyrex-silicon anodic bonding technology. The cells were designed with two cavities, one for the filling and one for the laser probing. An internal alkali dispenser used for the cesium filling is placed in the filling cavity (see Sec. 3.1.3.1). A buffer gas mixture of N$_2$-Ar was added. A characterization of these cells was reported in 2010 and showed a short term frequency stability of $5 \cdot 10^{10} \tau^{-1/2}$ [21]. The Wroclaw University of technology developed in parallel cells using the same approach [22] and glass transmissive cells [23]. Recently, the relatively large dispensing pill was replaced by a Cs dispensing paste in novel cells [24, 25]. Finally, atomic vapor cells filled with ^{87}Rb dicromate were reported by Ermak et al. [26]. They were characterized in a clock setup and showed a potential short term frequency stability in the order of $5 \cdot 10^{-11} \tau^{-1/2}$ [27, 28].

In 2011, due to incompatibilities of N$_2$ with the dispensing micro-pills, the buffer gas mixture was replaced with a single Ne back-filling which possesses an inversion temperature of approximately 80°C for cesium [29]. The same year, modifications in the cell design and an optimization of the anodic bonding parameters was realized. New cells were produced in which the filling cavity was linked to the probing cavity with micro-channels [30]. Characterization of these cells with optimized buffer gas pressure was realized and showed a short term frequency stability of $3.8 \cdot 10^{11} \tau^{-1/2}$ and a long term stability below 10^{-11} until 5000 s [31].

A new design was proposed in 2013 [32] in which getter was added inside the cell to the previous version. This reduced the impurity pressure to less than $4 \cdot 10^{-2}$ mbar as compared to the 2 mbar measured previously. However no long term study was undertaken.

Finally, the intrinsic frequency of a getter free cell filled with a Cs dispenser was measured in long term and a maximal relative drift of $-7.8 \pm 0.6 \cdot 10^{-11}$/day was measured [33]. A value in the

---

[1]Now Microsemi corp., USA

order of $-4.4 \cdot 10^{-12}$/day was measured in a preliminary study on a cell filled with dispensing paste [24]. In the first case, the drift was attributed to the Ne permeation through the cell windows. As a solution, aluminosilicate glass (ASG) was proposed as a potential solution by Dellis et al. [34] but no long-term frequency stability measurements were reported to my knowledge.

1.3.3 Low-temperature bonding for cells with anti-relaxation coating

In 2010, a new indium bonding technique for MEMS vapor cells was proposed by Pétremand et al. [35]. The advantage of this method compared to anodic bonding is the low bonding temperature making it compatible with wall coating instead of buffer gas. Cells were realized by indium bonding of glass to silicon. Absorption spectrum and CPT were recorded but no information was given on the cell lifetime. This method was adapted in 2011 by Veccio and al. for the bonding of LTCC based cells [36, 37]. The cell lifetime was limited to 20 days in this case. In 2012, an improved design of indium bonded cells was proposed by Strässle et al. [38, 39]. These cells were tested for hermeticity and an upper leak rate limit of $1.5 \cdot 10^{-13}$ mbar l/s was found. A reaction of Rb with In was nevertheless observed inside the cell which discarded indium as a bonding method [39]. However tests on octadecyltrichlorosilane wall coating as substitute to the buffer gas were realized and its anti-relaxation properties were demonstrated [40].

1.3.4 Functionalized cells

Research on MEMS atomic vapor cells is realized at CSEM since 2009. Atomic vapor cells realized at CSEM were the first proposed at a wafer scale to my knowledge. They are based on anodic bonding of borosilicate glass to a silicon core and are filled with Ar/N_2 mixture. Two filling techniques were tested [41]: Direct alkali dispensing and alkali salt decomposition. The second technique was retained for the next developments. The Ar is filled inside the cell prior to the bonding whereas the N_2 comes from the UV decomposition of RbN_3.

In addition to the cell fabrication, CSEM explored the functionalization of the atomic vapor cell window [42, 43, 44, 45]. Resistive heaters, magnetic coils and a temperature sensor are integrated directly onto both cell windows using two metallic structured layers separated by a thin insulating dielectric layer.

1.3.5 Long light-path microfabricated cells

Increasing the lightpath of the laser inside a MEMS cell is a good mean to improve the short term frequency stability. This was first realized in 2009, with a new design for which distributed Bragg reflectors (DBR) were placed on the inside walls of the cells. This allows a second light-path through the cells with the output of the laser at the same side as the input [46, 47].

In 2014, anodically bonded cells with a thick glass core were proposed by Pétremand et al. [48]. Cells were realized with a stacking of glass, silicon, thick glass core, silicon and glass in order to overcome the cell length limitation due to the maximal etching thickness of silicon. With this technique, cells with a thickness of 4 mm were realized.

Recently, Chutani et al. proposed a new design using microfabricated gratings and mirrors in order to route the light in a path perpendicular to the cell window [49].

Finally, perforated hollow core fibers filled with alkali were moreover reported as containers for atomic absorption spectroscopy [50, 51].

1.3.6 Atomic vapor cells for magnetometers

In addition to atomic clocks, atomic vapor cells can be used for the fabrication of atomic magnetometers. Such magnetometers have application in biomedical imaging [52]. Atomic vapor cells array

were reported by Woetzel et al. [53, 54]. These atomic vapor cells are made by a classical anodically bonded stacking of borosilicate, silicon and borosilicate. They are filled by CsN_3 decomposition. Due to the filling method, the amount of Cs is limited by the amount of buffer gas required (see Sec. 3.1.3.1). This also limits the lifetime of the cells to a few hours, as the operating temperature is much higher than for atomic clocks. Different anti-permeation wall coatings were tested in order to improve the lifetime. Al_2O_3 showed promising results [55].

In 2007, a new type of vapor cell fabrication based on chip-scale micro-glass blowing was proposed [56]. Such cells were later characterized by Ji et al. in combination with an anti-relaxation coating for magnetometers applications [57, 58, 59].

Atomic vapor cells for magnetometers using Potassium were reported in several publication of Tsujimoto et al. The cells are filled using alkali metal source tablet [60, 61, 62]: The alkali metal is released by a chemical reaction, either KN_3 decomposition or reaction of KCl with BaN_6. The tablet is used in order to increase the generation yield and to prevent splashing. This technology was further improved by other microfabrication means and different tablet fabrication designs were proposed [63, 64]. In the frame of the same projects, cells sealed using glass-frit over micro-channels were investigated [65, 61]. The micro-channels are used to evacuate the unwanted gas created during the decomposition process and to back-fill a precise buffer gas mixture. However, no experimental demonstration of this technique was reported yet.

1.3.7   Other related publications

MEMS atomic vapor cell fabrication was also studied by other groups in the world which were not cited here above: At University of Princeton, fabrication of MEMS atomic vapor cells was reported [66]. The cells were fabricated using anodic bonding and direct alkali dispensing. An interesting alternative filling method was proposed by Gong et al. in 2006 [67]. The alkali metal was dispensed inside the cell by electrolysis of alkali enriched glass. At Cornell University another method using alkali wax packets was reported by Radhakrishnan et al. [68]. Finally, small all-glass Rb cells sealed with a CO_2 lasers was reported by Losev et al. [69]. These cells are made of a cylindrical glass tube with length and diameter of 5 mm and sealed with a window having a thickness of 0.5 mm.

In China, the first microfabrication of atomic vapor cells was reported in Beijing in 2010 [70]. These cells were realized by anodic bonding of glass-silicon-glass and filled with barium azide. An alternative filling technique was reported by Wei et al. [71]. This filling technique used the reaction of Ca and RbCl inside the cell which takes place above the softening point of Pyrex, therefore leading to a deformation of the cell wall. Another filling technique was proposed by Chen et al. which used the barium azide decomposition technique together with TiH_2 decomposition in order to fill the cell with Rb and H_2 buffer gas [72, 73]. This decomposition takes also place at high temperature which has the same deformation effect as the previous technique. Finally, cells realized using alkali azide decomposition in a double cavity design was reported by Ji et al. [74]. Recently, a first prototype of a complete chip-scale atomic clock was demonstrated in Shanghai [75].

1.4   Summary

The drift performances reported in literature for chip-scale atomic clocks are summaries in table 1.2. Based on these results, the following conclusions can be drawn:

- The commercial product SA-45s clock of Symmetricom provides a relative drift value of $3 \cdot 10^{-11}$/day and uses anodically bonded MEMS atomic vapor cells. However details on the manufacturing process are not given by the manufacturer.

- Good results in term of intrinsic frequency drift were obtained by the use of internal alkali

dispensers. The limitations are attributed to gas permeation in the cell windows.

- Wafer-scale fabrication of MEMS atomic vapor cells filled with RbN_3 offers potential cost reduction as compared to other methods. However, the limited lifetime of cells filled with this method requires complementary technological steps.

- Different technologies were developed in order to increase the laser lightpath inside the cell and improve the short-therm frequency stability.

- Indium cannot be used for atomic vapor cells as it reacts with the alkali metal.

Reference	Frequency drift reported	Technology used
[8]	$-2 \cdot 10^{-8}$/day	Anodic bonding and BaN_6 + CsCl internal decomposition
[8]	$5 \cdot 10^{-11}$/day	Anodic bonding and BaN_6 + RbCl external dispensing
SA.45s CSAC	$\leq 3 \cdot 10^{-11}$/day	entire clock performance
[33]	$-7.8 \pm 0.6 \cdot 10^{-11}$/day	anodic bonding, internal alkali dispenser, 0-LS extrapolated
[24]	$-4.4 \cdot 10^{-12}$/day	anodic bonding, internal alkali dispensing paste, 0-LS extrapolated

Table 1.2: Comparison of the long-term frequency stability achieved by the different research groups in the world

2 Physics of Rb atomic vapor cells

2.1 Coherent Population Trapping: Description of the phenomenon

Coherent population trapping is a phenomena commonly used for atomic vapor cell clock operation (see Chap. 1.2). It is best described in a semi-classical treatment of the atom-photon interaction [76]. In a first approach, a three level system is considered where an excited level $|3\rangle$ is coupled to two lower levels $|1\rangle$ and $|2\rangle$. The decay rates are neglected in this simple model (see Fig. 2.1).
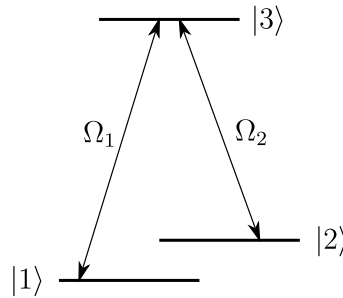
Figure 2.1: Three level system (Λ-scheme) considered for the explanation of the coherent population trapping phenomena

Two optical frequencies of a bichromatic laser excite the $|1\rangle \to |3\rangle$ and $|2\rangle \to |3\rangle$ transitions whose Rabi frequencies are:

$$\Omega_{1,2} = \frac{\boldsymbol{\varepsilon}_{1,2}\mathbf{d}_{1,2}}{\hbar} \tag{2.1}$$

with $\mathbf{d}_{1,2}$ the dipole matrix element of the considered transition and $\boldsymbol{\varepsilon}_{1,2}$ the electric field. The total electric field writes as $\boldsymbol{\varepsilon}(t) = \varepsilon_1 e^{-i(\omega_1 t + \phi_1)} + \varepsilon_2 e^{-i(\omega_2 t + \phi_2)}$ in the rotating wave approximation and the Hamiltonian writes as:

$$\mathbf{H} = \mathbf{H}_0 + \mathbf{H}_{\text{int}} \tag{2.2}$$

with $\mathbf{H}_0$ the unperturbed Hamiltonian and $\mathbf{H}_{\text{int}}$ the interaction hamiltonian defined as:

$$\mathbf{H}_0 = E_1 |1\rangle \langle 1| + E_2 |2\rangle \langle 2| + E_3 |3\rangle \langle 3| \tag{2.3}$$

and

$$\mathbf{H}_{\text{int}} = -\frac{\hbar\Omega_1}{2} e^{-i(\omega_1 t + \phi_1)} \ket{3}\bra{1} + \frac{\hbar\Omega_2}{2} e^{-i(\omega_2 t + \phi_2)} \ket{3}\bra{2} + \text{c.c.} \tag{2.4}$$

Let us now define an orthogonal basis $\{\ket{NC}, \ket{C}, \ket{3}\}$ with $\ket{C}$ a coupled state and $\ket{NC}$ an non-coupled state as:

$$\ket{C} = \frac{1}{\sqrt{\Omega_1^2 + \Omega_2^2}} \left(\Omega_1 e^{-iE_1 t/\hbar} \ket{1} + \Omega_2 e^{-iE_2 t/\hbar + i(\phi_2 - \phi_1)} \ket{2} \right). \tag{2.5}$$

and

$$\ket{NC} = \frac{1}{\sqrt{\Omega_1^2 + \Omega_2^2}} \left(\Omega_1 e^{-iE_1 t/\hbar} \ket{1} - \Omega_2 e^{-iE_2 t/\hbar + i(\phi_2 - \phi_1)} \ket{2} \right). \tag{2.6}$$

The transition probability of the $\ket{NC}$ state to the $\ket{3}$ state is given by:

$$\bra{3}H_{\text{int}}\ket{NC} = \frac{\hbar\Omega_1\Omega_2}{2\sqrt{\Omega_1^2 + \Omega_2^2}} e^{-i(E_1/\hbar + \omega_1)t - i\phi_1} \left(1 - e^{i\delta_R t - i\delta_\phi} \right) \tag{2.7}$$

with $\delta_R = (\omega_1 - \omega_2) - (E_2 - E_1)/\hbar$ the 2 photons Raman frequency detuning and $\delta_\phi = \phi_2 - \phi_1$ the optical frequency phase difference. Therefore, when the phase difference is a multiple of 2π and when the Raman frequency detuning is equal to 0, no excitation of the $\ket{NC}$ state to the $\ket{3}$ state is possible. For an atom prepared on the $\ket{NC}$ state, the Schrödinger equation is:

$$\frac{\mathrm{d}}{\mathrm{d}t}\ket{NC} = \frac{1}{i\hbar}(\mathbf{H}_0 + \mathbf{H}_{\text{int}})\ket{NC} = 0 \tag{2.8}$$

This is the so-called CPT effect. When the difference between the two laser frequencies is exactly equal to the hyperfine frequency of the atoms, a part of those are trapped in a so-called dark state. In this particular state, the atoms cannot be brought into an excited state by the light and the transparency becomes maximal.

As said above, this description is only a first approach. It does not take into account the different relaxation of the excited state, essential to populate the dark state. For a more detailed approach, see section 2.4

2.2   Structure of the Rb atom

In the following, an overview of the Rb atomic structure is given. This element is commonly used in cells atomic clocks for the following reasons:

- It can easily be vaporized into a relatively dense vapor

- The two isotopes have a nucleus magnetic field (odd number of protons and neutrons) which produces an hyperfine splitting

- Since it has a single valence electron, the electronic structure is fairly simple

- It has a transition in the GHz domain which is technologically easily accessible and provides a stable frequency reference

The occupied orbitals of rubidium atom are $1s^2 2s^2 2p^6 3s^2 3p^6 3d^{10} 4s^2 4p^6 5s$. As they are in a closed sub-shell, the total angular momentum of the first 36 electrons is zero and the 5s electron acts as

an hydrogen-like electron. Here we will focus on the transitions between the ground state of this electron 5s and its first excited state 5p. The sub-structure of those levels arises from three level of correction to the gross structure predicted by the quantum mechanics of non-relativistic electrons: the fine structure, the hyperfine structure and the Zeeman splitting.

2.2.1 Fine structure

The fine structure arises from three corrective terms to the non-relativistic Coulomb interaction Hamiltonian: the kinetic energy relativistic correction term, the spin-orbit term, and the Darwinian term. Given the unperturbed Hamiltonian:

$$\mathbf{H}_0 = \frac{\mathbf{p}^2}{2m} - \frac{Ze^2}{r} \tag{2.9}$$

we have the unperturbed energy level:

$$E_n = \frac{Z^2}{2n^2} \tag{2.10}$$

and the eigenstates (including the spin):

$$|n, l, m_l, m_s\rangle \tag{2.11}$$

which are $2n^2$ degenerated. The fine structure Hamiltonian writes as:

$$\mathbf{H}_{\text{FS}} = \mathbf{H}_{\text{Relativistic}} + \mathbf{H}_{Darwinian} + \mathbf{H}_{SO} \tag{2.12}$$

with

$$\mathbf{H}_{\text{Relativistic}} = -\frac{\alpha^2}{8} p^4 \tag{2.13}$$

$$\mathbf{H}_{Darwinian} = \frac{\alpha^2}{8} \nabla^2 V \tag{2.14}$$

$$\mathbf{H}_{SO} = \frac{\alpha^2}{2} \frac{1}{r} \frac{dV}{dr} \mathbf{L} \cdot \mathbf{S} \tag{2.15}$$

$$\tag{2.16}$$

where $\mathbf{L}$ is the orbital angular momentum and $\mathbf{S}$ the spin angular momentum. The relativistic and Darwinian terms are negligible as compared to the spin-orbin interaction. We define the total angular momentum of the electron as:

$$\mathbf{J} = \mathbf{L} + \mathbf{S} \tag{2.17}$$

The corresponding quantum number J must lie in the range $|L - S| \leq J \leq L + S$. For the ground state of Rb, $L = 0$ and $S = 1/2$ so $J = 1/2$ and for the first excited state $L = 1$ and $S = 1/2$ so $J = 1/2$ or $J = 3/2$. The total energy shift due to this correction is then given by:

$$\Delta E_{\text{FS}} = (Z\alpha)^2 (-E_n) \frac{1}{n^2} \left(\frac{3}{4} - \frac{n}{J + 1/2} \right) \tag{2.18}$$

The shift therefore only depends on J. In the case of the two Rb levels of interest (5s and 5p), this leads to a splitting of the level 5p in two sub-level with $J = 1/2$ and $J = 3/2$. In the standard spectroscopic notation, atomic levels are written as $n^{2S+1}L_J$ with L written as s,p,d etc. The levels of interest for Rb are therefore $5^2\text{s}_{1/2}$, $5^2\text{p}_{1/2}$ and $5^2\text{p}_{3/2}$ (see Figure 2.2). The D line transitions, *i.e.*

transitions between the $L = 0$ (5s) and $L = 1$ (5p) state split then into two components defined as D1 for the transitions $5^2s_{1/2} \rightarrow 5^2p_{1/2}$ and D2 for the transitions $5^2s_{1/2} \rightarrow 5^2p_{3/2}$.

2.2.2 Hyperfine structure

The next shift of the energy levels arises from the interaction of the total magnetic moment of the electron with the magnetic moment of the atomic nucleus. A detailed treatment can be found in [77, 78]. Here, only an overview will be given where the effect of higher order interactions are not taken into account. Those are effects such as the electric quadrupole interaction or the magnetic octupole interaction which require a rigorous treatment.

The dominant magnetic dipole interaction between the nuclear dipole momentum $\boldsymbol{\mu}_I$ and the magnetic field produced by the electron B_e is:

$$H_{\text{HFS}} = -\boldsymbol{\mu}_I \cdot \mathbf{B}_e \tag{2.19}$$

The nuclear dipole momentum is related to the nuclear spin by $\boldsymbol{\mu}_I = g_I \mu_N \mathbf{I}/\hbar$ where $\mathbf{I}$ is the nuclear angular momentum, g_I is the nuclear g-factor and μ_N is the nuclear magneton. For a particular electronic energy level, we can assume that $\mathbf{B}_e$ is proportional to $\hbar \mathbf{J}$ and the interaction Hamiltonian becomes:

$$\mathbf{H}_{\text{HFS}} = \frac{A}{\hbar^2} \mathbf{I} \cdot \mathbf{J} \tag{2.20}$$

Where A is the hyperfine structure constant. Now, given the total atomic angular momentum:

$$\mathbf{F} = \mathbf{J} + \mathbf{I} \tag{2.21}$$

with the eigenstates $|F, m_F\rangle$, the scalar product $\mathbf{I} \cdot \mathbf{S}$ writes as:

$$\mathbf{I} \cdot \mathbf{S} = \frac{1}{2} \left(\mathbf{F}^2 - \mathbf{S}^2 - \mathbf{I}^2 \right) \tag{2.22}$$

and the total energy shift due to the hyperfine correction is then given by:

$$\Delta E_{\text{HFS}} = \frac{1}{2} A [F(F+1) - I(I+1) - J(J+1)] \tag{2.23}$$

F must lie in the range $|J - I| \leq F \leq J + I$ and each level is $2F + 1$ degenerate in the absence of an external magnetic field (see below). The value of the nuclear angular momentum is different for ^{87}Rb and ^{85}Rb: $I = 3/2$ and $I = 5/2$ respectively. For both however, $J = 1/2$ for the $5^2s_{1/2}$ ground state, $J = 1/2$ for the $5^2p_{1/2}$ D1 excited state and $J = 3/2$ for the $5^2s_{3/2}$ D2 excited state. For example, for ^{87}Rb, $F = 1$ or $F = 2$ for the ground state as well as for the excited state.

2.2.3 Zeeman splitting

When an external magnetic field is applied, the degeneracy of the hyperfine is removed. The interaction Hamiltonian describing the interaction with an external magnetic field writes as:

$$\mathbf{H}_B = \frac{\mu_B}{\hbar} (g_S \mathbf{S} + g_L \mathbf{L} + g_I \mathbf{I}) \cdot \mathbf{B} \tag{2.24}$$

where g_S, g_L and g_I are respectively the electron spin, the electron orbital, and the nuclear g-factors. For a magnetic field oriented in the z direction, the Hamiltonian writes as:

$$\mathbf{H}_B = \frac{\mu_B}{\hbar} (g_S S_z + g_L L_z + g_I I_z) B_z \tag{2.25}$$

If the energy shift is sufficiently small, as compared to the fine splitting, **J** can be used as a quantum number and the interaction Hamiltonian writes as:

$$\mathbf{H}_{\text{B}} = \frac{\mu_B}{\hbar}(g_J J_z + g_I I_z)B_z \tag{2.26}$$

with g_J the Landé g-factor calculated for each fine structure level:

$$g_J = g_L \frac{J(J+1) + L(L+1) - S(S+1)}{2J(J+1)} + g_S \frac{J(J+1) - L(L+1) + S(S+1)}{2J(J+1)} \tag{2.27}$$

Again, if the energy shift is sufficiently small, as compared to the hyperfine splitting, **F** can be used as a quantum number. and the interaction Hamiltonian writes as:

$$\mathbf{H}_B = \frac{\mu_B}{\hbar}(g_F F_z)B_z \tag{2.28}$$

with g_F the hyperfine Landé factor:

$$g_F = g_J \frac{F(F+1) + J(J+1) - I(I+1)}{2F(F+1)} + g_I \frac{F(F+1) - J(J+1) + I(I+1)}{2F(F+1)} \tag{2.29}$$

This results in a lift of the degeneracy of the hyperfine levels and a shift proportional to magnetic quantum number m_F and the shift is given by:

$$\Delta E_{|F,m_F\rangle} = \mu_B g_F m_F B_z \tag{2.30}$$

However, due to the treatment in perturbation of the hyperfine levels, this result is only valid for small values of the B and the second order effects are not taken into account. For a more detailed treatment, the quantum mixing of the states between the Zeeman and the hyperfine splitting has to be studied. The interaction Hamiltonian is then taken as:

$$\mathbf{H} = \mathbf{H}_{\text{HFS}} + \mathbf{H}_{\text{B}} \tag{2.31}$$

and the eigenenergies of the states $|F, m_F\rangle$ for the ground states of the D lines are given by the Breit-Rabi formula [79]:

$$\Delta E_{|F=I\pm 1/2, m_F\rangle} = -\frac{\Delta E_{\text{HFS}}}{2(2I+1)} + \mu_B g_I m_F B \pm \frac{\Delta E_{\text{HFS}}}{2}\sqrt{1 + \frac{4m_F x}{2I+1} + x^2} \tag{2.32}$$

where the $\pm$ sign is taken to be the same as is $m_F = m_I \pm m_J = m_I \pm 1/2$ and with x the field strength parameter given by:

$$x = \frac{\mu_B B(g_J - g_I)}{\Delta E_{\text{HFS}}} \tag{2.33}$$

From this equation, the small-field shift of the two $m_F = 0$ ground states levels can be calculated. Indeed, these two levels have no first order shift:

$$\Delta E_{\text{clock}} = \frac{(g_J - g_I)^2 \mu_B^2}{2\hbar \Delta E_{\text{HFS}}} B^2 \tag{2.34}$$

Based on the above calculations, the different physical quantities can be calculated for ^{87}Rb and ^{85}Rb: The fine structure splitting of the D line given by Eq. 2.18 and the hyperfine splitting given by Equation 2.23. The structure of these two isotopes is presented in Fig. 2.2. The first order Zeeman

shift given in Eq. 2.30 and the second order Zeeman splitting of the clock transition given in Eq. 2.34 can also be calculated and are presented in Tab. 2.1 [78, 80]:
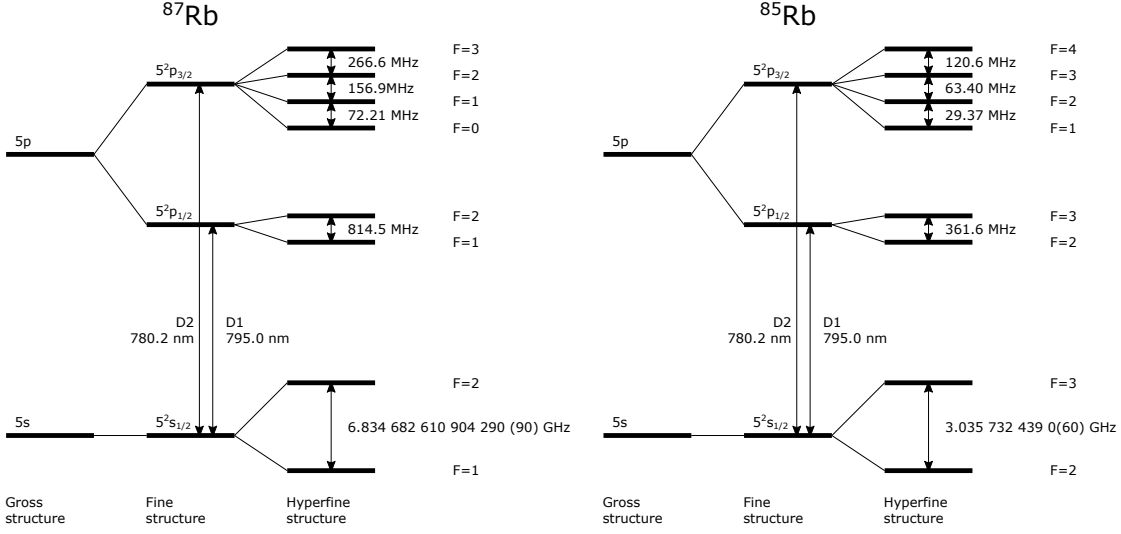
Figure 2.2: Gross, fine and hyperfine structure of Rb D lines in absence of external magnetic field

		^{87}**Rb**	^{85}**Rb**
Relative natural abundance	NA	72.17 %	27.83 %
First order Zeeman shift	$\Delta\nu_{m_{F_1} \to m_{F_2}}$	$(m_{F_1} + m_{F_2})\cdot$ 0.7 MHz/G	$(m_{F_1} + m_{F_2})\cdot$ 0.47 MHz/G
Second order Zeeman shift of the clock transition	$\Delta\nu_{\text{clock}}$	575.15 Hz/G^2	1293.98 Hz/G^2

Table 2.1: Relative abundance and first and second order Zeeman shifts for ^{85}Rb and ^{87}Rb

2.3 Optical absorption of rubidium

2.3.1 Relative transition strength

The relative absorption intensity of each transition is governed by the transition strength factor and therefore the dipole matrix element $\langle F, m_F | er | F', m_F' \rangle$ [81, 78, 80]. The value of these coefficients as well as the authorized transitions depend on the light polarization. For example, a σ^+ polarized light, only drives $|F, m_F\rangle \to |F', m_F' = m_F + 1\rangle$ transitions due to conservation of the angular momentum. The dipole matrix element of a transition can be expressed in function of a reduced matrix element $\langle J || er || J' \rangle$ as:

$$\langle F, m_F | er | F', m_F' \rangle = c_{F,m_F} \langle J || er || J' \rangle \tag{2.35}$$

Moreover, in a single light frequency absorption experiment, each of the m_F transition can be considered as degenerated in F. In this case, the total transition strength of the hyperfine transition is given by $C_F^2 = \sum c_{F,m_F}^2$, the sum over each Zeeman sub-levels. The values of C_F^2 do not depend on the polarization and are given for the ^{87}Rb in Tab. 2.2.

		F'	
		1	2
F	1	1/6	5/6
	2	5/6	5/6

Table 2.2: Strength factor for the transitions for the ^{87}Rb D1 line - C_F^2

2.3.2 Absorption lineshape

2.3.2.1 Absorption profile

Each of the $|F\rangle \to |F'\rangle$ optical transition can be considered as a Voigt profile. Voigt profiles are resulting from the convolution of a Gaussian (resulting from the Doppler broadening of the transition) and a Lorentzian profile (resulting from the relaxations).

Voigt profiles are defined by:

$$V(x, x_0, \sigma, \gamma) = \int_{-\inf}^{\inf} G(x', \sigma) \cdot L(x - x_0, \gamma) dx' \tag{2.36}$$

With $G(x, \sigma) = \frac{e^{-x^2/2\sigma^2}}{\sigma\sqrt{2\pi}}$ a Gaussian profile and $L(x, \gamma) = \frac{\gamma}{\pi(x^2 + \gamma^2)}$ a Lorentzian profile.

The Gaussian and Lorentzian width are respectively defined as:

$$\text{FWHM}_G = 2\sqrt{2\ln(2)}\sigma \tag{2.37}$$
$$\text{FWHM}_L = 2\gamma \tag{2.38}$$

2.3.2.2 Broadening effect

The Gaussian broadening arises from the Doppler effect. Its FWHM is given by [82]:

$$\sigma = \frac{\sqrt{\frac{2RT}{M}}}{\lambda} \tag{2.39}$$

with $R = 8.314$ J/mol K the ideal gas constant, T the cell temperature and M the molar mass of the alkali atom.

As an order of magnitude, for a ^{87}Rb cell at a temperature between 80 and 100°C, the Gaussian broadening is in the order of 540 to 560 MHz for optical transitions.

The Lorentzian broadening is the sum of the transition natural width corresponding to the Rb spontaneous emission and of the buffer gas induced linewidth due to collisions between Rb atoms and buffer gas atoms. It is expressed as follow:

$$\text{FWHM}_L = \text{FWHM}_0 + \beta_{\text{Buffer gas}} P \tag{2.40}$$

Where $\text{FWHM}_0 = 6.0666$ MHz is the ^{87}Rb natural linewidth [78], $\beta_{\text{Buffer gas}}$ a coefficient depending on the buffer gas (see Tab. 2.3) and P the buffer gas pressure.

2.3.2.3 Optical pumping and saturation effects

The measured shape of broadened absorption line are moreover modified by optical saturation effects and optical pumping. In first approximation, the absorption of light through an absorptive medium is governed by the Beer-Lambert law. For a small path dz, the light absorption is given $\frac{dI}{dz} = -\alpha I$ with

Gas	Optical broadening [MHz/Torr]	
	D1	D2
He	18.9	20.0
Ne	9.84	9.47
Ar	18.1	17.7
N_2	16.3	18.3

Table 2.3: Optical broadening coefficients of typical gases for the D1 and D2 lines of Rb [83]

z the position and α the absorption coefficient. The total transmitted intensity is therefore given by:

$$I(z) = I_0 \cdot e^{-\alpha z} \tag{2.41}$$

with I_0 the initial intensity. In practice, the absorption is however limited by saturation effects and it is given by:

$$\frac{dI}{dz} = -\frac{\alpha I}{1 + I/I_{\text{Sat}}} \tag{2.42}$$

Where I_{Sat} is the saturation intensity.

As an effect, this saturation distorts the lineshape and the Lorentzian width becomes [84]:

$$\text{FWHM}_S = \text{FWHM}_L \sqrt{1 + S_0} \tag{2.43}$$

With S_0 a saturation parameter proportional to the intensity. Together with optical pumping which redistributes the populations amongst the hyperfine levels, it does not allow a proper fitting of the linewidth for any light intensity. Width measurement must be done well below the saturation intensity or extrapolated to 0-light intensity [81].

It should noted that the saturation intensity depends on the light polarization. As an example, it is given for the D1 line of ^{87}Rb by [78]:

$$I_{\text{Sat},\pi} = 3.05381 \text{mW/cm}^2 \tag{2.44}$$
$$I_{\text{Sat},\sigma^\pm} = 1.66933 \text{mW/cm}^2 \tag{2.45}$$

2.3.3 Absolute absorption

A detailed treatment of the absolute absorption can be found in [81]. In particular the effect of optical pumping is discussed. Here we will only focus on the relevant parameter. From the Beer-Lambert law (Eq. 2.41), the absorption is governed by the absorption coefficient α. This coefficient can be written in term of the microscopic cross-section σ_i of the involved transitions and the number density n:

$$\alpha = \sum_i n\sigma_i \tag{2.46}$$

The relative cross section of each transition is given by the transition strength given in Sec. 2.3.1 and the absorption coefficient can finally be written as:

$$\alpha \propto \sum_{F_g \to F_e} nC_F^2 \tag{2.47}$$

The atomic vapor density is given for rubidium by:

$$n_{\text{Rb}} = \frac{P_{\text{Rb}}}{k_B \cdot T} \tag{2.48}$$

with the vapor pressure for Rb under liquid phase given by [78]:

$$P_{\text{Rb}} = 10^{7.193 - \frac{4040}{T}} \, \text{Torr} \tag{2.49}$$

It can therefore be seen that the central parameter to tune the absorption of vapor cell is its vapor density and therefore its temperature.

2.4 Spectroscopy of the CPT resonance

2.4.1 CPT amplitude and linewidth

The explanation of the spectroscopic properties of the CPT resonance requires a more detailed treatment than the simple approach presented above. Indeed, the use of the density matrix formalism is required in order to explain the linewidth of the CPT. In this case, the Schrödinger equation is solved for the Hamiltonian of Eq. 2.2 for the density with the addition o f a relaxation operator. The derived optical Bloch equations can be analytically solved (see [76] for a detailed treatment). In a first approximation, the linewidth of a CPT resonance is then well approximated by a Lorentzian lineshape [85]:

$$\Delta_{1/2} = \frac{\gamma_2 + \frac{\Omega_R^2}{\Gamma^*}}{\pi} \tag{2.50}$$

with γ_2 the relaxation rate of the hyperfine resonance (ground state relaxation), Γ^* the relaxation rate of the excited state and $\Omega_R \cong \Omega_1 \cong \Omega_2$ the optical Rabi frequency as defined in Eq. 2.1. Other broadening effect such as the Doppler broadening of the CPT resonance and the so-called time-of-flight broadening, due to the limited interaction time between the atoms and laser light field, can be neglected in cells with buffer gas. Indeed, due to the diffusive motion of the atoms in that case, the Doppler broadening is eliminated through the Dicke effect, when the mean free path between two collisions is smaller than the relevant wavelength given by the hyperfine transition [86] and the time-of-flight broadening is eliminated by the longer interaction time.

The results of this approach are in good agreements with experimental measurements in term of absorption linewidth. However, the absorption amplitude and the contrast observed experimentally require a more detailed model. Indeed, in a real system, some atoms are optically pumped to levels that are not involved in the CPT. This is especially the case when circularly polarized radiation is used, as required to observe ground-state field-independent transition. Moreover, the cell can often not be considered as optically thin media. Finally, this model does not take into account field intensity inhomogeneity. A more detailed approach, taking into account these effects in a four level model in an optically thick cell can be found in [85]. This model explains the observed contrasts. However it is no longer valid for high buffer gas pressure when optical absorption lines start to overlap as it is the case in MEMS atomic vapor cells. Indeed, in Eq. 2.4, Ω_1 is supposed to be only resonant with $|1\rangle \rightarrow |3\rangle$ and Ω_2 with $|2\rangle \rightarrow |3\rangle$ which does not remain a valid assumption in high buffer gas pressure cells.

2.4.2 Ground state relaxation in Rb cells

In Rb cell, the ground state population relaxation rate is given by:

$$\gamma_2 = \gamma_{\text{Rb-Rb}} + \gamma_{\text{Buffer gas}} + \gamma_{\text{Wall}} \tag{2.51}$$

where $\gamma_{\text{Rb-Rb}}$ is due to the Rb-Rb spin exchange collision, $\gamma_{\text{Buffer gas}}$ is due to the collisions with buffer gas and γ_{Wall} is due to the collisions with the walls.

For the D1 line of rubidium, the different relaxation rates can be expressed as follows:

Rb-Rb spin exchange collision   The spin exchange relaxation value is given by

$$\gamma_{\text{Rb-Rb}} = \frac{6I+1}{8I+4} \bar{v}_{\text{Rel Rb-Rb}} n_{\text{Rb}} \sigma_{\text{SE}} \tag{2.52}$$

with $I = 3/2$ the nuclear spin quantum number for rubidium, $\sigma_{\text{SE}} = 2.64 \cdot 10^{-14} \text{cm}^2$ the Rb-Rb spin exchange cross-section, and $\bar{v}_{\text{Rel Rb-Rb}} = \sqrt{\frac{8k_B T}{\pi \mu_{\text{Rb}}}}$ the mean relative Rb atoms velocity, with μ_{Rb} the reduced mass of rubidium.

Collisions with buffer gas   The relaxation rate due to the collisions with the buffer gas is given by the following formula which directly depends on the buffer gas pressure:

$$\gamma_{\text{Buffer gas}} = L_0 \bar{v}_{\text{Rel Rb-BG}} \sigma_{\text{Buffer gas}} \frac{P}{P_0} \tag{2.53}$$

with $L_0 = 2.65 \cdot 10^{25}$ m^{-3} the Loschmidt constant, $\bar{v}_{\text{Rel Rb-BG}} = \sqrt{\frac{8k_B T}{\pi \mu_{\text{Rb-GR}}}}$ the mean relative Rb-Buffer gas atoms velocity, $\sigma_{\text{Buffer gas}}$ the rubidium-buffer gas collision cross-section and P the pressure, with $\mu_{\text{Rb-BG}}$ the reduced mass of the rubidium and buffer gas. The values of the buffer gas cross section are given in table 2.4

Buffer gas	$\sigma_{\text{Buffer gas}}$ [cm^2]
Ar	$37 \cdot 10^{-23}$
N$_2$	$350 \cdot 10^{-23}$

Table 2.4: Buffer gas collision cross section for Rb for population relaxation [77]

Wall collisions   The cell wall collision relaxation rate is given by:

$$\gamma_{\text{Wall}} = \left[\left(\frac{2.405}{R}\right)^2 + \left(\frac{\pi}{L}\right)^2 \right] D_0 \frac{P_0}{P} \left(\frac{T}{T_0}\right)^{3/2} \tag{2.54}$$

with R the cell radius, L the cell length, D_0 the Rb atoms diffusion constant, T the cell temperature and P the cell pressure. The values of D_0 is given for Rb in Tab. 2.5.

Buffer gas	D_0 [cm^2 s^{-1}]
Ar	0.22
N$_2$	0.23

Table 2.5: Rubidium diffusion constant in different buffer gases at T$_0$=100°C and P$_0$=760 torr [87]

2.5 Atomic clock frequency stability

2.5.1 Allan deviation

Let $x(t)$ the clock frequency. This quantity is measured every time interval τ_0. Let us define the nth measurement as the mean clock fractional frequency y_n:

$$y_n = \frac{1}{\tau_0}(x(t_{n+1}) - x(t_n)) \tag{2.55}$$

The Allan variance is then defined as:

$$\sigma_y^2(\tau) = \frac{1}{2}\langle(\bar{y}_{n+1} - \bar{y}_n)^2\rangle \tag{2.56}$$

The Allan deviation is then defined as:

$$\sigma_y(\tau) = \sqrt{\sigma_y^2(\tau)} \tag{2.57}$$

This quantity allows to analyze the different noise sources in the device frequency in the time domain.

2.5.2 Short term frequency stability

2.5.2.1 Estimation of short term frequency stability

The Allan deviation of the clock signal can be linked to the detection noise and to the different parameters of the measured signal. The following formula gives the white frequency noise limit (in the case of white frequency noise) [88]:

$$\sigma_y(\tau) = \frac{N}{\sqrt{2} \cdot D \cdot \nu_{\text{Rb}}} \tau^{-1/2} \tag{2.58}$$

with N the total noise power, D the discrimination slope which is proportional to the derivative of the CPT signal and ν_{Rb} the transition frequency. The discrimination slope depends on the shape of the signal and on the exact modulation/demodulation parameters of the clock [77]. A good approximation is:

$$D \approx 2 \cdot \frac{A}{\Delta_{1/2}} \tag{2.59}$$

where A is the CPT amplitude and $\Delta_{1/2}$ the CPT FWHM. The noise power can be expressed as follow:

$$N = N_{\text{Dark}} + N_{\text{AM}} + N_{\text{FM}} \tag{2.60}$$

with the different components defined below. An estimation of the different noise sources affecting the short term frequency stability is given in Fig. 2.3 in function of the optical intensity.

2.5.2.2 Dark current

The dark current value is specific for each photodiode. It is due to the random generation of electrons and holes within the depletion region. It is typically in the order of a few pA. The following value is given for a Hamamatsu S10993-05GT photodiode.

$$N_{\text{Dark}} \approx 20\text{pA}/\sqrt{\text{Hz}} \tag{2.61}$$

2.5.2.3   Laser AM noise (RIN)

The intensity noise of the laser source directly impacts the clock performances as it induces directly a photocurrent variation. Typical random intensity noise (RIN) values for VCSEL are in the order of $8 \cdot 10^{-14}$/Hz. The associated noise is then for an optical power P and a responsivity R:

$$N_{\text{AM}} = \sqrt{RIN} \cdot P \cdot R \qquad (2.62)$$

2.5.2.4   Laser FM noise

The laser FM noise impacts the clock frequency stability through a FM-AM conversion process inside the cell. A detailed treatment can be found in [89, 90]. The power noise can be expressed as:

$$N_{\text{FM}} = \frac{2P_0}{\Delta_{1/2}^2} \delta f^2 \qquad (2.63)$$

with P_0 the output power, $\Delta_{1/2}$ the CPT linewidth and δf the frequency noise. The FM noise is typically in the order of $N_{VCSEL} = 5 \cdot 10^{-11}$W/$\sqrt{\text{Hz}}$ for $P_0 = 20~\mu$W [10].

2.5.2.5   Shot noise: the fundamental limit

The fundamental noise limit is given by the stochastic properties of light. For a light power P, the optical shot noise is given by $\sqrt{2h\nu P}$. However as the light is measure by a photodetector, the electric shot noise is a more more relevant parameter. Let R be the responsivity of the detector. Then the photocurrent is given by $I = P \cdot R$ and the electric shot noise is given by:

$$N_{\text{Shot}} = \sqrt{2eI} \qquad (2.64)$$

This noise source is usually taken into account in the laser RIN. Given equation 2.58, the short term fundamental limit is given by:

$$\sigma_{\text{Shot}}(\tau) = \frac{\sqrt{eI}}{D \cdot \nu_{\text{Rb}}} \tau^{-1/2} \qquad (2.65)$$

2.5.2.6   Figure of merit

A relevant parameter for clock optimization is given by the Figure of Merit (FoM) defined as:

$$FoM = \frac{C}{\Delta_{1/2}} \qquad (2.66)$$

where C is the CPT contrast, *i.e.* the ratio between the CPT signal. In the case of shot-noise limited detection, it is easy to show that [49]:

$$\sigma_y(\tau) \propto \frac{1}{FoM} \tau^{-1/2} \qquad (2.67)$$

2.5.3   Frequency shift and long-term stability

In a vapor cell, the natural resonance frequency of rubidium is perturbed by the environment and shifted by external effects. Therefor, on the mid to long-term, the frequency instabilities can be attributed to fluctuation or drift of these shifts implied by variations of the clock parameters on which they depend. These frequency shifts arise from three main physical sources: The buffer gas
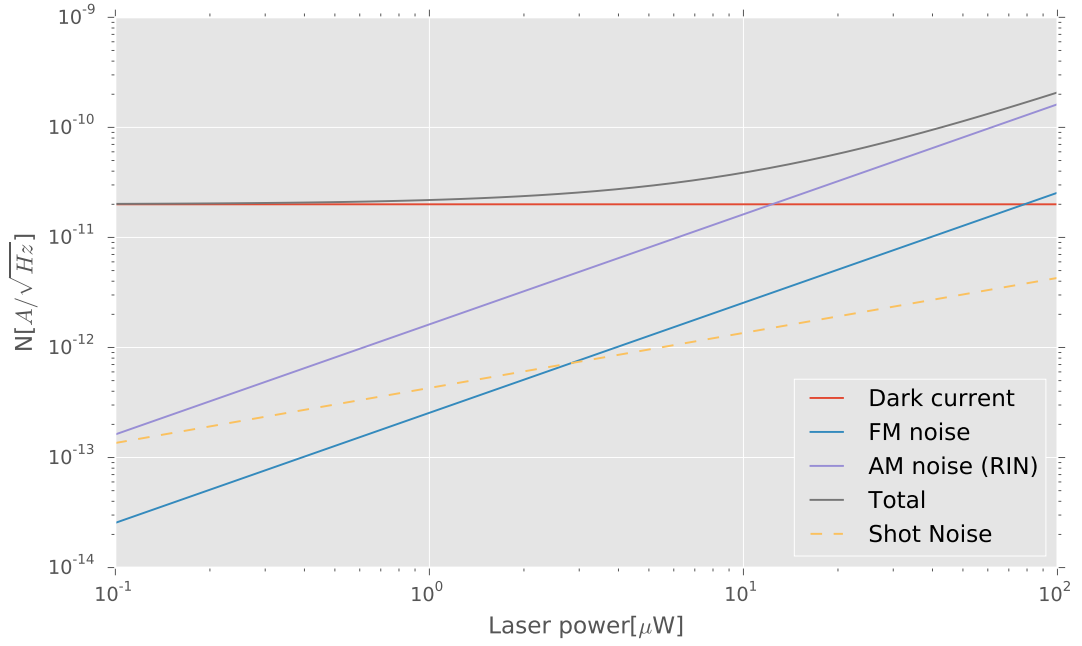
Figure 2.3: Noise sources affecting the short term frequency stability in function of the optical intensity calculated with the parameters of Sec. 2.5.2 for a laser beam of $D = 2$ mm. At a typical laser power of 15μW, the noise is dominated by the AM and dark current contributions.

induced shift, the light shift and the second order Zeeman shift [33]. The total shift of these effects being respectively in the order of 1000, 100, 10 Hz in a typical clock. Here are detailed these effects and the different implied sensitivities. Other sources of frequency shift and in particular spin-exchange frequency shift can be neglected since a population imbalance is not created at the first order by CPT with a bichromatic interrogation using equal laser intensities [91].

2.5.3.1 Buffer gas induced shift

The frequency shift produced by the buffer gas on the hyperfine frequency is due to the small phase shift in the dipole momentum accumulated over the collisions between the buffer gas and the rubidium atoms. Experiment showed that light atoms (He, Ne, N_2) produce a positive frequency shift as the Pauli forces are dominant and heavy atoms (Ar, Kr, Xe) produce a negative frequency shift as the Van der Waals forces are dominant [92]. It results in a complicated integral which is in practice approximated in a limited temperature range by the empirical formula [77, 93]:

$$\Delta\nu_{\text{Buffer Gas}} = P_0[\beta + \delta(T - T_0) + \gamma(T - T_0)^2] \tag{2.68}$$

Where β, δ and γ are coefficients that can be found in the literature (see Tab. 2.6) for a given reference temperature T_0 and P_0 is the corresponding buffer gas pressure.

Based on these consideration, there exist buffer gas mixtures for which the first order buffer gas temperature shift is canceled. Indeed, by choosing gases with an opposite temperature first order temperature dependance, a so-called inversion temperature can be found. This temperature can be tuned by adjusting the ratio between the two buffer gases. Atomic vapor cells are commonly filled with such a mixture (Ar/N_2 for example) in order to remove the first order thermal frequency

Gas	β [Hz·torr^{-1}]	δ [Hz·torr^{-1}·K^{-1}]	γ [Hz·torr^{-1}·K^{-2}]
Ar	-59.7	-0.32	-0.00035
N$_2$	547.9	0.52	-0.0013
Ne	407.3	0.18	-0.0092
He	744.6	0.90	-0.0149

Table 2.6: Collisional shift coefficients for ^{87}Rb at $T_0 = 333$K [93, 94]

dependance at the operating temperature.

Cell barometric shift   The pressure inside the cell is sensitive to the variation of pressure outside of the cell due to the deformation of the cell membranes. For a cylindrical cell, this deformation can be analytically calculated: Let $w(r,\theta)$ be the bending profile of a circular membrane. For a pressure variation of ΔP between the two sides of the membrane, and clamped boundary conditions, the profile is given in function of the radius r and the angle θ by [95]:

$$w(r,\theta) = \frac{\Delta P}{64D} \left(a^2 - r^2\right)^2 \tag{2.69}$$

with D the flexural rigidity defined as

$$D = \frac{Et^3}{12\left(1 - v^2\right)} \tag{2.70}$$

with a the total membrane radius, t the membrane thickness, E the Young modulus and v the Poisson ratio.

The volume variation for the complete cell is given by integration of this deformation profile over the surface of the two cell's membranes:

$$\delta V = 2 \int_0^a \int_0^{2\pi} w(r,\theta) r\, d\theta\, dr = 2 \frac{\Delta P}{64D} \frac{2\pi a^6}{6} \tag{2.71}$$

The corresponding pressure change in the cell is given by:

$$\delta P = \frac{\delta V}{V} P = \frac{P \Delta P a^4}{96Dh} \tag{2.72}$$

with h the cell thickness.

2.5.3.2   Light shift

The intensity light shift (AC Stark shift) arises from the interaction of the atomic dipole momentum with the electromagnetic field. It is given by [96]:

$$\Delta \Omega_{LS} = -\frac{1}{4} \frac{\Omega_L - \Omega_R}{(\Gamma^*/2)^2 + (\Omega_L - \Omega_R)^2} (\Omega_1^2 - \Omega_2^2) \tag{2.73}$$

where $\Omega_L - \Omega_R$ is the optical detuning between the bichromatic laser frequencies and the two transitions frequencies. The light shift therefore takes the shape of a dispersive Lorentzian. In a true clock system, the value of the light shift coefficient is obtained by summing over all the atomic transition.

Intensity light shift   The intensity light shift coefficient is defined as:

$$\alpha(\nu_L, I) = \frac{\partial \Delta \Omega_{LS}}{\partial I} \tag{2.74}$$

Typical values for the D1 line of ^{85}Rb are in the order of 80 Hz·mW^{-1}·cm^{-2} for a full band modulated VCSEL in a Ar-Ne cell servo controlled to the maximum of absorption [97].

Frequency light shift   The frequency light shift coefficient is defined as:

$$\beta(\nu_L, I) = \frac{\partial \Delta \Omega_{LS}}{\partial f_L} \tag{2.75}$$

No typical values were reported for Rb in the literature to my knowledge. For Cesium in a Ne cell, a value of -20 mHz/MHz was reported in [98] for the D2 line and a value of -11 mHz/MHz was reported in [99] for the D1 line.

2.5.3.3   Magnetic field shift

Variation of the magnetic field can also affect the clock frequency through the second order Zeeman effect (see Sec. 2.2.3) The frequency shift due to a change ΔB of the magnetic field can be calculated from Eq. 2.34 as:

$$\Delta \nu_{\text{Mag. Field}} = \frac{\partial \Delta \nu_{\text{clock}}}{\partial B}\bigg|_{B=B_{\text{op.}}} \Delta B \tag{2.76}$$

where the values for $\Delta \nu_{\text{clock}}$ are given in Tab. 2.1 and $B_{\text{op.}}$ is the constant magnetic field applied to the cell to lift the Zeeman sublevel degeneracy. From this equation and from Eq. 2.34, it can be seen that the sensitivity of the clock transition to magnetic field changes is proportional to the total magnetic field. It is therefore better for clock stability to work at low magnetic field. In practice, the applied field is therefore set to be sufficient to well discriminate the sub-Zeeman levels.

2.5.4   Influence of the physical parameters on the short term stability

2.5.4.1   Optical power

The optical intensity has two main contributions to the cell frequency stability: first, it affects the different noise sources (see Fig. 2.3) where the lower the light power, the better. Secondly, it affects the discrimination slope of the CPT signal (see Eq. 2.50) where the higher the light power, the better. Therefore, the optimal power is a compromise between these two effects and depends on the cell temperature and size and of the buffer gas pressure. It can then be experimentally optimized.

2.5.4.2   Buffer gas pressure

The buffer gas pressure affects the frequency stability through the CPT linewidth (see eq. 2.50) through the relaxation rates. Fig. 2.4 shows γ_2 as a function of the buffer gas pressure. The value is minimal for buffer gas pressure in the order of 300 to 400 torr. However, lower pressures are used in practice. Indeed, as the optical lines are also broadened by the buffer gas the different excited states absorption lines are mixed which decreases the efficiency of the optical pumping.

2.5.4.3   Operation temperature

The cell temperature mainly affects the short term stability with its influence on the absorption coefficient through the atomic density (see Sec. 2.3.3). The cell temperature also influences the CPT
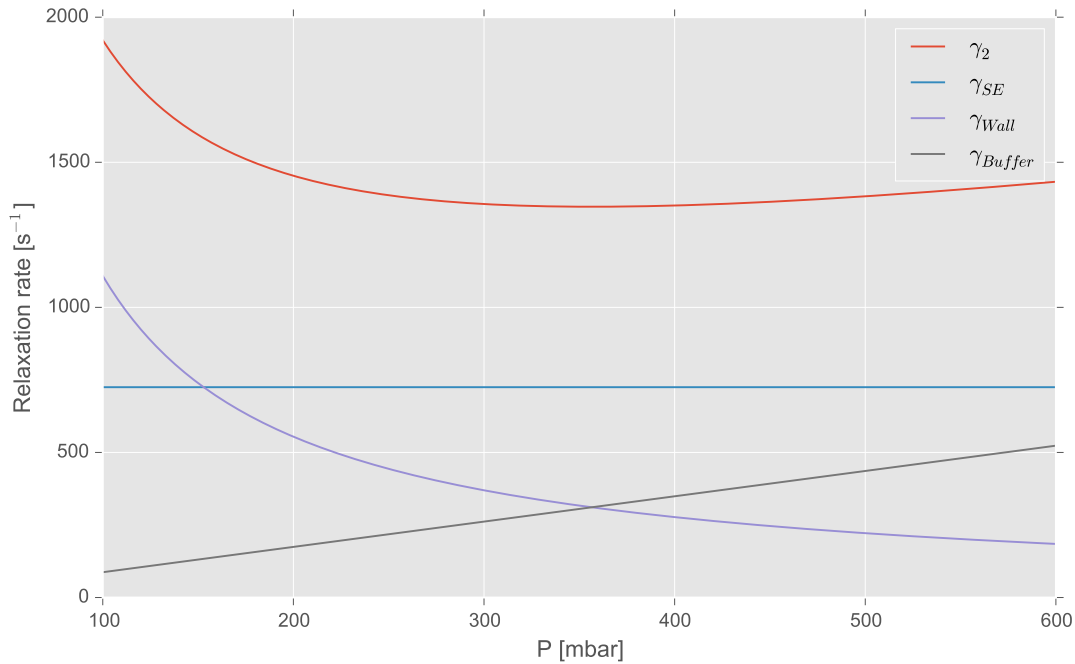
Figure 2.4: Ground population relaxation rate in function of the buffer gas pressure calculated with the parameters of Sec. 2.5.2 for a cell of $L = R = 1$ mm at 85°C

linewidth and amplitude with the Rb-Rb and Rb-Buffer gas collision through the relative velocity of the atoms. For MEMS (mm-size) atomic vapor cells, the temperature is typically higher than for macroscopic (cm-size) cells in order to reach a sufficient atomic absorption on the lower thickness and must be experimentally adjusted. Moreover, the buffer gas mixture has to be optimized in function of the cell temperature. (see Sec. 2.5.3.1).

2.6 Requirements for rubidium cells for chip scale atomic clock

The atomic vapor cell being at the heart of CPT atomic clocks, the requirements for the MEMS cell can be extracted from the requirements for a full chip scale atomic clock. In the following, a critical review of the overall clock requirements will be done. Deductions from these on the atomic vapor cell will then be given.

2.6.1 Overall clock requirements

The frequency stability requirements for a chip scale atomic clock for spatial applications are given by ESA[1]. The relevant requirements are summarized in Tab. 2.7. For each requirement, a remark is added whether it is fully or partially applicable for the cell design.

---

[1]See ESA technical document "Statement of Work: Miniaturized Timing Source (mTS)", Appendix 1 to ESA ITT AO/1-8048/14/NL/GLC, private communication

Power Consumption		
Parameter	**Value**	**Remark**
Power consumption during warm-up	≤ 200 mW	Partially applicable
Power consumption over the operating temperature range	< 150 mW	Partially applicable
Environmental conditions		
Parameter	**Value**	**Remark**
Operating temperature	-20 to 60°C	Applicable
OFF mode temperature	-55 to 85°C	Applicable
Lifetime	15 years	Applicable
Electrical parameters		
Parameter	**Value**	**Remark**
Stabilization time	< 30 days	Applicable
Output Frequency accuracy, all effects included (*i.e.* aging over lifetime, environmental, retrace)	$< 10^{-8}$	Partially applicable
Output Frequency Retrace after warm-up time in stable environmental conditions	$< \pm 5 \cdot 10^{-11}$	Applicable
Frequency Drift	$< \pm 10^{-11}/\text{day}$	Applicable
Long Term Frequency Drift (After 3 months of operation)	$\pm 10^{-10}/\text{month}$	Applicable
Short Term Frequency Stability	≤ 30 days	Applicable
1 s	$2.5 \cdot 10^{-10}$	
10 s	$8 \cdot 10^{-11}$	
100 s	$2.5 \cdot 10^{-11}$	
1000 s	$8 \cdot 10^{-12}$	
Long Term Frequency Stability		Applicable
1000 - 100000 s	$1 \cdot 10^{-11}$	
Frequency sensitivity to temperature	$< \pm 7 \cdot 10^{-12}/°\text{C}$	Partially applicable
Physical parameters		
Parameter	**Value**	**Remark**
Mass	< 100 g	Partially applicable
Volume	< 20 cm^3	Partially applicable

Table 2.7: Full clock specification target

2.6.2 Critical review of the requirements

2.6.2.1 Frequency stability

The short term frequency stability is mainly driven by the atomic signal detection noise, linewidth and amplitude. The last depends on the cell parameters such as the shape of the cavity, the buffer gas pressure and the operating temperature.

On the contrary the medium to long term frequency stability is mainly dictated by so called Flicker frequency modulation noise. This noise is not directly dependent on the cell properties. However, any periodic fluctuation can degrade this noise floor. The cell must therefore be as less sensitive as possible to any environmental change such as temperature variation.

2.6.2.2 Temperature

The clock must be able to operate between - 20 to 60°C. As the cell can only easily be heated in an atomic clock, the cell operating temperature must be located above 70° C. Moreover, in this range of temperature, the clock must be less sensitive than $7 \cdot 10^{-12}/$°C and the mid-term frequency stability must be sustained (see above). This requirement implies that the clock frequency dependence to the temperature for any part of the clock must be minimized. For the cell, the buffer gas pressure must therefore be controlled such that the working temperature is at the inversion point of the buffer gas frequency shift.

2.6.2.3 Alkali migration

When the atomic cell is heated, the alkali metal is known to condensate on the coolest part. When this part is the cell window, it affects the cell transmission and can influence the full clock frequency stability through the light-shift effect. Moreover, if this migration of the alkali happens during the clock OFF mode, as the temperature range goes higher than the rubidium melting point, this can affect the frequency retrace. In this case, the migration on the cell walls has to be compensated within the warm-up time.

A common solution is to heat the windows of the cell at a temperature slightly higher than the rest of the cavity. This technique is however hard to implement for MEMS cells. Another solution is the Au micro-disc presented and treated in detail in Sec. 3.5.

2.6.2.4 Frequency drift

The frequency drift of the clock is mainly given by the cell intrinsic frequency[2] drift and by the aging of the different components of the clock. For the cell, it relies on maintaining a constant buffer gas pressure and mixture [33]. The last can vary only through a leaking of the cavity or permeation into the cavity materials (see for example [100] for a description of that last phenomena).

It is possible to extract specifications in terms of hermeticity based on the specifications of maximal frequency drift. In the following, hermeticity requirements for the cell will be extracted supposing that the drift only arises from the buffer gas pressure variation. This is of course not true in a real clock but it give an order of magnitude of the performances that must be achieved by the cell.

The frequency shift as a function of the cell pressure is given by Eq. 2.68 Taking a standard buffer gas mixture with $P_{Ar}/P_{N_2} = 1.3$ and 150 mbar at 333 K [39], the working temperature is given by the inversion point of the cell temperature dependance, in this case, $T = 95$°C. At this temperature, the pressure shift coefficient is $\delta \nu / \delta P = 211$ Hz/mbar. For a frequency shift $\delta \nu / \delta t$, the corresponding

---

[2]See Sec. 4.1.2 for a definition of "intrinsic frequency".

leak rate is then given by:

$$l = \frac{\delta P \cdot V}{\delta t} \tag{2.77}$$

Taking cylindrical cell of $R = L = 1$ mm, the drift requirement of $\delta v/\delta t = 1 \cdot 10^{-10}/\text{month} \cdot v \equiv 2.63 \cdot 10^{-7}$ Hz/s therefore corresponds to a leak rate of $l = 1.75 \cdot 10^{-10}$ mbar l^{-1} s. It is important to note that this maximal leak rate value includes both permeation and true leaking of the cell.

2.6.2.5 Minimal windows thickness

The cell windows thickness can be limited by two long-term effects: the buffer gas shift due to the gas permeation inside the glass and the barometric shift: The pressure inside the cell is sensitive to the variation of pressure outside of the cell due to the deformation of the cell windows. As the first source of shift depends linearly with the wall thickness, it is more interesting to play with other parameters such as, for example, the glass composition to control it. We will therefore only focus on the barometric shift in the following.

Using the pressure shift value of $\delta v/\delta P = 211$ Hz/mbar calculated in Sec. 2.6.2.4 and based on Eq. 2.71 and Eq. 2.72, the frequency change due to the barometric effect on the cell windows can be calculated as a function of the windows thickness. The results are presented on Fig. 2.5. Now, supposing a pressure change of 1 bar in the outside of the cell during the cell lifetime (15 years) and a constant pressure inside the cell, a minimal window thickness can be estimated, supposing that the outside pressure change is constant and that the maximum drift induced by the barometric shift is $10^{-11}/\text{day}$. In this case, a total shift of 123 Hz for 1 bar pressure change is the maximal limit. This is realized for a window thickness of approximately 16 μm for Sapphire or 33 μm for Pyrex. For a Pyrex window of 200 μm which is the minimum wafer thickness for easy handling, the barometric frequency shift is 3 order of magnitude under this value. Moreover, the cell is supposed to be in a vacuum environment during the clock lifetime and a variation of 1 bar is well above what could be tolerated in this case. Therefore, one can conclude that the barometric shift is not the limiting factor for MEMS atomic vapor cells windows thickness and can be neglected. Indeed, other factors such as wafer handling capabilities or gas permeation will limit the thickness of the windows to a minimum of a few tenth of μm.

2.6.2.6 Lifetime

The clock lifetime must be at least 15 years. This implies that the cell lifetime must also be greater than 15 years. This topic is treated in detail in Chap. 5. However, the 10 years industry standard is used as baseline in this case.

2.6.2.7 Harsh environment

The cell must be able to sustain conditions specific to the space environment. The cell must therefore not be damaged by temperature from - 55 to 85°C.

2.6.2.8 Power consumption

The clock consumption requirement includes the cell heating and the laser operation. These requirements mainly rely on the clock thermal design. However, the total consumption can be limited by lowering the cell operating temperature and the laser power to some extent.
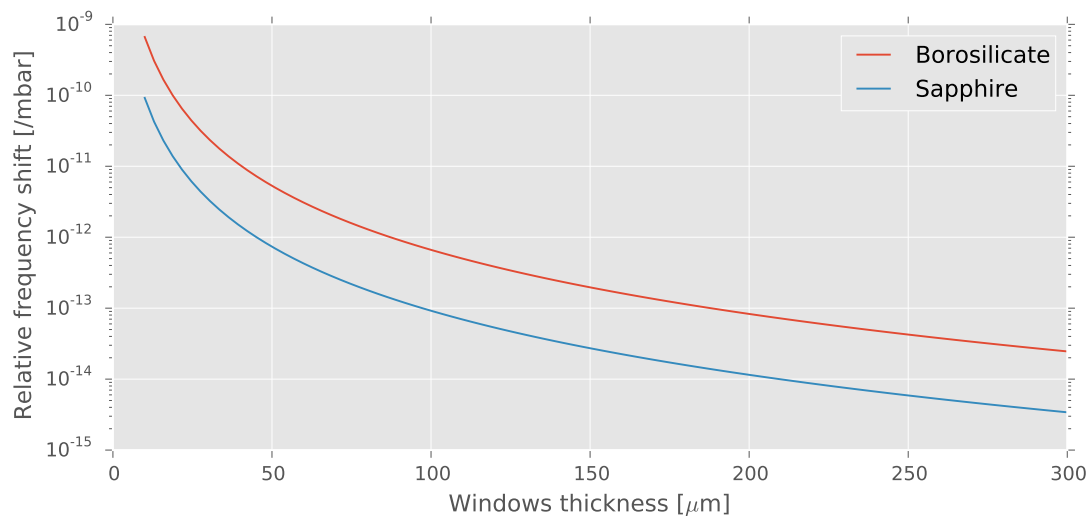
Figure 2.5: Barometric relative frequency shift coefficient for ^{87}Rb in a cylindrical cell with a radius of 1 mm and a thickness of 1 mm for Pyrex and sapphire. The cells is supposed to be filled with 150 mbar of Ar/N$_2$ buffer gas with a ratio of 1.3

2.6.2.9 Size and weight

The clock weight must be lower than 100 g and the size must be lower than 20 cm^3. This implies that the cell must be as light and as small as possible while fulfilling the other requirements.

In summary, the main requirements on the atomic vapor cells are the following:

- Full clock short term stability better than than $2.5 \cdot 10^{-10} \tau^{-1/2}$ until 1000 s

- Full clock drift below 1×10^{-10}/month

- Leak rate below $1.75 \cdot 10^{-10}$ mbar l^{-1} s

- Lifetime greater than 15 years

- Operating temperature greater than 60°C

- Minimization of cell sensitivity to temperature

- Design compliant with alkali migration during ON and OFF mode

- Cell must sustain harsh environment

- Minimization of power consumption

- Minimization of total cell size and weight
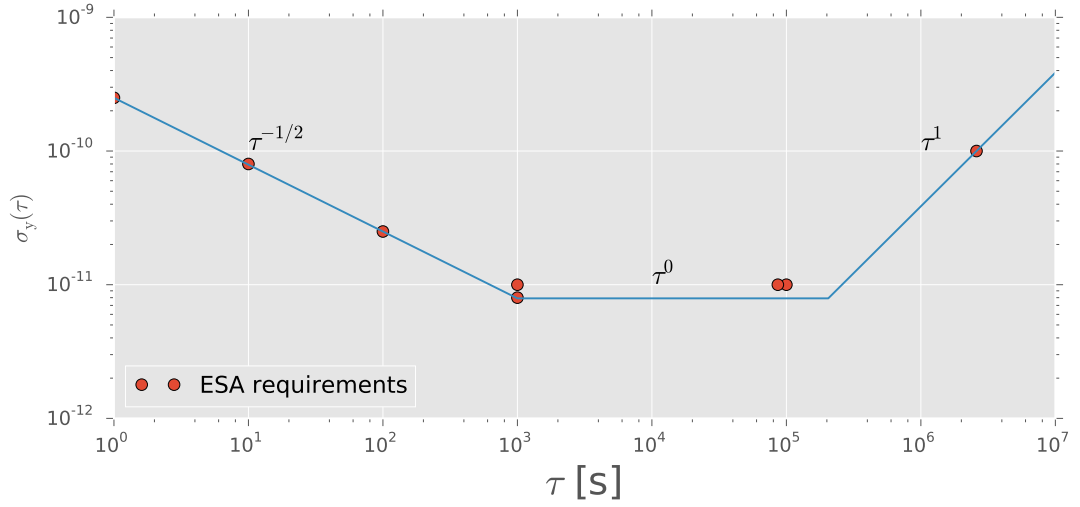
Figure 2.6: Full clock frequency stability (Allan deviation) requirements: ESA requirements (red) ; extrapolation on full time range based on the most stringent requirements (blue)

2.7 Nuclear magnetic resonance in alkali vapor cells

Besides CSACs, alkali vapor cells have applications in atomic sensors such as nuclear magnetic resonance gyroscopes (NMRGs). In this case, a noble gas is used as rotation sensor and the shift of the Larmor precession frequency in a static magnetic field is sensed to measure the rotation. The noble gas nuclei are polarized by optical pumping through spin-exchange collisions with the alkali atoms. The alkali atoms are then used to sense the macroscopic polarization of the nobel gas. A complete review of the subject of micro-gyroscopes can be found in [101] and a detailed review if NMRGs in [102]. Here is described the general working principle of NMRGs. In particular the description is inspired from [103].

2.7.1 Nuclear magnetic gyroscopes: general principle

Elements with an even atomic number Z possess a non-zero nuclear spin I only if the mass number A is odd. This is in particular the case for Xe where $Z = 54$. In this case, the ^{129}Xe (26.4% natural abundance) and ^{131}Xe (21.2% natural abundance) possess respectively a nuclear spin of 1/2 and 3/2. Associated with each nuclear spin is a magnetic moment which coexists with the angular momentum of the nucleus. This magnetic moment[3] $\boldsymbol{\mu}$ is given as a function of the angular momentum $\mathbf{I}$ as:

$$\boldsymbol{\mu} = \frac{g_I \mu_N}{\hbar} \mathbf{I} = \gamma \mathbf{I} \tag{2.78}$$

where g_I is the nuclear g-factor, μ_N the nuclear magneton and γ is the gyromagnetic ratio. In a magnetic field $\mathbf{B}$, torque is applied to the nucleus:

$$\frac{\mathrm{d}\mathbf{I}}{\mathrm{d}t} = \boldsymbol{\mu} \times \mathbf{B} \tag{2.79}$$

---

[3]The subscript present in Sec.2.2.2 is omitted here

These two equation therefore describe the precession of μ about the direction of the magnetic field B at the Larmor frequency:

$$\omega_L = \gamma B \tag{2.80}$$

Now, if the measuring coordinate system is rotation with an angular rate ω_r, the the Larmor precession frequency in the rotation frame will be:

$$\omega_L' = \omega_L - \omega_r \tag{2.81}$$

By measuring this shifted frequency and comparing it to the unperturbed Larmor frequency, it is therefore possible to extract the rotation frequency of the coordinate system. This principle is used in NMRGs in order to deduce the rotation angle. Tab. 2.8 gives the values of the gyromagnetic ratio for both Rb and Xe most common isotopes.

Element	$\gamma[\text{Hz}/\mu\text{T}]$
^{85}Rb	4665
^{87}Rb	6998
^{129}Xe	-11.77
^{131}Xe	3.516

Table 2.8: Gyromagnetic ratio for Rb and Xe most common isotopes

2.7.2 Spin-exchange optical pumping
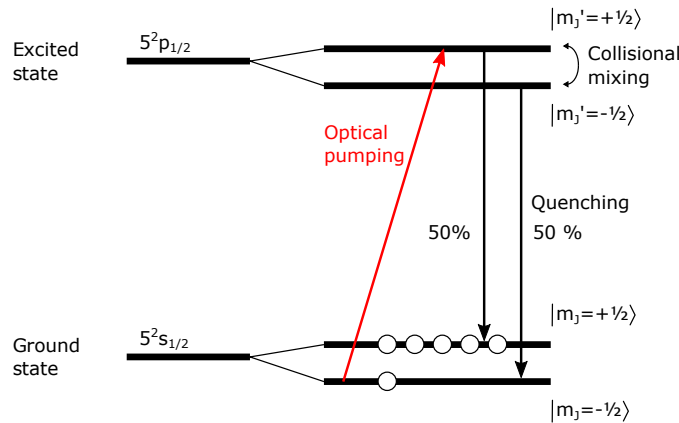
Figure 2.7: Polarization of idealized Rb vapor (no nuclear spin) by D1 optical pumping with σ_+ light

In order to measure the Larmor precession of the Xe atoms, a significant part of the atoms must be polarized and precess collectively in a static magnetic field. This polarization is realized by spin-exchange optical pumping (SEOP). A modern review of this technique can be found in [104]. Here, only a general overview is given. SEOP can be described in two steps: first the alkali metal vapor must be polarized. This is done by optical pumping. Then the polarization of the alkali vapor must be transferred to the noble gas. This is realized by spin-exchange collisions.

The process of Rb vapor optical pumping is as follow (see Fig. 2.7). Let us consider the $5^2s_{1/2} \rightarrow 5^2p_{1/2}$ transition of Rb (D1 line at 795nm). Let us suppose that a laser beam, resonant with this transition is shone onto the atomic vapor. Here $J = 1/2$ for both the ground and the excited

state. In the case of σ_+ polarized light, the light transfers its angular momentum to the atoms. This means that atoms in the $m_J = -1/2$ state are pumped in the $m_J' = +1/2$ state. Now if the excited populations are rapidly equalized by collisional mixing with buffer gas and if quenching [77] repopulates the two ground-state levels with nearly equal probability, all the atoms are eventually pumped in the $m_J = +1/2$ ground state. This assumption is however valid under a few conditions [104]: (i) circularly polarized light is used, resonant with the Rb D1 line. (ii) pressure broadening of the absorption lines makes the hyperfine structure unresolved. (iii) quenching effect eliminates radiation trapping as a source of relaxation. (iv) the nuclear spin polarization is conserved in the time interval of a full pumping/relaxation process. The collisional spin-exchange process from the alkali to the noble gas atoms occurs then through two main path: formation and breakup of van der Waals alkali metal - noble gas molecules and binary collisions between an alkali metal atom and a noble gas atom.

2.7.3 The alkali metal used as magnetometer

Once polarized by SEOP, the Xe magnetization must be measured. This is done by the so-called Dehmelt method [105] reported in 1957, where the modulation of light by the precession of the absorbing atoms is used. This method where the alkali metal is now used as a low field optically pumped magnetometer was first used with rubidium by Bloom [106] in 1962 and was then applied to the detection of noble gas NMR signal by Grover [107] in 1978.

Let us now consider the Rb vapor pumped as in Fig. 2.7 and let us consider the relaxation of the ground state. If $\mathbf{M}_0$ is the saturated absorption, $i.e.$ all atoms in the $|m_J = +1/2\rangle$ ground state and $\mathbf{M}_{\text{Rb}}$ is the net magnetic moment of rubidium[4], the absorption of σ_+ light is:

$$A \propto (\mathbf{M} - \mathbf{M}_0) \cdot \mathbf{k} \tag{2.82}$$

where $\mathbf{k}$ is the light beam vector. Now if the pumping rate is given by $1/\tau_p$ and the relaxation time is given by τ_r, the rate equation for the net magnetic momentum writes:

$$\frac{d\mathbf{M}}{dt} = \frac{1}{\tau_p}(\mathbf{M}_0 - \mathbf{M}) - \frac{\mathbf{M}}{\tau_r} + \gamma \mathbf{M} \times \mathbf{B} \tag{2.83}$$

with $\mathbf{B}$ the total magnetic field Redefining

$$\frac{1}{\tau} = \frac{1}{\tau_p} + \frac{1}{\tau_r} \qquad \text{and} \qquad \mathbf{M}_0' = \mathbf{M}_0 \left(\frac{\frac{1}{\tau_p}}{\frac{1}{\tau_p} + \frac{1}{\tau_r}} \right) \tag{2.84}$$

Eq. 2.83 writes:

$$\frac{d\mathbf{M}}{dt} = \frac{1}{\tau}(\mathbf{M}_0' - \mathbf{M}) + \gamma \mathbf{M} \times \mathbf{B} \tag{2.85}$$

Let us now show qualitatively how this system can be used as a magnetometer. We consider a magnetic field $\mathbf{B}_y$ oriented along the $\hat{\mathbf{y}}$ axis and a light beam vector $\mathbf{k}$ oriented in the $\hat{\mathbf{z}}$ direction. Fig. 2.8 shows the behavior of the collection of Rb magnetic moment and the net magnetic moment as a function of the intensity of the $\mathbf{B}_y$ field. The atoms are pumped in the $\hat{\mathbf{z}}$ direction. As their magnetic moment rotates under the effect of the magnetic field, they relax at a rate $1/\tau$. For $\mathbf{B}_y \approx 0$, the net magnetic moment stays parallel to $\hat{\mathbf{z}}$ and $\mathbf{M}$ approaches the saturation value $\mathbf{M}_0'$ (Fig. 2.8 - left). The light absorption is at its minimum according to Eq. 2.82. As soon as $\mathbf{B}_y$ becomes non-zero, $\mathbf{M}$ starts to rotate (Fig. 2.8 - center) and the light absorption increases. When $\mathbf{B}_y$ becomes too strong, the

---

[4]The subscript is omitted for readability in the following

magnetic moments have time to make many turns before relaxing. They are therefore spread in an isotropic fashion in the x-z plane and the net magnetic moment tends to zero (Fig. 2.8 - right).
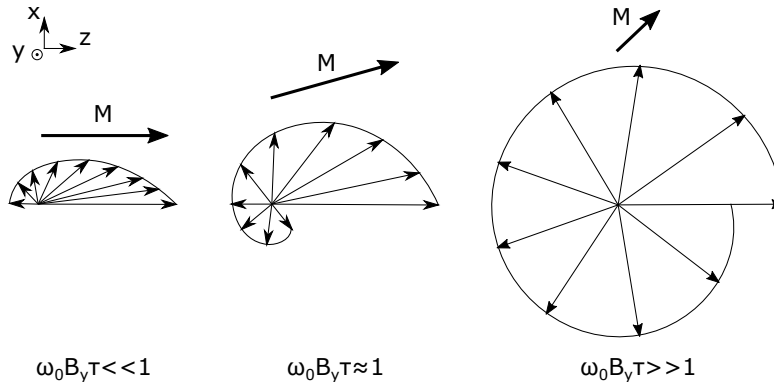
Figure 2.8: Alkali metal dipole ensemble in three cases depending on the magnetic field

Now, let us sum a small amplitude AC magnetic field to $\mathbf{B}_y$ in the $\hat{\mathbf{y}}$ direction at a frequency $\omega \gg 1/\tau$. For $\mathbf{B_y} \approx 0$, the net magnetic field $\mathbf{M}$ starts to oscillate symmetrically about the $\hat{\mathbf{z}}$ axis. (see Fig. 2.9 - left) As an effect, its projection on $\hat{\mathbf{z}}$, $\Delta\mathbf{M}_z$ oscillates at 2ω and so does the absorption, according to Eq. 2.82. As soon as $\mathbf{B}_y$ becomes non-zero, the oscillation axis of $\mathbf{M}$ starts to rotate and the amplitude of the projection on $\hat{\mathbf{z}}$ increases and becomes asymmetrical, which effect can be detected on the light absorption. Now by demodulating the transmitted light at a frequency ω, the output signal is proportional to the $\mathbf{B_y}$ magnetic field making this system a magnetometer.

2.7.4   Detection of the Xe relaxation

Now let us come back to the Xe atoms. If a magnetic field is suddenly applied by, for example a field-switch technique, to a SEOP Xe nuclear spin ensemble, they start to processes in phase around the static magnetic field (see Sec. 2.7.1) and to relax at a rate $1/T_2^*$. This spin ensemble creates in turn a macroscopic magnetization which can be sensed by the Rb used as magnetometer to measure the relaxation rate.

Let us suppose that the Xe atoms were pumped by SEOP until a time $t = 0$ and that they reached the steady-state. In this case, both the Xe and Rb magnetic momentum are aligned with the $\hat{\mathbf{z}}$ direction. Let us now switch on a static magnetic field $\mathbf{B}_0$ in the x-z plane and an AC magnetic field in the y direction. Under the effect of $\mathbf{B}_0$, the Xe magnetic momentum start to rotate at its Larmor frequency ω_L and create a macroscopic magnetization $\mathbf{B}_{Xe}$. The y component of this magnetization is sensed by the Rb used as a magnetometer (see Sec. 2.7.3) and modulates the error signal measured by the magnetometer. The Xe coherence time T_2* can be measured as the exponential decay envelope of this signal. A few comments can finally be added with respect to this measurement method.

- The x component of the $\mathbf{B}_0$ static magnetic field rotates the Rb magnetic momentum and influences the light absorption. However, this effect is fixed in time and only shifts the error signal measured after demodulation of the transmitted light.

- The AC magnetic field affects the Xe magnetic momentum too. However, as the gyromagnetic ratio and the decoherence rate are much lower for Xe than for Rb and the frequency chosen to be $\omega \gg 1/\tau$, the Xe "does not feel" the AC magnetic field.

- The field generated by the Rb atoms is sensed by Xe [3]. It must therefore be taken into account in measurements.
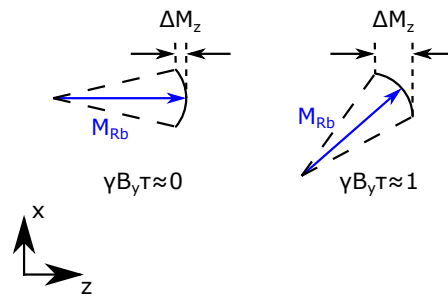
Figure 2.9: Oscillation of the alkali metal magnetic moment in zero and low field configurations

2.8 Conclusion

In this chapter, the relevant theoretical aspects for the fabrication of an atomic vapor cell were reviewed. The general working principle of a CPT clock was described in Sec. 2.1. The Rb atom structure was described in Sec. 2.2 and its optical absorption is described in Sec. 2.3.

The spectroscopy of the CPT resonance is described in Sec. 2.4. From this analysis, it was shown in Sec. 2.5 that, in the frame of CPT clocks, the different physical parameters such as the temperature, the buffer gas pressure and mixture inside the cell, the buffer gas leakage, the laser power and the clock noise sources as well as the cell dimension affect the clock long term and short term performances. It was also shown that a theoretical optimization of these cell parameters is difficult to realize due to the difficulty of calculating a precise CPT contrast. Nevertheless, this chapter gives the frame for the experimental optimization of these parameters during the cell fabrication process. Moreover, in Sec. 2.6, the requirement for a CSAC are analyzed. In particular, the buffer gas pressure shift values are used to calculate requirements in term of leak rate.

Finally, the theoretical aspects of NMR gyroscopes and in particular those relevant for the measurement of Xe relaxation time were reviewed in Sec. 2.7.

3 Microfabrication of atomic vapor cells

This chapter covers the different aspects related to the MEMS atomic vapor cells microfabrication activities. In the first section, the technological aspects are reviewed: the different materials that can be use for the core and the windows of the cell are investigated. The bonding technologies that can be used to seal the MEMS cell are then listed. The alkali metal dispensing techniques are described and finally the getters and the anti-diffusion coatings used to maintain a pure content inside the cell are analyzed. The second section describes in detail the approach chosen as novel alternative techniques for the fabrication of MEMS atomic vapor cells, *i.e.* Cu-Cu thermocompression bonding. The different steps of fabrication are described: the cavity design and etching, the substrate structuration, the copper layer deposition and the bonding parameters. The results of preliminary tests are then described as well as the final full cell realization. The third section describes in detail the two alkali dispensing techniques studied in the present work. The filling made with RbN_3 and Rb micro-pill filling are presented. The fourth section gives information about the deposition of the Al_2O_3 coating used as alkali anti-diffusion coating. Finally the fifth sections describes the fabrication of the CSEM patent pending gold micro-discs used as alkali condensation sites to enhance the long-term frequency stability of the cell.

3.1 Review of fabrication techniques and materials

3.1.1 Materials

One of the main property of interest for the fabrication of atomic vapor cell is the leak tightness and the manufacturability. Indeed, the intrinsic long term frequency stability[1] of MEMS cells is mainly affected by changes of the buffer gas pressure (see [33] and Sec. 2.68). This change of the buffer gas pressure mainly relies on the permeation in the cell wall and windows. Moreover, the cell lifetime can be limited by the reaction of the rubidium with the walls (see Chap. 5). It is therefore of great interest to review the different possibilities for the cell core and windows materials in order to find the optimal combination.

Due to the optical interrogation method, atomic vapor cells require a transparent light path at 795nm in order to allow the laser interrogation of the rubidium atoms. The cavity of the cell can, on the contrary, be made in any other non-magnetic material, as long as it does not react with rubidium. In the following, the few materials commonly used in vacuum technology that could be used for the cavity and the windows of atomic vapor cells are described [108].

---

[1]See Sec. 4.1.2 for a definition of "intrinsic frequency".

3.1.1.1 Glasses and other transparent oxides

Glasses are the most standard materials for the fabrication of transparent atomic vapor cells. Permeation of gases in glass was mainly studied in [109, 100] and showed that in general, the permeability is higher for high SiO_2 contents. Fig. 3.1 shows a comparison between different types of glasses. Other studies showed that rubidium diffusion in glass was the first limiting factor for rubidium lamps lifetime [110, 111, 112]. It is particularly a very relevant parameter in the case of MEMS atomic vapor cells as the surface to volume ratio is much higher than in a classical glass-blown cell.

Soft glass   This sort of glass has a typical low SiO_2 content and are composed of several other oxides. The melting point of soft glass is typically relatively low (370°C to 450°C) and their thermal shock resistance is poor. Moreover, soft glass are easily reduced by alkali metals [110] and can not be anodically bonded. They are therefore not good candidates for atomic vapor cells.

Hard glass   The SiO_2 content in hard glasses often exceeds 70%. The hardness of the material is typically increased by addition of another oxide such as Boron or Aluminum. There exist different hard glasses depending on the added oxide.

- **Borosilicate glass** Borosilicate glass is the most commonly used hard glass. Common commercial brands are Pyrex[®] and SCHOTT Borofloat[®] 33. It is the most commonly used glass for the fabrication of MEMS atomic vapor cells as it is a very suitable material for anodic bonding (see Sec. 3.1.2.1). Indeed, it has a high ion mobility and matches well the thermal expansion coefficient of silicon. Moreover, borosilicate glass presents a good resistance to alkali metal oxidation.

- **Aluminosilicate glass** This sort of glass can also be used for anodic bonding. First tests were reported for the fabrication of anodic-bonded cells [113]. Measures of the Helium diffusion showed a diffusion 100 times lower than for Pyrex[®].

- **Alkali-silicate glass** This sort of glass was reported in [111, 112] for the fabrication of rubidium lamps. The studies compare the used SCHOTT 8436 alkali-silicate glass to Corning 1720 aluminosilicate glass and show an improvement of a factor of two in terms of rubidium consumption due to diffusion. However the other physical properties of this type of glass were never reported to my knowledge.

- **Quartz** It is made of pure SiO_2 in crystalline structure. It is commonly used for macro vapor cells. However, as it cannot be anodically bonded, it is not a first choice for MEMS atomic vapor cells.

Sapphire   Sapphire (Al_2O_3) is characterized by a crystalline structure. Its amorphous form (Al_2O_3) is commonly used as anti-diffusion coating for UHV [108] and is therefore expected to show an extremely low diffusion constant. Centimeter-sized atomic vapor cells were successfully realized with this material [114]. As sapphire is transparent at 795nm it a a good candidate for the cells windows. The main drawbacks of sapphire are that it can not be anodically bonded in bulk form and that it is an extremely hard material. It can therefore only be machined using diamond tools or by laser. Moreover, etching of sapphire is difficult for the most common etchant [115]. Finally, it is important to note that, as sapphire is a birefringent material, if it is used as cell window, the crystal structure has to be oriented such that the clock interrogation laser follows the ordinary axis.
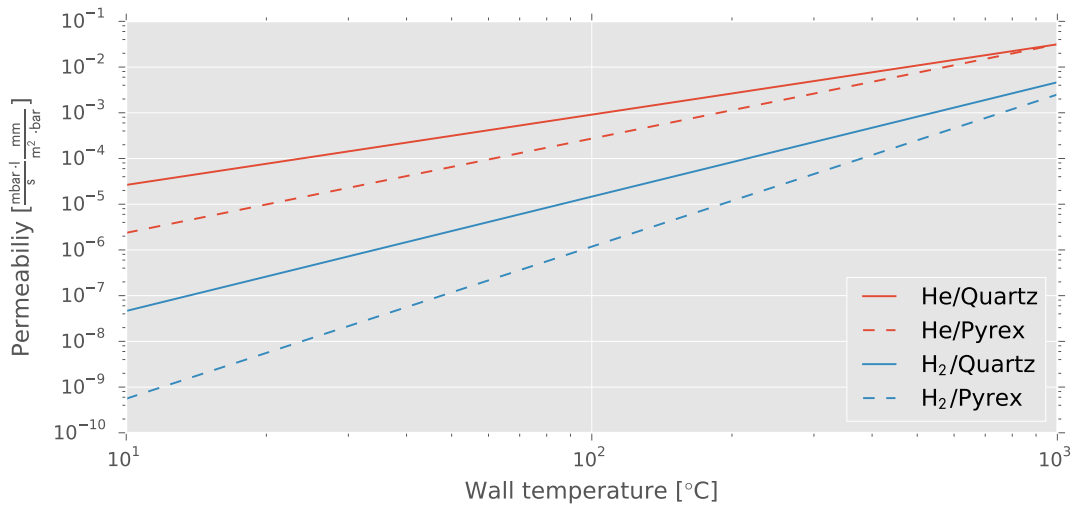
Figure 3.1: Permeability of quartz and Pyrex® to H_2 and He versus wall temperature - data taken from [108]

3.1.1.2 Ceramic materials

LTCC LTCC (Low Temperature Co-fired Ceramic) is an interesting alternative to Silicon for the fabrication of atomic vapor cells. LTCC is commonly used for vacuum encapsulation and is non-reactive with alkali metals. It was therefore used as cell cavity in [37]. The main advantage of LTCC over Silicon is that it allows a direct integration of the cell in a more general design of the atomic clock. Indeed, passive electronics can be included directly inside the LTCC layers. However, the miniaturization of the cell is limited by the processing of LTCC. Indeed, the processes do not allow to scale down the size as much as for Silicon and no sealing technique compatible with alkali filling was ever developed to my knowledge.

3.1.1.3 Transition metals

Metals are commonly used in MEMS technology as intermediate layers for different kind of bonding (see section 3.1.2). A detailed review of corrosion of metals by alkali metals can be found in [116, 117].

The best criterion in order to determine if a metal can be used for the cavity is to assess its solubility in the alkali metal. The solubility increases from the left to the right in the periodic table. Thus, the so called refractory metals and in particular metals from the Ti,V,Cr groups are the best candidates to contain alkali metals. The three metals commonly used as adhesion layers (Ti,Ta,Cr) are precisely part of these metals (see Sec. 3.1.2). Ni and Cu are at the limit in the transition metal group beyond which a compatible metal cannot be found. Moreover, heavier metals of their group show increasing solubility in alkali metals.

Based on these general rules, a detailed literature review on the Rb-metal systems was realized for metals presenting a technological interest. The results are presented in Tab. 3.1. The following criteria were assessed: Solubility of Rb in the metal, presence of an eutectic system (see Sec. 3.1.2.2) and presence of inter-metallic compounds. The outcome is that Al or Cu are materials commonly used in microfabrication that are compatible with Rb as well as Ti, Cr and Ta as adhesion layers.

Alloy	Solubility of metal in Rb	Solubility of Rb in Metal	Eutectic system	Formation of inter-metallic compounds	Note	Suitable for Rb atomic cells
Al-Rb [118]	extremely small	0.05 at.% @ 660°C	No	No		Likely
Au-Rb [119]	?	≈5%@100°C	Yes	Yes		No
Cr-Rb [116]	extremely small	extremely small	No	No	Eutectic temperature of 40°C	Yes
Cu-Rb [120]	extremely small	extremely small	No	No		Yes
In-Rb [121, 117]	non zero	see note	Yes	Yes	Eutectic point virtually indistinguishable from melting point of pure elements	No [39]
Sn-Rb [122]	see note	?	Yes	Yes	Eutectic point virtually indistinguishable from melting point of pure elements	Unlikely
Ta-Rb [116]	extremely small	extremely small	No	No		Yes
Ti-Rb [116]	extremely small	extremely small	No	No		Yes

Table 3.1: Summary of the different Rb-metal systems for the most common solder metals

3.1.1.4 Other non-metals

Silicon Silicon is at the basis of MEMS fabrication. The first microfabricated atomic vapor cells were realized with silicon for the cavity material and it is still the main material used for this purpose. The main advantages of silicon is that it can easily be etched by DRIE, it has a crystalline structure which implies a low permeation to gases [123] and it can be anodically bonded.

Wafer bonding technologies can be sorted in three main groups depending if they are realized with or without an intermediate layer and on the nature of this layer. Techniques such as glass frit bonding, adhesive and epoxy bonding are realized with an insulating interlayer. In the other hand, soft solder, eutectic, transient liquid phase (TLP) or diffusion bonding are realized with the help of a conductive metallic interlayer. They both are opposed to fusion bonding or anodic bonding which don't require such a layer and where the two wafers are directly bonded to each other.

3.1.2 Bonding technology

Bonding technique	Temperature	Vacuum level	Chemical compatible with Rb
Anodic	300 - 450°C	0.01 mbar	Yes
Laser transmission	local	unknown	Yes
Glass frit	350-500 °C	1 mbar	Yes
Soft solder	150-450°C	0.01 mbar	Partial
TLP	400-1200°C	0.01 mbar	Partial
Diffusion	< 450°C	0.01 mbar	Partial
Eutectic	300-400°C	0.01 mbar	Partial
Adhesive	<200°C	1 mbar	No
Epoxy	Room temperature	No	No

Table 3.2: Comparison of the most common glass-silicon bonding technologies adapted from [124] and completed with data from [125] - the vacuum level given here only takes into account the hermeticity and not the outgasing of the bonding process

Table 3.2 summarizes the most common wafer bonding technologies and the achievable vacuum levels with their bonding temperature. The table is completed with a study of the chemical compatibility of the bonding technique with Rb (see below). From this first analysis, techniques such as adhesive bonding, transient liquid phase bonding or epoxy bonding can be discarded as they are not chemically compatible with Rb. In the following a detailed analysis of the different techniques is presented in order to further characterize their suitability for the fabrication of atomic vapor cells.

3.1.2.1 Direct bonding techniques

Anodic bonding Anodic bonding, also known as "field-assisted sealing" or "electrostatic bonding" was first reported in 1968 by Wallis and Pomerantz [126]. It was the first technology used for the fabrication of MEMS Alkali vapor cell which was introduced by NIST in 2004 [7] and was applied to most of microfabricated cells ever since.

Anodic bonding is an electrochemical process which consists in joining an alkali-containing glass such as Corning 7740 Pyrex® or Schott Borofloat® 33 to a silicon wafer. The temperature is raised to 300 to 450°C, so that the glass is sufficiently conductive. A high DC voltage (400 - 1000V) is applied [127]. Under the effect of the voltage, the positive ions contained in the glass (mainly Na^+) migrate toward the cathode, letting a cation-depleted layer at the interface with the silicon. Under

this high field, the negative O_2^- remaining ions move to the bond interface and react with the silicon to create SiO_2 bonds. This oxidation process completes the anodic bonding.

The bond strength depends on the bonding condition and on the wafers thickness. It is usually found in the range 5-45 MPa [127]. Moreover, non-bonded areas can easily be identified by visual inspection as they appear as gray areas or colored fringes.

The residual pressure inside an anodically bonded cavity is known to be higher than the pressure in the bonding chamber [128, 129]. This is due to the gas released from the inner surface of the cavity and the gas produced by the anodic bonding (mainly O_2). The gas pressure can vary from 1 mbar [130] up to 500 mbar for very small cavities [128]. However, leak rate tests realized under hydrogen atmosphere showed values as low as 10^{-15} mbar l/s [131].

Finally, it can be noted that the anodic bonding can be used to bond silicon to glass but also LTCC to silicon, in which case a specific LTCC material must be used [132], or even glass to glass, in which case a diffusion stopper must be used [133].

Fusion bonding   Fusion bonding or direct bonding is realized between two silicon wafers [127]. The two wafers are placed in contact, heated close to the silicon melting point and pressed together. The cleanliness and surface roughness of the silicon wafers are therefore critical. However, it is not applicable to glass or other transparent material and hence this technique is not suitable for atomic vapor cells.

3.1.2.2   Bonding with intermediate layer

Glass frit bonding   The basic principle of glass frit bonding is the use of glass as an intermediate bonding layer. The bonding processes is as follows [127]: First a glass frit paste is printed on one of the wafers. This paste is composed of low-melting-point glass milled into a powder, an organic binder and a solvent. When printed, the solvent dries and the binder polymerizes. The printed wafer is then heated in two steps (below 450°C) in order to burnout the binder and to pre-melt the glass. The second wafer is then put into contact with the first wafer and placed under pressure in order to realize the bonding.

It has been shown that the vacuum level inside cavities sealed by this technique cannot be lower than 1-5 mbar, the main limiting factor being the gas created by remaining organics of the glass frit paste in the cavity [127].

Adhesive bonding   Adhesive bonding is a technique which uses a polymer as an intermediate bonding layer [127]. As the bonding realized with this technique are not hermetic and the polymer is very likely to react with alkali metal, this technique is not suitable for atomic vapor cells.

Soft solder bonding   In soft solder bonding, two metals layers of the same element or alloy are deposited on the two wafers to be joint [124]. They are then placed in contact and heated at relatively low temperatures (150-450°C). This results in a melting of the two metal layers and to sealing. The wetting of the solder reduces the need for high pressure and fills the gap and non-planarities of the wafers. However, outgasing issues were observed for the soldering of microcavities (H_2O, H_2, O_2). In some cases, as the soldering temperature must remain relatively low, this technique is incompatible with getters which require a higher activation temperature. Moreover, the metals commonly used with this method (In, Sn, Pb, ...) are incompatible with alkali metal.

Eutectic bonding   An eutectic alloy is an alloy which has a lower fusion temperature than the compounds that it is composed of [134]. Eutectic bonding can be realized with Au-Si (363°C), Al-Ge (420°C), Au-Sn (280°C) and Al-Si (577°C) [135]. The process is the following: For Au-Si or Al-Si, an Al or Au layer is deposited at the surface of the glass wafer. The two wafers are then pressed

together and heated to a temperature slightly above the eutectic temperature. Upon cooling, an eutectic alloy forms up when reaching the eutectic temperature. For Al-Ge and Au-Sn a metal layer is deposited at the surface of the two wafers and the same process is applied. As for soft-soldering, the commonly used metals are incompatible with alkali metals.

Transient liquid phase bonding Transient liquid phase bonding or solid-liquid inter-diffusion bonding is a process that joins wafer with the help of two metal layer with a high-melting temperature and a metallic intermediate layer with a low melting temperature [127]. When heated, the intermediate layer melts and diffuses into the metalization where it forms intermediate compounds and bonds. As these compounds have higher melting point than the pure interlayer material, the remelting temperature of the soldering is higher than the bonding temperature. The candidates for the high-melting temperature material are Cu, Au, Ag, Co and Ni. The candidate for low-melting temperature materials are Sn, In and Hg. Here as well, the commonly used metals are incompatible with alkali metals.

Thermocompression bonding Thermocompression bonding, often called diffusion bonding, is a diffusion-based process. A metal (most commonly Al, Au or Cu) is deposited on the surface of the two wafers to be bonded.The two wafers are then pressed together and heated. As a consequence, metal atoms of the two lattices diffuse into the lattice of each-other without forming a liquid phase. The bonding time is relatively long as this is a diffusion driven process. However the melting point of a bonding realized with this technique will be much higher than the bonding temperature. Among the commonly used materials, Al and Cu are compatible with alkali metals. However, Al-Al thermo-compression bonding is known to be extremely difficult due to the difficulty to remove the aluminum oxide layer that rapidly grows at the surface when exposed to ambient atmosphere.

3.1.2.3 Localized bonding

The above bonding methods require a heating of the complete wafer in order to realize the bonding. However, there exist other bonding methods that only require a localized heating at the bonding area. A detailed review of these techniques was realized by Lorenz in 2011 [136]. The following is inspired and completed by more recent publications.

Microwave heating A dielectric material that has a low imaginary dielectric constant is transparent to Microwave radiation (200 kHz-20 GHz), however energy is deposited in high imaginary dielectric constant materials such as metals and some polymers [137]. This property is used in microwave local bonding in order to selectively heat certain regions of wafers: The silicon wafer is structured with a high dielectric constant material in order to design the bonding areas. The two wafers are then placed in contact and pressed together. They are then placed in a microwave field. The defined zones heat up and bond to the other wafer.

This technique was used for silicon to silicon selective bonding with Parylene [138, 139] and hermetic packaging of silicon to silicon with gold sealing layer [137]. However, as all materials with a high imaginary dielectric constant heat up during the bonding, this technique is not recommended for atomic vapor cells if pure alkali metal is present inside the cell. Indeed, the alkali metal will also heat up and vaporize. Therefore, this technique does not give any advantage in the case of MEMS atomic vapor cells.

Resistive heating Resistive local bonding was developed by Chen et al. since 2000 [140, 141, 142, 143]. In this technique, the bonding energy is provided in a highly localized way by micro-heaters which are deposited in the bonding area. Application of this technique was realized with various bonding methods such as eutectic fusion bonding and solder bonding.

However, the main drawback of this method is the up scaling to a wafer level. Indeed, as each micro-heater requires a large amount of current, the electric tracks will be significantly large in order to provide sufficient current to all the vapor cells sealing. The implementation would therefore require further investigation in term of feasibility.

Induction heating Induction heating for local bonding is based on the same principle as resistive heating bonding with the difference that the electric current is induced inside a bonding loop via an oscillating magnetic field [144, 145, 146, 147].

This technique was used by Yang et al. for silicon to silicon with a lead-tin interlayer soldering [144]. Hu et al. applied the same principle to glass to silicon and glass to glass bonding [145] and finally Chen et al. realized a hermetic package for a temperature sensitive gyroscope in a ceramic package [146].

In the case of pure alkali metal, this technique would not be suitable as the metal would heat up due to induction. However, it may be used for alkali-metal azide but does not provide any advantage as compared to conventional technique such as diffusion bonding as the cell content is not thermal sensitive.

Laser joining Laser bonding was a topic of high interest during the last decade [148, 149, 150, 125, 151, 152, 153, 154, 155, 156, 157, 158, 159, 160]. Three main approaches are used: the transmission approach which is used to join a transparent material to a non-transparent material, the focal point approach which is used to join two transparent materials, and the intermediate layer approach which uses a metallic interlayer.

The first laser joining was demonstrated by Wild et al. in 2001 for glass to silicon local bonding with a Nd:YAG laser (1064 nm) [148], a technique which was further explored during the next few years [149, 161, 150, 125, 151, 152]. This technique is based on the difference of absorption of materials. As the glass is transparent to the laser wavelength, the light passes through it and is absorbed by the silicon surface for example. This creates a local high temperature spot. As a result, the glass and the silicon locally melt and create a bond.

Further investigations showed that a precise control of the bonding parameters was required to avoid cracks in the glass and a pyrometer was installed in the laser head in order to control the output power [149, 162]. A helium leak test was realized on cavities sealed with this technique and a leak rate below $1 \cdot 10^{-9}$ mbar l/s was achieved with a typical bonding speeds of 50 mm/min and 500 mm/min. Using this technique, complex micro-fluidic ($< 100 \ \mu$m) structures and different cavities were realized [152].

More recently, another approach was studied in which the focal point of a laser is set to be at the exact interface between two transparent materials [157]. The optical power is therefore more important and as for the previous method, this implies the local melting of the material. Bonding speed in the order of 0.1mm/s were reported[158]. Contrarily to the transmission approach, this method requires a second laser in order to precisely localize the focal point of the laser at the interface of the two wafers [159, 160].

In 2002, Mescheder et al. proposed and demonstrated a laser joining with an aluminum or gold as intermediate layer using a pulsed and cw Nd-YAG laser [153]. The same year, Luo et al. realized a laser joining with an intermediate indium layer with a shadow mask [154]. However, this technique limits the flexibility given by the laser joining. Finally, Tan et al. demonstrated in 2005 a laser joining using gold-tin eutectic alloy [155, 156].

3.1.2.4 Conclusion on bonding technology

The following conclusions can be drawn from the above considerations:

- **Anodic bonding** provides a good hermeticity of the bonding. This solution is therefore well adapted when the alkali metal is present in excess in the cell. However, if the alkali is present in very few quantity due to the filling methods (as it is the case for alkali azide decomposition used by CSEM), this bonding technology becomes challenging for two reasons: First, the bonding principle requires an ion rich glass such as Borofloat$^{®}$ 33 which can be partially reduced by the alkali. Secondly, the process is known to potentially produce undesired gases which might participate to the alkali consumption.

- **Direct bonding** can not be realized with glass.

- **Glass frit bonding** is less sensitive to surface defect as compared to anodic bonding. As this is not a limiting factor for the current application and as the gas production during the bonding process is known to be high, there is no advantage to use this method for the fabrication of atomic vapor cells.

- **Adhesive bonding** is known to be not hermetic.

- **Soft soldering** does not provide any solution for the fabrication of atomic vapor cells. The temperatures are either too high or too close to the operating temperature of the atomic cell.

- **Eutectic bonding** is not realizable due to the high reactivity of Au, Sn or Ge with alkali metals. Moreover $Al - Si$ eutectic bonding is difficult to realize due to the aluminum oxide layer that forms when aluminum deposition is exposed to ambient atmosphere and to the high eutectic temperature. This makes therefore this technique too restrictive from a technological point of view.

- **Transient liquid phase bonding** is not suitable for bonding of atomic vapor cell as all the low-melting-temperature candidate materials are reactive with alkali metals.

- **Thermocompression bonding** Cu-Cu diffusion bonding is potentially an excellent alternative for alkali vapor cell fabrication. Indeed, Cu does not form intermediate compounds with alkali metals and the cross-solubilities are known to be extremely low which makes it an excellent bonding method in presence of alkali metals. Moreover, Cu-Cu bonding allows to bond any materials together which potentially enables the replacement of the classical borosilicate glass by a more alkali resistant materials. It also does not release gases at the bonding interface. Al-Al and Au-Au diffusion bonding are, on the contrary, not suitable for alkali vapor cells. Indeed, for the first, the aluminium oxide is hard to remove in particular in presence of an alkali dispense. For the second, gold is not a appropriate sealant for alkali metal.

- **Microwave local heating** is not compatible with direct alkali metal filling techniques and does not provide any advantage for post-activated techniques.

- **Resistive local heating** would require further studies in order to determine the feasibility of a wafer-level bonding of atomic vapor cells. However, the technique itself is well adapted for the bonding of already filled vapor cells as the cell is not significantly heated during the bonding process.

- **Induction local heating** is also not compatible with direct alkali metal filling techniques and does not provide any advantage for post-activated techniques.

- **Laser joining** provides the advantage that the cell is not significantly heated during the bonding and no supplementary material is used for the bonding.

3.1.3 Dispensing technique

One of the main difficulty when dealing with the filling of MEMS atomic vapor cells is that the alkali metals are highly reactive. It is therefore necessary to find an appropriate process in order to store it and to handle it before and during the process. The filling techniques can be sorted in three main groups: the post-activated processes in which the cell is filled with a miniature device which releases the alkali-metal after the sealing of the cell, the chemical reaction in which a thermal or UV activated reaction is started after the sealing in order to produce the alkali metal, and the direct alkali metal filling, in which the atomic cell is filled prior to its sealing. Each of these techniques have their advantages and disadvantages. The post-activated processes and chemical reactions allow the handling and the bonding of the alkali metal in convenient conditions but can add excess contamination of the cell. In the other hand, direct filling technique require a specific environment in order to avoid the reaction of the alkali metal before the cell sealing. In the following, techniques of the three groups used or proposed for the filling of MEMS atomic cells are discussed.

3.1.3.1 Post-activated processes

Alkali dispenser Alkali dispenser technique was first proposed in the frame of the MAC-TFC project [19]. A piece of a commercially available alkali dispenser commercialized by SAES Getters, Italy, is placed inside a double cavity cell. The dispenser is activated after the sealing by local laser heating. This produces the following reaction which creates cesium and non-reactive side reaction products.

$$2Cs_2CrO_4 + ZrAl_2 \rightarrow 2Cs + Cr_2O_3 + Al_2O_3 + 3ZrO_2 \tag{3.1}$$
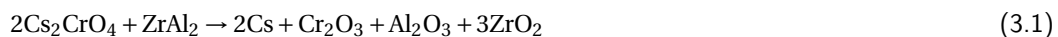
Given the success of this method, dedicated alkali dispenser pills of small size (Cs and natural Rb) were realized by SAES Getters and are now commercially available [20]. This method has nevertheless two main drawbacks: it requires a relatively large cell as a specific dispensing cavity has to be built to contain the pill and the Zr compound of the pill reacts with N_2 and this gas cannot be used as buffer gas [30]. A similar compound was therefore proposed recently under the form of a paste to solve partially the first of these drawbacks [24, 25]. This paste uses the same reaction where Cs_2CrO_4 is replaced by Cs_2MoO_4. Moreover a stabilizer and a binder are added to the mixture. Clock measurement made on MEMS cells filled with this technique showed a long-term frequency drift below $1 \cdot 10^{-10}$/day [24], showing the potential of this filling method.

Wax packet The wax packet method was proposed by Cornell University in 2005 [163]. In this method, Rb is enclosed into wax micropacket produced at wafer scale in a glove box. Vapor cells are then produced with only the desired buffer gas pressure. The cells are sealed at the bottom by only a small SiN layer. The micropacket are then attached to the cells by heating. Finally, a laser removes the SiN layer from the inside of the cell releasing the Rb inside the cell.

Enriched glass electrolysis Enriched glass electrolysis was reported by Gong et al. [67]. A Cs enriched glass is placed in an electric field inside the cell. This makes the Cs diffuse out of the glass. The main drawback of this method is that it only releases a very small amount of alkali metal in the cell.

Alkali metal source tablet   Alkali metal source tablets were reported in [60, 61, 62] for atomic magnetometers. Alkali metal source tablets are porous alumina tablets containing a source material. The alkali metal is released by a chemical reaction, either KN_3 decomposition or reaction of KCl with BaN_6 (see Sec. 3.1.3.1). The tablet is used in order to increase the generation yield and to prevent splashing.

3.1.3.2   Post-activated chemical reaction

The main chemical reactions used for the production of Rb and Cs were analyzed by Hackspill at the beginning of the 20th century [164, 165, 166, 167]. Tab. 3.3 summaries the reactions that are currently used for the production of alkali metal in atomic vapor cells.

Reaction	Temperature	Remark	Reference
$BaN_6 + MCl \rightarrow BaCl + 3N_2 + M$	200°C	Invert reaction observed	[7, 8]
$MN_3 \rightarrow 2M + 3N_2$	450°C	Also UV decomposition	[9]
$2MCl + Ca \rightarrow 2M + CaCl_2$	720°C	Deformation of windows due to reaction temperature	[71]

Table 3.3: Summary of the different chemical reactions used for the production of alkali metals with M=Rb or Cs

Alkali-metal chloride and barium azide reaction   The alkali-metal chloride and barium azide reaction was first proposed by NIST for the filling of cesium atomic vapor cells in 2004 [7]. A solution of CsCl and BaN_6 in H_2O is deposited in the cell cavity and the H_2O is evaporated by baking. The cell is then placed in a UHV chamber and heated which causes the following reaction:

$$BaN_6 + CsCl \rightarrow BaCl + 3N_2 + Cs \tag{3.2}$$

The N_2 is removed from the cell and backfilling of buffer gas is added before the sealing of the cell.
   Cells filled with this technique were measured in a CPT atomic clock and showed a relative frequency drift of $-2 \cdot 10^{-8}$/day. This drift was identified as due to the recombination of impurities, mainly nitrogen and barium recombining to form barium azide [8]. As these impurities are intrinsic to the filling techniques, it makes it incompatible with the fabrication of atomic vapor cells. However a derived method was proposed where the decomposition is realized outside of the atomic cell which showed an improved frequency drift below $5 \cdot 10^{-11}$/day (see Sec. 3.1.3.3).

Alkali-metal azide decomposition   The alkali-metal azide decomposition technique was first proposed by NIST for cesium [9]. In the original method, a film of CsN_3 was deposed inside the cell by thermal evaporation. Further methods in which the alkali metal azide is deposited by pipetting of an aqueous solution were later reported [53]. The azide is then UV decomposed in order to produce pure alkali metal and gaseous nitrogen which gives for rubidium the following reaction:

$$2RbN_3 \rightarrow 2Rb + 3N_2 \tag{3.3}$$

The UV decomposition reaction can be realized either before the cell bonding in order to evacuate the N_2 and add a backfilling of controlled buffer gas or inside the sealed cell in which case the produced N_2 is used as a buffer gas. More details are given on this filling technique in Sec. 3.3.1.

Alkali-metal chloride reduction   The reaction between rubidium chloride and calcium is commonly used for the filling of glass blown cells [168] and was first proposed by in [164, 166]. It consists of

the following reaction:

$$2MCl + Ca \rightarrow 2M + CaCl_2 \tag{3.4}$$

This reaction was tested in MEMS cells for Rb in [71] where Ca is created by CaH_2 decomposition. As the reaction takes place at approximately 720°C, a deformation of the glass widows was observed. Indeed, the reaction temperature is well above the Pyrex® recommended working temperature (500°C) and close to the Pyrex® softening point (821°C). Moreover, in the case of a Pyrex®-Si bonded cell, the thermal expansion creates a non-negligible breaking risk.

Due to its physical properties, Calcium cannot be found in powder form but only in granular form which is not convenient for dispensing in MEMS cells. Magnesium, on the contrary, which has comparable chemical properties can be found in powder form and could replace Ca in the upper reaction.

Reduction of alkali metal chloride has however a few advantages as compared to other techniques. Indeed, since the reaction temperature is well above the atomic vapor cells working temperature, the recombination probability can be supposed to be very low. Moreover the Calcium or Magnesium are known to be non-reactive with the rubidium. Therefore, their residual presence is not a problem from a chemical point of view [169]. The main advantage of this reaction as compared to the previous ones is that no buffer gas is created during the reaction. This overcomes then the limitations in alkali metal quantity given by the other above methods as it is possible to create the alkali metal in excess.

A simple solution can be found to overcome the temperature limitation given by the Pyrex®-silicon bonding: It is known that high power laser can provide a very localized heating above the required 720°C while keeping the rest of the cell in normal thermal conditions [125]. Therefore, the only remaining problem is the amount of residues created by the reaction.

Other chemical reactions   Many other reactions allow the production of alkali metal for example [165]:

$$3Fe + 4MOH \rightarrow Fe_3O_4 + 2H_2 + 4M \tag{3.5}$$
$$2M_2CO_3 + 2Fe \rightarrow Fe_2O_3 + CO + CO_2 + 4M \tag{3.6}$$
$$2MOH + 2Mg \rightarrow 2MgO + H_2 + 2M \tag{3.7}$$
$$2MCl + Pb \rightarrow PbCl_2 + 2M \tag{3.8}$$
$$2MF + Fe \rightarrow FeF_2 + 2M \tag{3.9}$$
$$2MCN + Fe \rightarrow N_2 + Fe + 2C + 2M \tag{3.10}$$
$$SO_4M_2 + Fe \rightarrow SO_4Fe + 2M \tag{3.11}$$
$$AlO_2M + Fe \rightarrow FeO + Al_2O_3 + 2M \tag{3.12}$$
$$2CNOM \rightarrow 2CO + N_2 + 2M \tag{3.13}$$
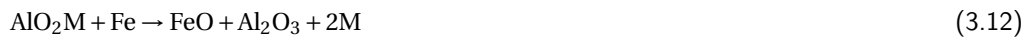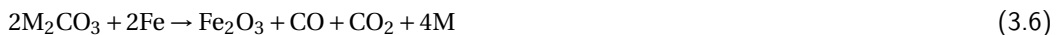
where M=Rb or Cs. However these reactions are not directly suitable for the required application and require further studies. Indeed, the reaction kinetic and equilibrium is not known. Moreover, some of the compounds presented here are either highly toxic or not RoHs compliant.

3.1.3.3   Direct alkali metal filling

Liquid alkali-metal filling   The liquid-alkali metal filling is the easiest filling method from the point of view of its principle. It was used by Liew in 2004 for the filling of the first prototypes of atomic vapor cells. The alkali metal is kept under a glove-box with controlled atmosphere such as dry nitrogen [7] or in a liquid such as dodecane [36] in order to avoid contamination by external gases.

It is then directly dispensed into the cells via pipetting or other methods and kept under controlled conditions until the bonding.

External alkali-metal chloride and Barium azide reaction   The external alkali-metal chloride and barium azide reaction was first proposed by NIST to avoid the contamination of the cell by residual decomposition products. The reaction presented above is simply displaced to the outside of the cell in a glass ampoule. The alkali metal produced is then dispensed inside the cell before the bonding. To avoid contamination of the pure alkali metal, the process is realized under high vacuum.

External alkali dispenser   Alkali dispenser can be used in order to fill the cells with cesium and are commercially available. The first use of an external alkali dispenser was reported by Pétremand in 2012 [48] and used the dispensers commercialized by SAES Getters which were presented in Sec. 3.1.3.1. SAES Getters only provides Cs, natural Rb, Na and K dispensers. However Alvatec provided dispensers based on metallic alloy with ^{87}Rb and natural Rb which were suitable for an external use and have been tested by CSEM [41]. The last were nevertheless discontinued.

3.1.3.4   Conclusion on dispensing techniques

The following conclusions can be drawn for the different filling methods presented above:

- **Direct alkali metal filling** techniques, have the advantage of providing a pure alkali metal inside the cell without other contamination and without limitation on the alkali quantity. This has the advantage of not being limited by the reactions of the alkali metal with impurities inside the cell. However due to the low melting point of Rb and Cs and to their high reactivity, the dispensing must be realized under controlled atmosphere and the wafer must not be heated before a partial sealing to avoid evaporation of the metal. This implies that the bonding equipment must be adapted to this technique or designed for it (*i.e.* dispensing inside the bonder, cooling of the wafer or placement of the bonder inside a glove-box)

- **Alkali dispensers** have been proved to be a good and reliable solution as they also produce an excess of alkali metal. However, the size of the dispenser forces the cell to be realized in a two-cavity design and prohibits the use of N_2 as buffer gas. The unit price of a dispenser makes it moreover a relatively expensive solution. The dispensing paste version is however a excellent alternative as it does not require a separate cavity and showed good clock frequency stability performances.

- **Wax packets** is a technologically complex solution and the influence of the wax impurities inside the cell is not known.

- **Alkali metal source tablets** do not give any interesting advantage as compared to the same reaction made directly inside the cell.

- **Alkali-metal chloride and barium azide reaction** inside the cell showed a recombination and is therefore not suitable for atomic vapor cell.

- **Alkali-metal azide decomposition** is a cost-effective solution and does not require complex technological equipment. The UV activation simplifies also the decomposition process. However, as the alkali metal quantity is directly limited by the buffer gas pressure, the reaction of the alkali metal with impurities inside the cell and the cell wall have to be limited. This technology therefore requires other technological steps in order to increase the cell lifetime.

> - **Alkali-metal chloride reduction** by Calcium or Magnesium is commonly used for the production of alkali metal for conventional glass-blown cell. An invert reaction is very unlikely but the thermal reaction takes place at high temperature and creates a large amount of residues and is hard to realize inside a MEMS cell.
>
> - **Other chemical reactions** are not well known and would therefore require further investigations in order to qualify their eligibility for alkali vapor cell filling.

3.1.4 Getters and anti-diffusion surface coating

3.1.4.1 Getter films

Non Evaporable Getters (NEG) are materials that are deposited in a MEMS cavity in order to trap the gases outgasing from the walls. They are often Zr-based alloys and are commonly used in vacuum encapsulated MEMS to achieve pressures in the order of 10^{-4} mbar [124]. Indeed, NEG can chemisorbe all active gases such as H_2O, CO, CO_2, O_2 and N_2.

When exposed to air, NEG are passivated by a layer of oxide. They are activated inside the cavity after the sealing by heating. During the heating, which can for example be realized by a laser, the oxide diffuses into the bulk of the getter, leaving a free active surface layer.

NEG were tested inside alkali vapor cells in [32]. No direct negative effect of the getter on the cell has been observed. However, no long term study was realized to my knowledge. Moreover, NEG trap N_2 which does not allow Ar/N_2 buffer gas mixture.

3.1.4.2 Anti-diffusion surface coating

The reaction of alkali metal with the atomic cell walls is a critical issue for the fabrication of MEMS atomic cell. Indeed, as the surface - volume ratio is significantly lower than in classical glass blown cells, this reaction is a limiting factor for the cell lifetime as the alkali quantity is limited and is more likely to react with the wall or diffuse through it. To overcome this limitation, a coating of the glass surface with a robust material was proposed by Woetzel et al. in 2013 [54]. Al_2O_3, SiO_2 and TiO_2 were tested with cesium anodically bonded vapor cells. Al_2O_3 coating showed an improvement of a factor of 100 of the cell lifetime. The other coatings did not show any encouraging results. SiO_2 showed no effect on the cell lifetime. TiO_2 was found to be not compatible with the microfabrication process.

For rubidium, Ma et al. measured the quantity of alkali metal absorbed by Pyrex® surface or reacting with it [170]. The conclusion was drawn that a limited quantity of Rb corresponding to 6-7 atomic layers were trapped on the wall surface and called this effect "curing" of the cell.

Several explanations were proposed for the reaction process between the glass and the alkali metals. For cesium, Hirashima et al. proposed in 1969 the reduction of the sodium oxide contained in the glass by cesium [171]. On the contrary, Bouchiat et al. reported in 1999 the reduction of the glass' silicon dioxide [172]. Finally Rothman et al. measured in 1982 the diffusion of K, Rb and Cs in vitreous silica [173].

The reaction rates of cesium with cell walls coated with different materials was studied by Stephens and al. in 1994 [174]. Pyrex® was compared to sapphire (Al_2O_3) and other materials commonly used as anti-relaxation wall coating. The reaction rate of Pyrex® with Cesium was determined by measuring the decay of the Cs fluorescence. Values of 9.6 cm^3/s cm^2 for Pyrex® were found. On the other hand, sapphire reaction rate was measured to be negligible. A more detailed study was reported by Bouchiat et al. by measuring of the surface electric conductivity. Sapphire cells showed a conductivity of five orders of magnitude below the Pyrex cells [172].

3.1.4.3 Conclusion on getters and anti-diffusion surface coating

The following conclusions can be drawn for the getters and anti-diffusion surface coating:

- **Getter films** Getter films are commonly used in vacuum technology to avoid cavity contamination. However in the case of rubidium atomic vapor cells, they are not compatible with Nitrogen as a buffer gas. Moreover, the long term stability of alkali vapor cells with getter was never studied to my knowledge.

- **Anti-diffusion surface coating** The reaction of alkali atoms with glass is a known issue for MEMS atomic vapor cell as it reduces the cell lifetime. This becomes critical when the cell is filled with a small quantity of alkali metal as it is the case when an alkali azide decomposition is realized inside the cell. The reaction of alkali atoms with the cell wall can be explained either by chemical reactions with the cell surface or by diffusion. Anyway, a good improvement of the lifetime can be achieved by deposition of a protection coating. Experiments on wall coating reaction rate showed that Al_2O_3 is the best candidate for this application and can improve the cell lifetime by a factor of 100.

3.2 Cu-Cu thermocompression bonded cells

Based on the review made in section 3.1, two bonding technologies were identified as relevant for the fabrication of alkali vapor cells: anodic bonding is one of these two techniques as it is currently the only established technology. The second technique is copper - copper diffusion bonding (or Cu-Cu thermocompression). This bonding technique is potentially well adapted to the fabrication of MEMS atomic vapor cells for the following reasons: The same materials as for the established anodic bonding can be used (Si and Pyrex®) but it can potentially also be applied to other materials such as sapphire. Indeed, sapphire has the advantage of being transparent, chemically more resistant to alkali metals and of having a low diffusion coefficient. These metals are well adapted as alkali containing material. Moreover,Cu-Cu thermocompression bonding is not expected to produce gases as it is the case with anodic bonding [128, 130]. These two advantages make it an interesting alternative.

Figure 3.2 shows a 3D model of the alkali vapor cell that will be realized with this method. In this representation, a double-cavity cell is shown with a Rb dispensing micro-pill in one of the two cavities. A thin Ta adhesion layer followed by the Cu layer is deposited by sputtering on the silicon wafer and on the glass wafer. In the case of the silicon wafer, a blanket metal deposition is performed whereas a lift-off patterning if the metal layer is done on the glass wafer. The two wafers are then bonded by thermocompression and the wafer is diced into individual vapor cells. The different investigation which were realized in order to reach the final cell are described in this section.
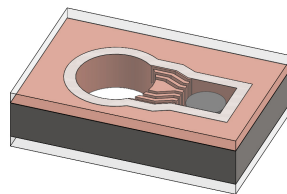

Figure 3.2: 3D model of a two Cu-Cu thermocompression cell filled with a Rb dispensing micro-pill

3.2.1 Substrate structuration

The design of the MEMS atomic vapor cells realized by thermocompression is presented on Fig. 3.3. Two different designs are realized in order to be able to test the two filling methods. A simple cavity is made to be used with rubidium azide (Fig. 3.3(a)) and a double cavity design is made to be used with dispensing micro-pills (Fig. 3.3(b)). The design of the double cavity cells is inspired from [30]. The substrate is a 1000 μm thick wafer. The full cell microfabrication process is described in Sec. 3.2.6. For the simple cavity, a circular opening is created with a diameter of 2 mm (blue and green on Fig. 3.3). On the double cavity design, a square dispensing cavity with 1 mm width is created next to it. The two cavities are connected by four 50 or 100 μm wide micro-channels (see blue layer on Fig. 3.3). These channels are designed such that they do not draw a direct path from the dispensing cavity to the optical cavity in order to avoid impurity transfer from one cavity to the other.

   Our design anticipates the need to compensate for the total thickness variation (TTV) of the wafer and to increase the bonding pressure. Indeed, contrarily to anodic bonding, Cu-Cu thermocompression is much more sensitive to thickness variation as the electrostatic force which pulls the two wafer together in the case of anodic bonding does not exist. Moreover, a bonding pressure superior to anodic bonding is required. Therefore, our design includes so-called TTV-release structures in order to allow a contact between the two wafers only at the desired locations. This TTV-release structure is 1.5 μm deep etched by DRIE it is designed to be etched on the places where no Cu contact is needed (see purple layer on Fig. 3.3).

   The cell cavity is surrounded by a 300 μm wide Cu track patterned on the 300 μm thick borosilicate glass window wafer. Another Cu track is located at the border of the cell for mechanical stability during dicing.

(a) Simple cavity cell (4 mm × 4 mm)   (b) Double cavity cell (4 mm × 6 mm)
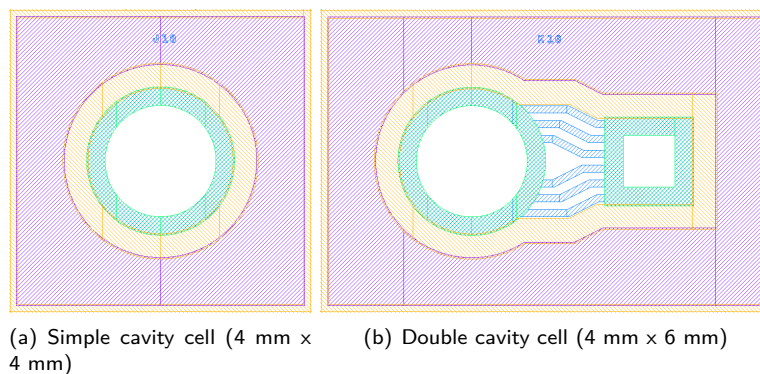
Figure 3.3: Thermocompression cell layers design - green: cavity (bottom), blue: cavity and channels DRIE (top), purple: TTV release (top & bottom), orange: Cu structuration (top & bottom)

3.2.2 Copper metalization

For Cu-Cu thermocompression bonding, in contrast to anodic bonding, the window wafer needs to be processed prior to the bonding and a copper layer needs to be deposited on both the cell cavity wafer and the window wafer. This copper layer requires to be patterned on the window wafer in order to have an optical access to the cavities for atomic absorption measurement and for the dispensing micro-pill activation.

   The patterning could in principle be done either by etching of the Cu and the adhesion layer after deposition or by lift-off. Based on the etch rate of Cu, Ta, Cr and Ti [115], an elegant solution would be to use CR-7 etchant to etch the Cu layer and the Cr layer: the etch rates being respectively 280 nm/min and 170 nm/min.

As an alternative solution, in case the etching approach does not give satisfactory results, the lift-off approach is considered. Nevertheless, this approach is not the first choice due to a higher complexity and a potential decreased pattern quality. Test are nevertheless realized with Ta as adhesion layer in order to have an alternative approach to Cr and as Ta was shown to be a valid adhesion layer for Cu-Cu thermocompression in most of the related literature (see [175, 176, 177, 178, 179, 180, 181, 182, 127]).

Preliminary tests were realized in order to assess the Cr and Cu etching process. 50 nm of Cr and 500 nm of Cu were deposited on a 200 μm Borofloat® 33 wafer. A photolithography was realized with AZ1518 positive resist and developed. The wafer was then put in a CR-7 solution for approximately 2 minutes until the glass windows were totally transparent at the opening locations (spectroscopic cavity and micro-pill cavity). The result is presented in Fig. 3.4. The Cu layer is practically totally under-etched at the time the Cr etching is completed. Indeed, the remaining Cu layer can only be seen on small portion of the structure. This shows that the use of the etch technique is not appropriate for the window wafer structuration. Therefore the lift-off technique will be used.
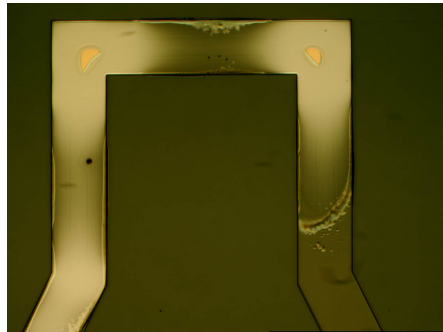
Figure 3.4: Cr Cu etch test: Cu layer nearly fully under-etched at the time Cr etching is completed

The lift-off process consists in using a sacrificial material to create a desired structure. In the present case, the Cu structuration is realized as follow: First a bi-layer resists structure is created by photolithography: A 600 nm LOR3B layer is coated under a S1813® photoresist layer on the 300 μm thick Borosilicate wafer. The LOR3B layer is used as undercut material in order to facilitate the lift-off process. The resist is developed in AZ® 400 buffered KOH based developer. The Cu layer and Cr adhesion layer are then sputtered. The lift-off is finally realized in NMP and the wafer is cleaned in Isopropanol and DI water.

3.2.3 Thermocompression bonding

The bonding condition is the most critical aspect in order to ensure mechanically reliable and hermetical cells. A detailed literature review based on [175, 176, 177, 178, 179, 180, 181, 182, 127] showed that the following parameters have to be taken into account:

- Bonding temperature

- Bonding time

- Bonding force

- Cu oxide removal

- Annealing temperature

- Annealing time

Based on this literature review, the following values were extracted: the oxidation layer above the Cu tracks must be removed prior to the bonding. This can be done by HCl cleaning [175, 177, 181] or by forming gas annealing prior to the bonding [178, 180]. As the first method cannot be realized due to the Rb dispenser (dispensing micro-pill or RbN$_3$), the last (forming gas) was chosen. The bonding force must be such that the pressure is in the order of 4000 mbar on the bonding structure [175, 176, 177, 179, 181]. The bonding temperature and time as well as the annealing temperature and time can be either 30 minutes bonding at 350°C followed by 60 min annealing at 350°C or 30 minutes bonding at 400°C followed by 30 min annealing at 400°C, in order to achieve an excellent bonding quality [175, 176, 177, 179, 178, 181]. The two options are compared.

The wafer bonding proceeds as follow: The two wafers are placed in a Süss SB6e wafer bonder. They are separated from each other with 200 μm spacers. The bonding chamber is purged with forming gas and heated to 350°C. Once the temperature is reached, the forming gas is purged again and left for annealing for 30 min (two steps of 15 min with an intermediate purge). The chamber is then pumped down. Depending on what is required in the cell, buffer gas is backfilled in the chamber at the desired pressure or the chamber is left under vacuum. The wafer spacers are then pulled out and the bonding pressure is applied. The bonding force was fixed at 14 kN which is the maximum of the wafer bonder. The wafer is left under pressure for 30 min, then the pressure is removed and the wafer are left for annealing under vacuum for 60 min. Finally, the temperature is ramped down and the chamber is purged with N$_2$ at atmospheric pressure.

3.2.4   Optimization of the bonding process

Prior to realizing a full atomic vapor cell, bonding tests were realized in order to optimize the bonding parameters. A simplified process was developed (see Fig. 3.5). The TTV release structure (see Sec. 3.2.1) is DRIE etched in a 500 μm thick wafer.

Seven runs were realized with different bonding parameters and adhesion layer (see Tab. 3.4). The test runs were characterized by the two methods proposed in [127]: pull tests and scanning electron microscopy (SEM). The results are presented below.
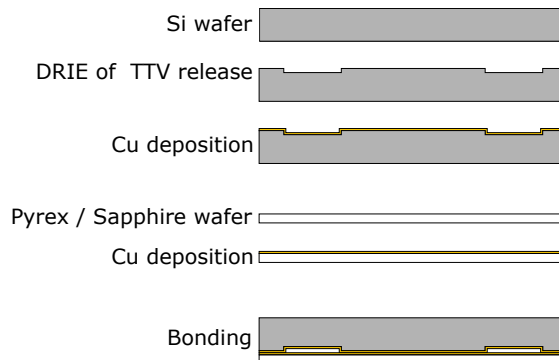
Figure 3.5: Simplified thermocompression bonding test process

3.2.4.1   Pull test

The bonded wafers of the seven runs were diced into individual 4 mm by 4 mm pieces. They were then glued to a sample holder and their pull test resistance was tested with a traction device. The results are presented in Tab. 3.4. A literature value of 70 MPa [127] is expected. However, the maximal value that can be obtained on the diced pieces with the available traction device is 35 MPa. All the tests were realized with 6000 N bonding force.

In runs 1 and 2, no adhesion layer was used and the Cu was directly deposited on the Si and Borofloat® 33 surface. After bonding, a pull strength in the order of 10 MPa was observed. The breaking point was always observed between the Cu layer and the Borofloat® 33 surface. An example of run 2 showing delamination of the Cu from the Borofloat® 33 glass is presented in Fig. 3.6. This justifies therefore the use of an adhesion layer. This adhesion layer will be used for both the Si and the Borofloat® 33 surface.

In run 3, no forming gas was used and the wafers were heated at the bonding temperature in N_2 atmosphere prior to the bonding step in order to give the same thermal budget to the sample. At the end of the process, no bonding was observed and the wafer surfaces were visibly oxidized. This Cu oxidation can be attributed to residual O_2 and H_2O in the bonder and in the used N_2 purge atmosphere. This therefore justifies the use of forming gas in order to reduce the oxide layer on the wafers prior to the bonding.

In runs 4 and 5, a Cr adhesion layer was used. A bonding was observed between the wafers. However, the observed pull strength is far below the expected value. Moreover the 400°C sample showed an even lower value than the 350°C sample. In order to understand this behavior, SEM analysis were realized. The results are summarized in Sec. 3.2.4.2.

In run 6 and 7, a Ta adhesion layer was used. The bonding strength are above the measurement capability of the traction device showing that the bonding strength is better than for the other runs and potentially close to the target value of 70 MPa.

In run 8, the optimal parameters found in run 6 were used. The test was nevertheless realized without the TTV release structures in order to confirm their necessity. As result, a bad bonding of the wafer was observed. Indeed, only a small region at the center of the wafer was bonded which confirms the necessity of the TTV release structures in the present case. The reason of this necessity can be attributed to two factors. First, the TTV structure allow to circumvent the TTV variation of the wafer and allows a good contact between the two wafers. Secondly, with the maximum force of 14 kN applied by the wafer bonder used here, the TTV structures distribute the force on only a small part of the wafer, concentrating the pressure.

Figure 3.6: Example of a bonding sample of run 2 after the pull test: The Cu layer did not adhere to the glass substrate

3.2.4.2 SEM surface analysis

Scanning Electron Microscope (SEM) analysis was performed on the surface of broken samples of run 5 in order to understand the poor bonding strength. Figure 3.7 shows a mixture of Cr and Cu giving evidence of diffusion that has occurred between the two layers at 400°C. This result was confirmed by EDX anaylsis. It can therefore be concluded that a diffusion between the two layers occurs. This

Run	Metalization	Temperature	Forming gas	Bonding time	Annealing	Pull test	Remark
1	500 nm Cu	350°C	30 min	30 min	60 min	11 MPa	
2	500 nm Cu	400°C	30 min	30 min	30 min	10 MPa	
3	500 nm Cu	350°C	No	30 min	60 min	No bonding	
4	50 nm Cr, 500 nm Cu	350°C	30 min	30 min	60 min	21 MPa	
5	50 nm Cr, 500 nm Cu	400°C	30 min	30 min	30 min	2.7 MPa	
6	50 nm Ta, 500 nm Cu	350°C	30 min	30 min	60 min	>35 MPa	
7	50 nm Ta, 500 nm Cu	400°C	30 min	30 min	30 min	>35 MPa	
8	50 nm Ta, 500 nm Cu	350°C	30 min	30 min	30 min	No bonding	Without TTV release structure

Table 3.4: Bonding test runs and pull test results

diffusion is more active at high temperature explaining the lower bond strength of the 400°C sample as compared to the 350°C sample.
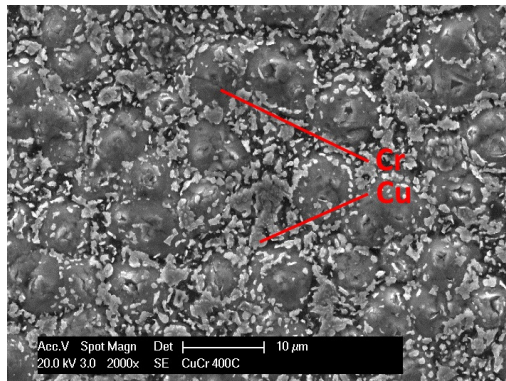
Figure 3.7: SEM analysis of a test wafer after bonding tentative at 400°C (Si wafer, 50 nm Cr, 500 nm Cu sputter deposition). Here is shown the surface of a bonded sample after pull test (Si side). Cr can be seen over the Cu layer showing the diffusion of Cr into the Cu layer.

3.2.4.3 FIB cross-section analysis

In order to assess and to compare the bond quality of the two best wafer bonding samples (runs 6 and 7), cross-section analysis of the bonded layers were realized. Samples were prepared by etching and focused ion beam (FIB) milling as follow:

- Diced samples (see figure 3.5) were placed in a KOH solution in order to remove silicon and to access the Cu bonded layer. As a side effect, the Ta adhesion layer on the silicon side was also etched by KOH

- A carbon coating was deposited on Cu surface in order to protect the surface for FIB milling

- Cross-section of the bonded layers was prepared by FIB milling

- SEM analysis was performed on the cross-section

Figure 3.8 shows an example of the bonded layer typically observed on the 6th and 7th sample. The grain structure can be easily observed confirming a good bond quality [127]. No voids were observed between the two initial layers. Moreover, crystallographic twins were observed through the final layer (only on the 3rd sample, see Fig. 3.8) showing the formation of a uniform copper structure.

3.2.5 Sapphire cells

3.2.5.1 Sapphire to silicon bonding

In order to assess the potential of Cu-Cu thermocompression bonding for sapphire to silicon bonding, a test was realized with the simplified bonding process presented in 3.2.4 between a 500 μm sapphire wafer and 500 μm structured silicon wafer. The same bonding parameters as for sample 7 were used. The results of this test can be seen on figure 3.9. Despite the large bonded zone, the silicon substrate broke due to the elevated mismatch between the coefficient of thermal expansion (CTE) of silicon and sapphire (respectively 2.6 ppm/°C and 8-9 ppm/°C, depending on the crystallographic orientation). It can therefore be concluded that thermocompression bonding of silicon to sapphire is not well adapted due to its relatively high bonding temperature and due to relative mismatch of CTE.

Crystallographic
twin

Carbon coating

Cu-Cu bonded layer

Ta adhesion layer
Glass substrate

200 nm | EHT = 2.00 kV | WD = 5.1 mm | FIB Imaging = SEM
Mag = 38.06 KX | Signal A = InLens | Stage at T = 54.0°

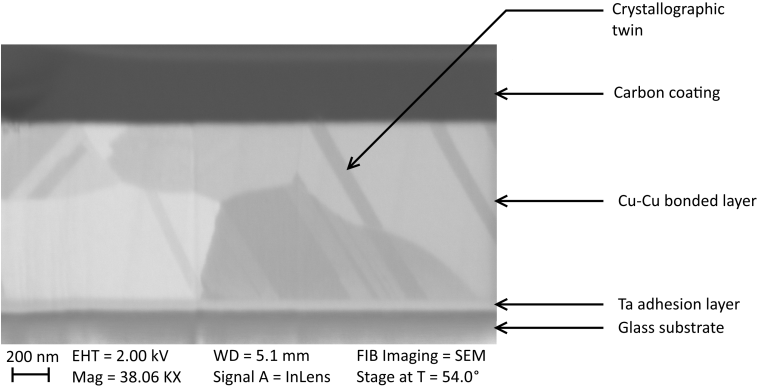Figure 3.8: SEM cross-section measurement made on a sample bonded at 400°C

Figure 3.9: Bonding test of silicon on sapphire: silicon substrate broken due to the too high CTE difference

3.2.5.2 Sapphire machining

From the preliminary tests realized on sapphire, we concluded that sapphire could not be bonded to silicon by thermocompression bonding. We therefore propose to replace the silicon substrate by a sapphire substrate in order to create full sapphire cells and to match the CTE of the two bonded layers. Moreover, preliminary test showed that the TTV of the two bonded wafer must be maintained as low as possible in order to achieve the bonding.

Sapphire being a hard material and being resistant to most chemicals, only laser machining can be used to produce patterns at the scale of the cells. First machining test were realized on a 500 μm wafers in order to verify if the structures (double cavities, micro-channels and TTV release structures) could be machined. Two runs were realized with a picosecond laser machining setup. In the first run 2μm TTV release micro-structures were etched, followed by 100 μm wide, 100 μm deep micro-channels and through-hole cavities. Unfortunately, the wafer broke at the first step and showed significant stress. The second test was realized without the TTV release structure. In that case, the wafer machining showed good result and $\approx$200 cells could be machined on the wafer (see Fig. 3.10).
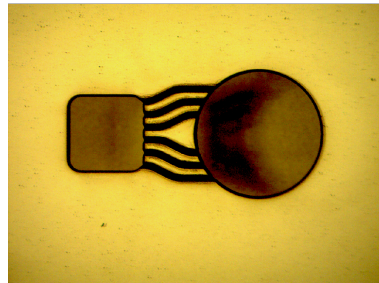
Figure 3.10: Through-hole cavities and 100 μm deep, 100 μm wide micro-channels machined in a 500 μm thick sapphire wafer

3.2.5.3 Sapphire to sapphire bonding

A second test was realized with two sapphire wafers. The supplier specifications were a TTV below 15 μm. After bonding and dicing, it was observed that the two copper layers did not adhere on the full wafer surface but only on a small region at the center. This was attributed to the important total thickness variation (TTV) of the sapphire wafers used and to the fact that, as sapphire is a much harder material, the bonding force required to put into contact the two wafers is potentially higher than for glass to silicon. Sapphire wafers with a lower TTV and a thicker Cu layer could potentially be bonded. That approach was nevertheless not tested in the frame of the present work. Indeed, the cost aspect of the fabrication of such high flatness wafers was out of the scope of the present work.

3.2.6 Complete cell realization

Based on the previous observations, the final Cu-Cu thermocompression atomic vapor cells fabrication process could be determined. The bonding parameters of run 6 were used. The full cell fabrication process is described in Fig. 3.11. It is as follows:

First the TTV release structures are etched on both sides of a 1000μm Si wafer by photolithography and DRIE. A SiO$_2$ thermal oxide is then produced at the surface of the silicon wafer. It will be used as a second mask layer for the silicon etching. The cell cavity design is then transferred to the bottom of the substrate by positive photoresist lithography. The oxide is then removed where necessary by RIE etching. The cell cavities are then etched through the half of the wafer by DRIE. The bottom etching being finished, the photoresist is stripped and a Parylene layer is deposited on the top of

the so-etched cavities (bottom of the wafer). That layer is used to maintain the leak tightness of the wafer during the DRIE and therefore allow its vacuum holding and cooling inside the etching machine. Moreover, the Parylene allow to maintain the Si sacrificial pieces until its stripping. As for the bottom, a photolithography is realized followed by the RIE etching of the SiO_2 layer and the DRIE etching of the top part of the cavities and of the micro-channels. After stripping of the photoresist and of the Parylene, the remaining Si oxide layer is removed by BHF etching and the Ta/Cu layers are deposited by sputtering.

The top window wafer is then prepared. A 300 μm Borofloat$^®$ 33 wafer is used. The 20 nm Al_2O_3 anti-diffusion barrier is deposited by MVD. A positive photolithography of the Cu sealing rings is realized. The Ta and Cu layers are then deposited. Finally, the lift-off stripping of the photoresist allow to create the structure.

The Cell bonding process is as follows: A first window wafer is bonded by thermocompression to the bottom of the structured Si wafer with the parameters of run 6 without the annealing step. The cells dispensing cavities are then filled with Rb dispensing micro-pills and the cell is closed by a second Cu-Cu thermocompression bonding under controlled buffer gas atmosphere. The bonding process is finished by the annealing step (see Fig.3.12) and dicing. An example is presented on Fig. 3.13.

Si substrate

TTV release structures
photolithography (bottom)

TTV release structures DRIE (bottom)

Stripping photoresist

TTV release structures
photolithography (top)

TTV release structures DRIE (top)

Stripping photoresist

Si oxidation

Cavities structures
photolithography (bottom)

RIE etchinig of Si oxide (bottom)

DRIE etching of bottom cavities

Stripping photoresist

Parylène CVD deposition (bottom)

Cavities and micro-channel
structures photolithography (top)

RIE etching of Si oxide (top)

DRIE of top cavities and micro-channels

Stripping of photoresists

BHF stripping Si oxide

Ta/Cu sputtering

Borosilicate substrate (2x)

Al₂O₃ MVD deposition

Photolithography

Ta/Cu sputtering

Lift-off stripping of photoresist

Cu-Cu thermocompression bonding
of bottom window

Micro-pill deposition and Cu-Cu
thermocompression bonding of top window

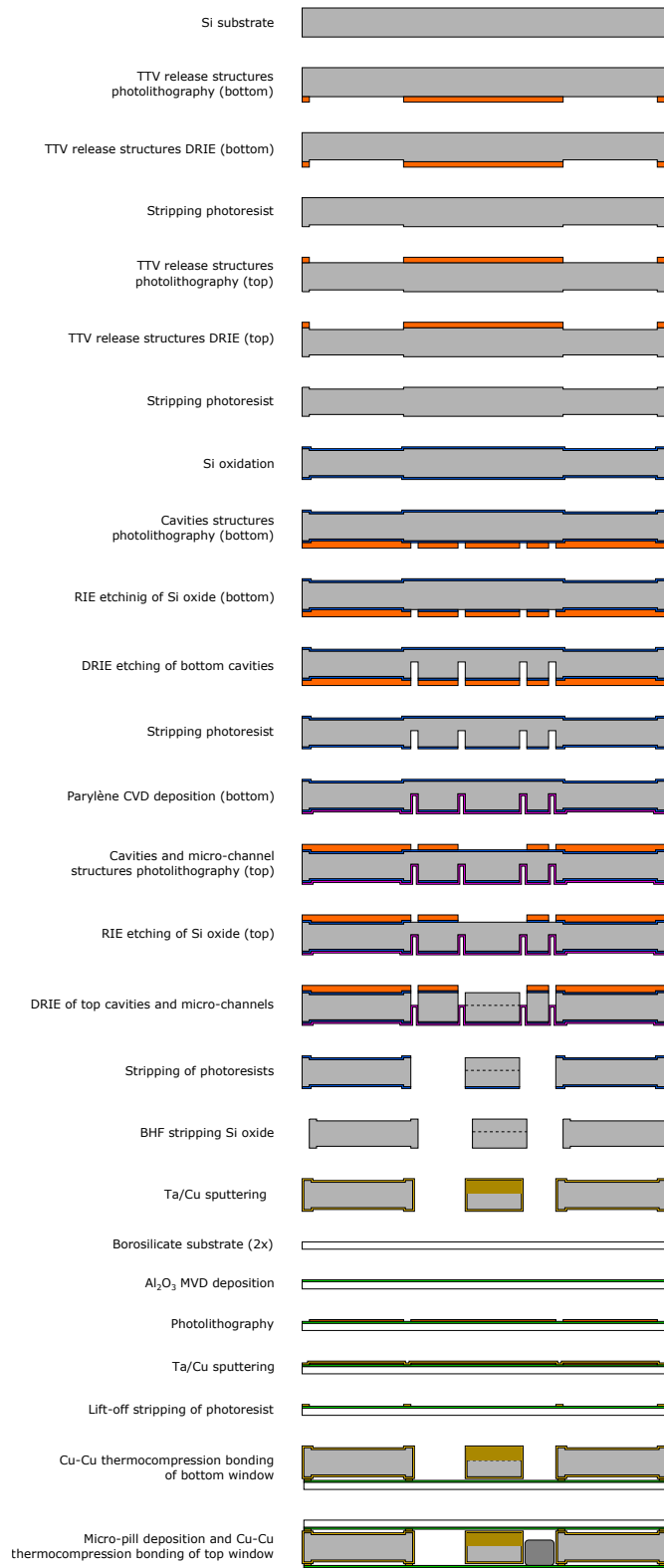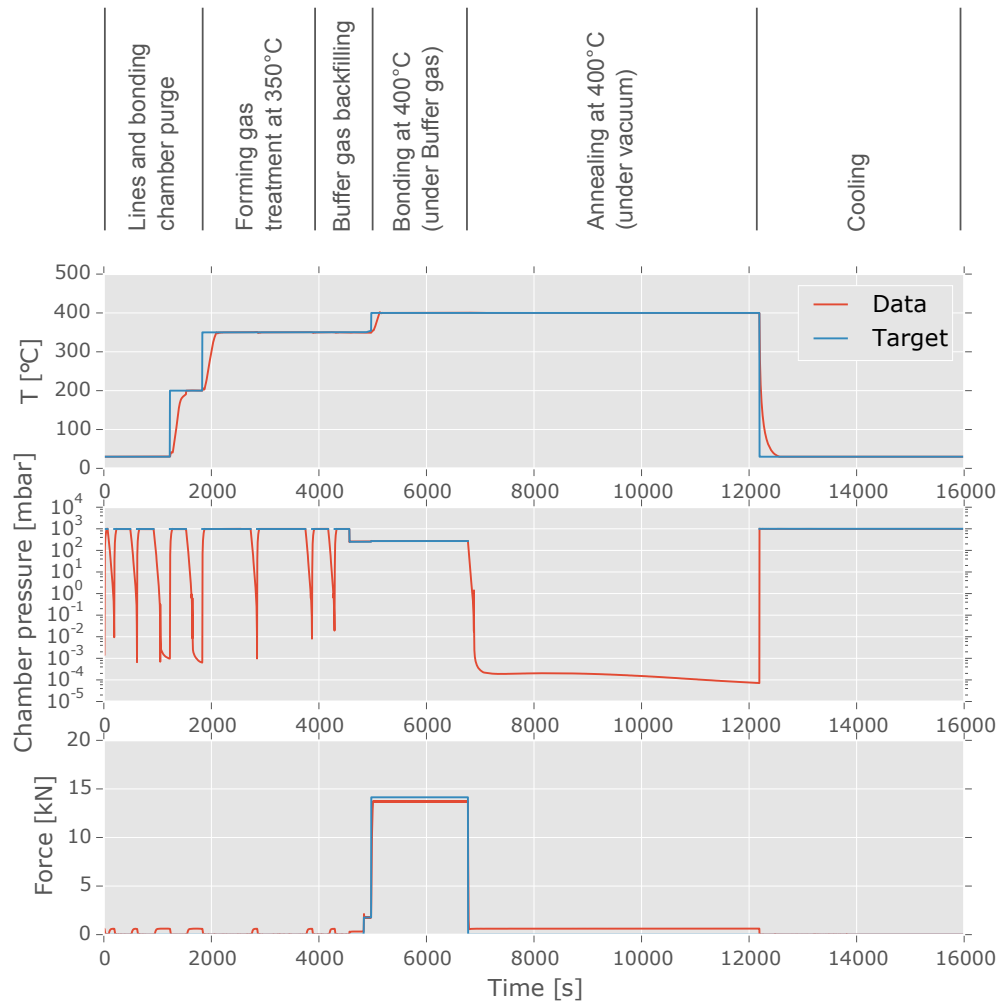Figure 3.11: Full microfabrication process of the Cu-Cu thermocompression cells

Figure 3.12: Monitoring of the bonding parameters during the second bonding step (sealing under Buffer gas atmosphere) of a Cu-Cu thermocompression wafer. See Sec. 3.2.3 for an explanation of the different steps.
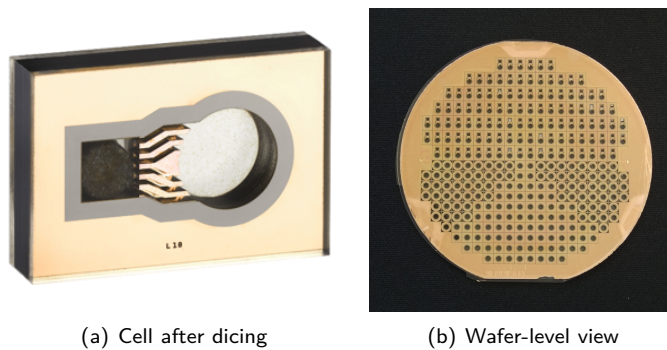

(a) Cell after dicing

(b) Wafer-level view

Figure 3.13: Picture of the first realization of a thermocompression atomic vapor cell

3.3 Alkali dispensing

Based on the review made in section 3.1, two filling technique were identified as interesting approaches to the existing techniques for Rb dispensing: In-situ alkali metal azide UV-decomposition and alkali metal dispensing micro-pills. Indeed, these two techniques are currently the only ones that are applicable on a wafer level and with conventional clean-room equipment. Both were already tested and showed good results, and moreover RbN_3 decomposition has been investigated for years at CSEM. Dispensing micro-pills, on the other hand and to the best of my knowledge, were only tested for Cs and will be investigated in more details in the following.

3.3.1 Alkali azide decomposition

Alkali azide decomposition (Eq. 3.3) has several advantages for low-cost wafer-level filling of atomic vapor cells. Indeed, as a very limited amount of Rb is dispensed in each cell, the use of isotropically selected rubidium (*i.e.* pure ^{87}Rb or ^{85}Rb) becomes interesting on an economical point of view. Here, RbN_3 is dispensed in aqueous form. In solid form RbN_3 is a white powder which dissolves well into pure water. Here, a concentration of ≈ 0.75 mol/l is used. The aqueous solution is dispensed by a picoliter dispenser. Drops with a diameter of 85 μm (≈ 300 pl) are deposited inside the cavity. The number of drops is adjusted in order to reach the desired N_2 pressure. 20 to 60 drops are typically dispensed which corresponds to the creation of 50 to 150 mbar of N_2 at room temperature and to the creation of 0.4 to 1.1 μg of metallic Rb by the decomposition reaction. After drying of the drops in ambient atmosphere, the cells are sealed under Ar buffer gas atmosphere and diced. UV-C light tubes emitting at a peak wavelength of 254 nm are used to irradiate the cells. The irradiation time and conditions are set such that a decomposition rate close to 100% is reached.

3.3.2 Dispensing micro-pill

Dispensing micro-pills have the main advantage to remain inert at the temperature of bonding ensuring an optimal and hermetic sealing. Once the cells are closed, a high power laser diode is used to locally heat the dispenser above 600°C, temperature at which the pill starts and releases pure Rb vapor. The advantage of such pills is that unlike RbN_3, the Rb quantity is not linked with buffer gas pressure. We used Rb/AMAX/Pill/1-0.6 dispensing micro-pills from SAES Getters. It is composed of a zirconium-aluminum alloy powder mixed to chromium-free natural rubidium precursor.

These pills nevertheless present several drawbacks: first the size of the pill is relatively large and, as a double cavity design is required, the overall cell dimension is bigger. Secondly, the insertion in the cell cavity is a slow process hardly compatible with wafer-level fabrication. Finally, it requires a specific buffer gas mixture as the conventional Ar-N_2 cannot be used (see below).

3.3.2.1 Buffer gas mixture

Ar-N_2 buffer gas mixture is commonly used in Rb vapor cells for atomic clocks. Unfortunately, it was shown that N_2 is not compatible with the dispensing micro-pill [183]. For Cs, a Ne-He mixture was proposed as an alternative. The sign of the temperature dependency of buffer gas shifts is however not the same for Cs an Rb and this mixture cannot be used as the two gases have a positive dependency to temperature at the operating temperature for Rb (see Tab. 3.5 [94]). Based on the coefficients of table 3.5, two buffer gas mixtures could be used: Ar-Ne and Ar-He, with respectively a ratio of 27%Ar-73%Ne and 71%Ar-29%He. We chose Ar-Ne mixture because it has two main advantages over the other mixture: first the two gases ratio is easier to balance as the Ne coefficient is lower that the He coefficient. Indeed, an error of 1% in the gas mixture implies a shift of $\approx 5\%$ for Ar-Ne and $\approx 10\%$ for Ar-He. Moreover, He being a lighter gas than Ne, it is more subject to permeation

into the cell glass wall as discussed in [33]. Ar-Ne is therefore a better candidate for good long term frequency stability.

Gas	Fractional frequency dependance to temperature [$10^{-1} \cdot$ Torr$^{-1} \cdot$ °C^{-1}]
He	11.6
Ne	1.79
Ar	-4.8

Table 3.5: Dependency of the buffer gas frequency shift to temperature for Rb at 95°C

It can be noted that the gases proposed here are only noble gases and that the quenching effect [77] is not as efficient for noble gases as for N_2. However, the results of [183] indicate that in comparable case, the excited state relaxation are sufficient to achieve good contrasts in the CPT resonance, even without the presence of N_2. Therefore, the target value of the buffer gas mixture that will be used for microfabrication was chosen to be fixed to 27% Ar and 73% Ne. Based on the coefficients of [94], this corresponds to an inversion temperature of 95.2°C.

3.3.2.2 Laser activation

The micro-pill laser activation setup consists in the focalization of a powerful laser onto the pill in order to heat it up to a temperature above 600°C [24]. The scheme of the setup is shown in Fig. 3.14. A 940 nm Lumentum 10 W fibered laser diode is used. The laser beam is focalized on the top of the cell. The power and the duration need to be adjusted in order to release a sufficient amount of Rb without having it into excess or breaking the glass window due to a too high intensity (See Fig. 3.15). A value of 4 W for 10 s was found give reasonably good results and was used for the cells used in the following.
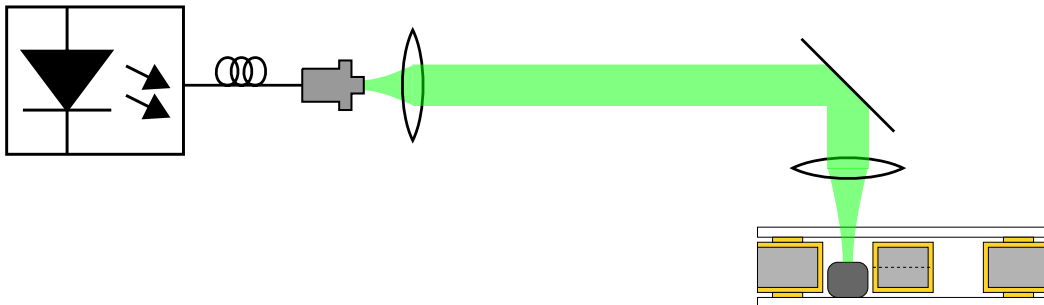

Figure 3.14: Schematic view of the micro-pill activation setup

Figure 3.15: Example of a cell with excess Rb due to a too high laser intensity and too long activation time (6W for 20s)

3.4   Anti-diffusion surface coating

Al_2O_3 surface coating was reviewed in Section 3.1.4.2. It was proposed by Woetzel et al. [54] as solution to improve Alkali-azide filed MEMS cells lifetime. In most of the cells tested here, a 20 nm layer of Al_2O_3 is deposited on top of the windows of the cavity. However, two different approaches are taken for the two bonding processes described here (see Fig. 3.11 and 3.19). In the case of anodic bonding, the first borosilicate window is bonded to the silicon structured wafer prior to the deposition of Al_2O_3. The diffusion barrier is therefore deposited on the surface of both of the second borosilicate wafer and the Si. This nevertheless did not prevent bonding as shown by Woetzel et al. In the case of Cu-Cu thermocompression, as the bonding principle is different, such an approach could not be used. The Al_2O_3 layer is therefore deposited directly on the two borosilicate wafers prior to the Cu layer lift-off deposition. In that case, no Al_2O_3 was deposited on the Si surface. Unlike Woetzel et al., we used molecular vapor deposition (MVD) instead of atomic layer deposition (ALD). It is known to give denser, smoother and more stable films as compared to other standard liquid or vapor deposited coatings [184] .

3.5   Gold micro-discs

One of the major limiting factor for CSAC and cell clocks mid and long term frequency stability is known to be the variation of laser intensity inside the cell. In most of the case, this variation can be attributed to the condensation or evaporation of alkali droplets within the interrogation laser light-path at the input window of the cell. The droplets thereby decrease the laser intensity and affect the measured frequency through the light shift effect (see Sec. 2.5.3). In glass blown cells, an elegant solution was found for cm-size glass blown cells by creating a cold spot at the cell tail. This cold spot serves as a preferential condensation spot which avoids the displacement of alkali metals within the laser light-path. That solution is nevertheless difficult to implement for MEMS cells due to the size constraint. As an alternative, CSEM patent pending[2] gold micro-discs were proposed. They consist in the structuration of a small surface of gold inside the cell volume which serves to condensate the Rb on a desired location.

3.5.1   Working principle

The Au-Rb system (as well as Au and Cs) are known to form intermetallic compounds. The phase diagram is given in Fig. 3.16. The enthalpy of mixing and excess Gibbs energy of the liquid alloys are expected to be large, negative, and "V-shaped", with a sharp minimum at 50 atomic % Rb. Therefore if Rb is present in a sufficient excess as compared to Au in a cell and if the effects of the drop size are neglected, the Rb vapor is expected to preferentially condensate on the Au gold surface and at the equilibrium to create an AuRb - Rb liquid mixture. The kinetic of the process is however harder to determine theoretically as it is driven by the evaporation - condensation mechanisms and needs to be explored experimentally.

Moreover, due to the Raoult's law, the Rb partial pressure is expected to be reduced by a ratio corresponding to the ratio of Au in the Au-Rb mixture. The effect of that reduction is however not an issue as the pressure decrease can be compensated by an increasing of the temperature. For example, for a 2% Au-Rb mixture, the Rb partial pressure change can be compensated by an increase of the cell temperature of $\approx 1°C$ (see Eq. 2.49).
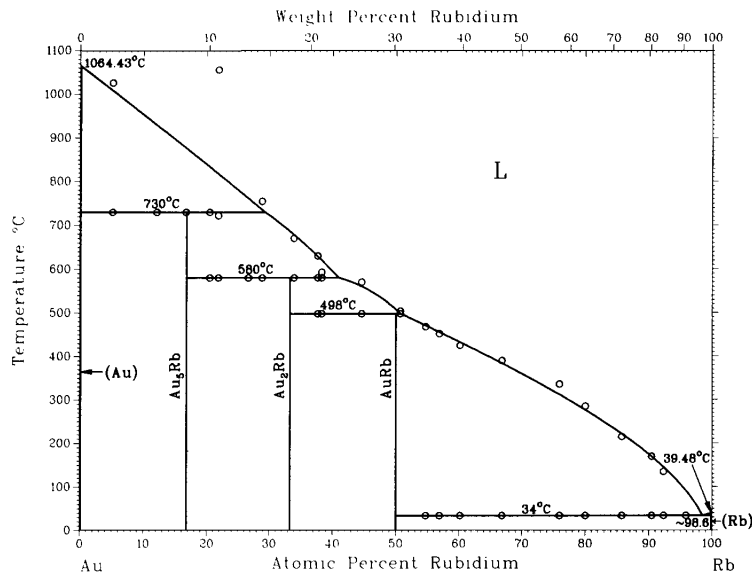
---

[2]European patent application EP 3 244 269 A1

Figure 3.16: Au-Rb phase diagram [119] - **Copyright ©1986, American Society for Metals. Reprint by permission of Springer International Publishing.**

3.5.2   Gold surface structuration

The gold patterns are realized by lift-off. A 50 nm Au layer is deposited over a 10 nm Ti adhesion layer by e-beam evaporation. For the simple cavity design which is dedicated to RbN_3 filling, as the total amount of available Rb is limited (see Section 5.3), the surface was designed such that the total Au amount corresponds, at the maximum, to the conversion of 3% of $1\mu g$ Rb into AuRb. For the two cavities design, as the available Rb amount is much more important, a total surface approximately 3 times larger was designed. The cell design is presented in Fig. 3.17. Au placed in the measurement cavity is designed in 8 micro-discs of a diameter of 100 μm placed an the border of the cavity in order to avoid the clock interrogation laser light-path. In the two cavities design, an additional Au surface is placed in the dispensing cavity in order to capture the liquid Rb in that cavity before it goes in the measurement cavity.

(a) Double cavity cell (4 mm x 6 mm)
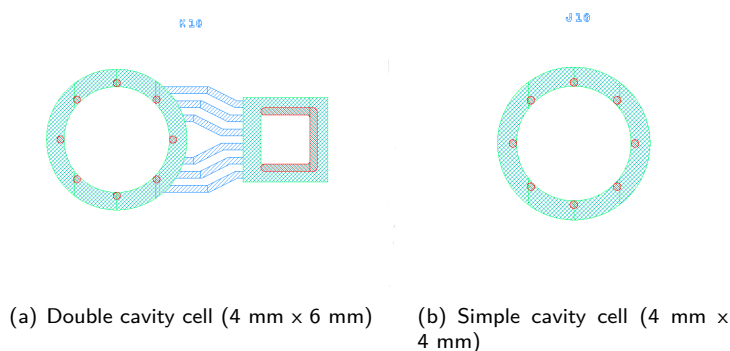
(b) Simple cavity cell (4 mm x 4 mm)

Figure 3.17: Anodic bonded cell with Au micro-discs layers design - green: cavity (bottom), blue: cavity and channels DRIE (top), red: Au structuration (bottom)

3.5.3 Cell fabrication

The full anodic bonding fabrication process with Au micro-disc is described in Fig. 3.19. The silicon etching process consists in the same technological steps as for the Cu-Cu thermocompression cells except that the TTV release structures are not etched. The top window wafer is prepared as follows: A 300 μm Borofloat® 33 wafer is used. The 20 nm Al_2O_3 anti-diffusion barrier is deposited by MVD. A positive photolithography of the Au discs is realized. The 50 nm Au layer is then deposited over a 10 nm Ti adhesion layer by evaporation. Finally, the lift-off stripping of the photoresist allow to create the structure.

The Cell bonding process is as follows (see Fig. 3.18): first a 300 μm Borofloat® 33 wafer is bonded to the bottom of the structured Si wafer. A 20 nm Al_2O_3 anti-diffusion barrier is deposited by MVD on top of the full structure. Finally, the cells dispensing cavities are filled with Rb dispensing micro-pills and the cell is closed by a second anodic bonding under controlled buffer gas atmosphere.
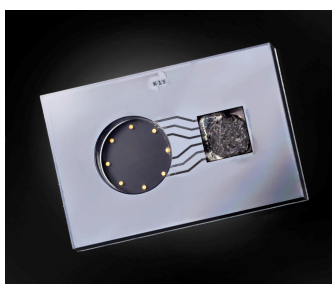

Figure 3.18: Microfabricated cell with Au microdiscs

3.5.4 Microscope imaging

Preliminary investigations on the Au micro-discs were realized by means of optical observations. A cell was irradiated according to Sec. 3.3.2.2. Fig. 3.20 shows three images of the measurement cavity of the cell taken from the bottom. The left image is taken right after the irradiation. The Au micro-discs can be seen but no droplets are present inside the cavity. The center image shows the same cell after 4h heating on a hotplate in ambient temperature. The cell was placed on the side on the base plate such that the dispensing cavity is the hot spot of the cell. In that case, a large amount of rubidium condensed on the measurement cavity at the center of the window. The right image shows the same cavity after a 1h treatment at 180°C in an oven. On that last image, the Rb completely condenses on the Au micro-discs.

These behaviors can be explained as follows: At first when the micro-pill is activated, Rb is created inside the dispensing cavity. After the hot plate treatment, the Rb migrates inside the measurement chamber and condenses onto the cell windows. As silicon is a good thermal conductor, the center of the window is likely the coldest spot inside the cell. The thermal gradients are probably such that the condensation of Rb on the Au discs are energetically less favorable. After the uniform oven treatment however, the temperature of the silicon and glass being uniform, the most favorable condensation spot becomes the Au micro-discs and the Rb droplets have completely condensate on it.
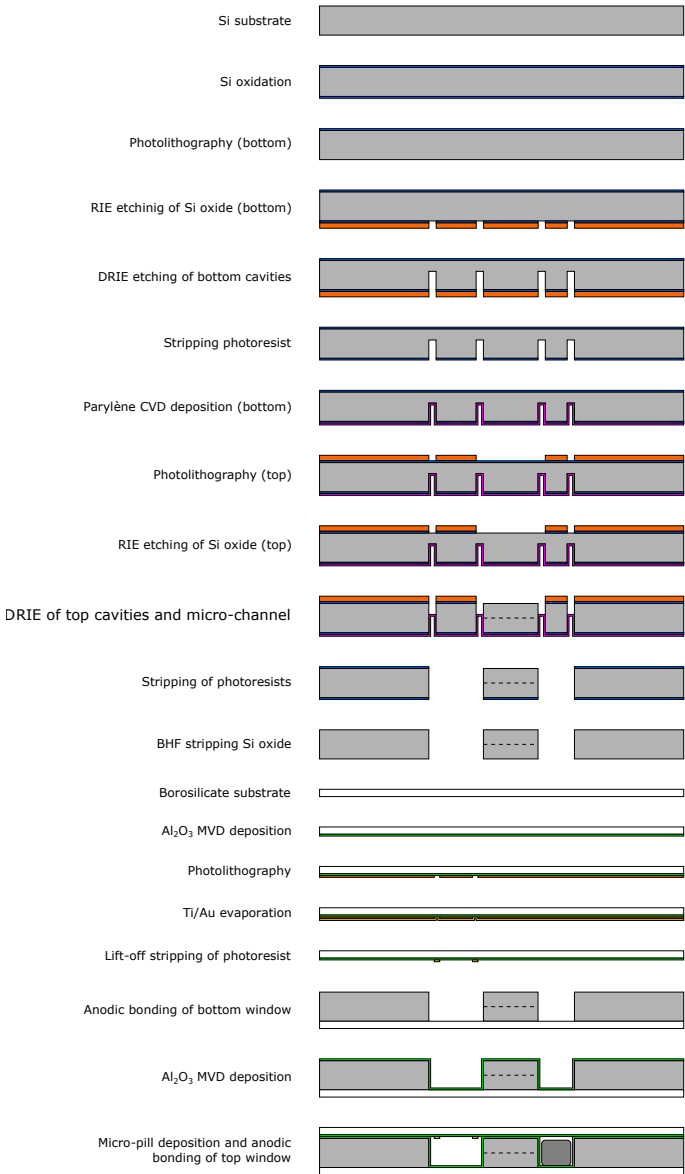
Figure 3.19: Microfabrication process of the anodically bonded cells with Au discs tested in the frame of the present work
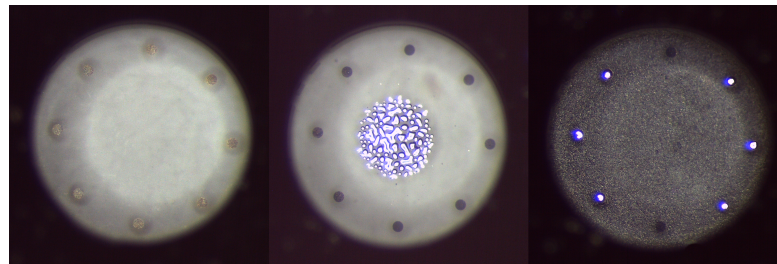
Figure 3.20: Measurement cavity of a MEMS cell with Au micro-discs (view from bottom) [left]: cavity right after activation, [center]: same cavity after heating of the cell on a hot plate during 4 hour, [right]: same cavity after a thermal treatment of 1h at $180°C$.

3.6 Conclusion

From the state-of the art review presented at the beginning of this chapter, Cu-Cu thermocompression was identified as a new wafer-level bonding method suitable for the microfabrication of MEMS atomic vapor cells. An optimization of the Cu structuration and of the bonding parameters was realized. This bonding method was then successfully applied to seal atomic vapor cells.

An alternative filled with rubidium dispensing micro-pills was tested. As the conventional N_2-Ar buffer gas mixture is not compatible with dispensing micro-pills, a novel Ar-Ne buffer gas mixture was moreover developed and used as backfilling. Such cells were successfully produced and the micro-pills were successfully activated in order to release metallic rubidium. These cells are characterized in Chap. 4.

In parallel, MEMS atomic vapor cells filled with UV decomposed RbN_3 were produced together with an Al_2O_3 anti-diffusion coating in order to improve their lifetime. The characterization of such cells is presented in Chap. 5.

Finally, the microfabrication of cells with gold micro-discs was presented. These micro-discs are expected to improve the cell long-term frequency stability. The clock performances of such cells is analyzed in Chap. 6. An optical imaging characterization was nevertheless presented and showed effective condensation of Rb on the Au microdiscs.

4 Spectroscopic characterization of MEMS atomic vapor cells

In the case of MEMS cells used for CSACs, the precise control of the buffer gas pressure inside the cavity is an important parameter. Indeed, the total buffer gas amount must be adjusted in order to obtain a CPT contrast and linewidth matching the target short-term stability (see 2.5.4.2). A precise control of the ratio between the different gas species is also required to minimize the first order dependence of the cell frequency to the temperature (see Sec. 2.5.3.1). On the other hand, for evacuated cells used for laser frequency locking in Doppler-free absorption spectroscopy [185], the purity of the cell content is a crucial parameter and any gas contamination must be avoided inside the cavity.

In this chapter, different methods used to characterize the gas content of MEMS cells are presented: First CPT hyperfine frequency spectroscopy is used on Ar-Ne filled cells. The frequency shift of the 0-0 resonance is used to determine the buffer gas pressure as well as its dependence to temperature and to find the thermal inversion point expected from the mixture used in Chap. 3. The CPT contrast and linewidth are moreover measured for different temperatures and light intensities and the optimal working conditions are determined for Ar-Ne and Ar-N_2 cells. A preliminary measurement of a CPT signal in Cu-Cu thermocompression bonding cell is presented as well. Secondly, micro-Raman spectroscopy is presented. This technique is used as a fast technique to measure the N_2 partial pressure inside Ar-N_2 RbN_3 filled cells. The results are compared with CPT hyperfine frequency spectroscopy results made on same cells. They are moreover used in Chap. 5 in order to calibrate the measurement of Rb quantity by image analysis. Doppler-free absorption spectroscopy measurements used to assess the vacuum level in evacuated Cu-Cu thermocompression bonded cells are moreover presented. Finally, preliminary measurements of Xe nuclear spin decoherence time are presented as well as the setup used to measure it.

4.1 CPT hyperfine frequency spectroscopy

This section describes the spectroscopic measurement made on MEMS atomic vapor cells filled with a dispensing micro-pill and Ar-Ne buffer gas mixture as well as on Ar-N_2 RbN_3 filled MEMS atomic vapor cells.

4.1.1 Setup description

The setup used here is designed such that it allows for the characterization of MEMS atomic vapor cells such that the experimental parameters can be easily tuned. This setup is used for three main goals: the measurement of the buffer gas pressure inside MEMS atomic vapor cells, the measurement of the thermal frequency dependence and the determination of optimal experimental conditions for the interrogation of MEMS cells.

The 0-0 hyperfine frequencies of both ^{85}Rb and ^{87}Rb can easily be measured with such a CPT setup. In order to extract the effect of the buffer gas shift only, the setup presented here is designed in order to measure and to subtract the effect of the light shift and the second order Zeemann shift (see Sec. 2.5.3).
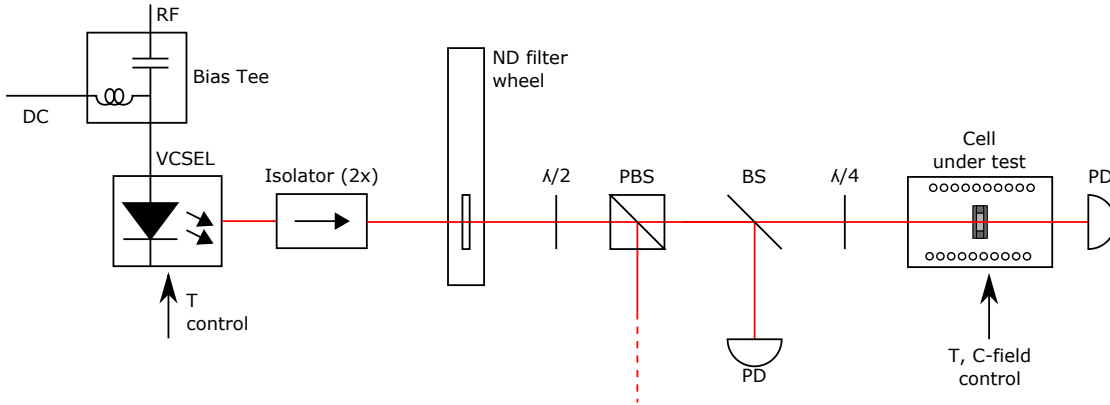

Figure 4.1: Buffer gas pressure measurement setup used for the hyperfine shift measurement technique

Figure 4.1 presents a scheme of the characterization setup. A Vixar 795 nm single mode VCSEL is thermally controlled at a temperature T_{Laser}. An injection current I_{Laser} and an RF modulation at a power P_{RF} is applied to the laser. The laser beam is sent through two 40 dB isolation factor isolators to prevent any back reflection into the laser. After the isolators, the beam is sent to a neutral density filter wheel which allows for an automatic control of the laser power sent to the rest of the setup. The beam crosses then a "$\lambda/2$ - polarized beam splitter system" whose function is to fine tune the optical power and to precisely control the polarization. After that, a part of the beam is sent to a photodiode with a beam-splitter in order to monitor the laser power. The remaining power of the beam crosses a $\lambda/4$ wave-plate in order to apply the σ-polarization required for the CPT to the cell under test placed right after. The cell under test is temperature and C-field controlled and is placed in a double magnetic shielding. The absorption signal is finally detected by a photodiode. This photodiode as well as the photodiode used for power monitoring are calibrated in order to know the exact light intensity getting in and out of the atomic vapor cell.

In operation, the setup is controlled by laboratory electronics: The laser temperature is fixed by laboratory electronics using an NTC. The laser frequency is controlled by adjusting the injection current with the same home-made electronics. At the beginning of the experiment, it is locked on an absorption line of the cell under test by modulation of the laser current at 50kHz and synchronous detection. The laser RF modulation is applied through a bias-tee with an RF generator (Agilent N5181A). This generator is frequency referenced to an OCXO (Oscilloquartz OCXO 8788). The reference cell is temperature controlled using laboratory electronics and the cell under test is C-field and temperature controlled using a numerical controller (SRS PTC10) and an NTC.

The setup can either be operated in open loop condition, with the RF frequency generated by a free reference (the OCXO in free regime) or in close-loop condition (or clock condition), with the RF frequency servo-controlled to the atomic hyperfine transition of the cell under test via the CPT effect. In the last case, the RF frequency is modulated at a given frequency $f_{\text{Mod.}}$ and depth $\Delta\nu^{\text{RF}}$ and synchronously detected using a lock-in amplifier (SRS SR830). The resulting error signal is used to control the OCXO through a PID (SRS SIM960). The OCXO frequency can finally be compared to a reference hydrogen maser (T4Science iMaser) either by using a frequency counter (Hewlett-Packard 53132A) or a phase comparator (SpectraTime Picotime).

4.1.2 Determination of cell intrinsic frequency

The "cell intrinsic frequency" is defined as the ^{85}Rb or ^{87}Rb atomic frequency only perturbed by the buffer gas frequency shift (Eq. 2.68). The light frequency shift (Eq. 2.73) and the magnetic field shift (or second order Zeeman shift, Eq. 2.76) are therefore subtracted using the setup presented above as follows.

4.1.2.1 Measurement procedure

The cell frequency in clock (closed loop) operation is measured at different temperatures and laser powers with a known C-field intensity. From these measurement, the cell intrinsic frequency can be deduced by 0-light intensity extrapolation and subtraction of the second order Zeeman shift. The cell is placed in the measurement setup. The C-field is fixed at a given target value. The cell temperature is fixed at a first desired value and the system is left to thermalize for a couple of hours. The laser is then locked on the optical absorption and remains so for the rest of the measurement. First, the full Zeeman spectrum is measured (see Fig. 4.2). This measurement allows to precisely compute the C-field intensity in view of subtracting its effect to the measured frequency.
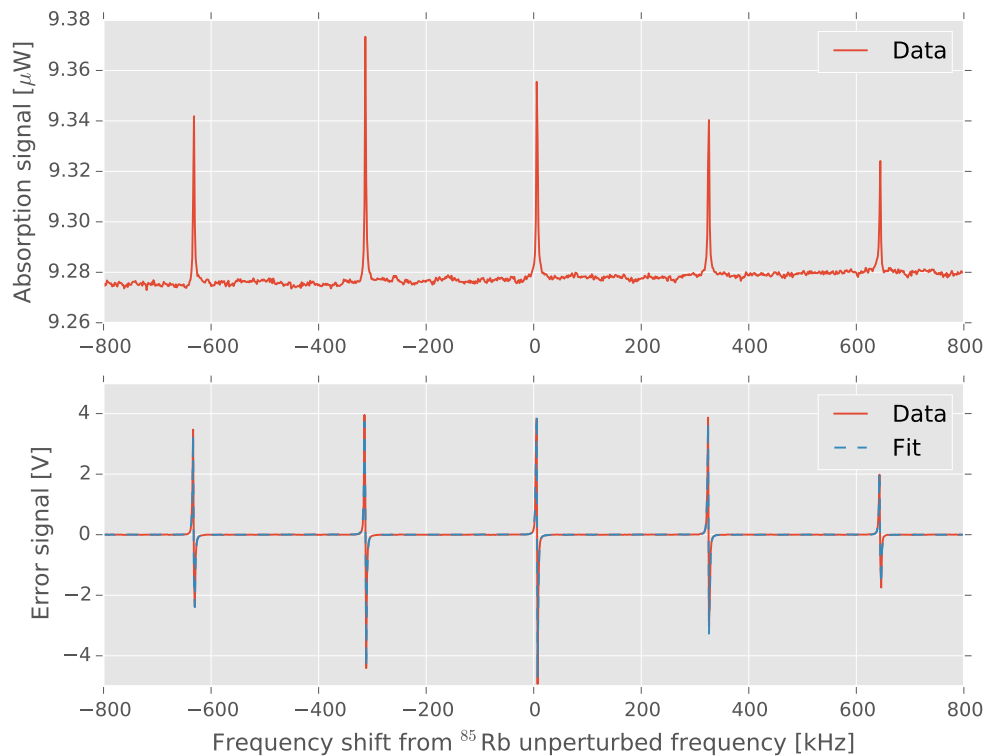
Figure 4.2: Zeeman spectrum measured on a (natural) RbN$_3$ filled Ar-N$_2$ MEMS cell. The fitted magnetic field intensity here is 339.5mG. The Zeeman pumping to lower frequencies suggest that σ^- polarization was used or that the magnetic field and the σ^+ light beam are oriented in opposite directions.

Then, for each measurement temperature, the light power is swept between 10 and 40 μW using the neutral density filter wheel and its precise power is recorded. For each laser power, the absorption

and error signal are recorded and the error signal is fitted to a dispersive lorentzian lineshape (see Fig. 4.3). According to the measured isotope, the RF frequency is then set by adjusting the multiplication factor of the RF generator to the fitted central frequency. The value set on the RF generator frequency is saved and the clock loop is closed. In other words, the error signal is used to servo control the reference quartz which is therefore locked to the center of the CPT absorption signal in order to form a clock. Finally the quartz frequency is compared to the frequency of the reference maser and the quartz frequency is recorded with the counter. The cell target temperature is then changed to the next desired value and the cell is left to thermalize for a few tenth of minutes and the same process in applied until all the required temperatures are measured.
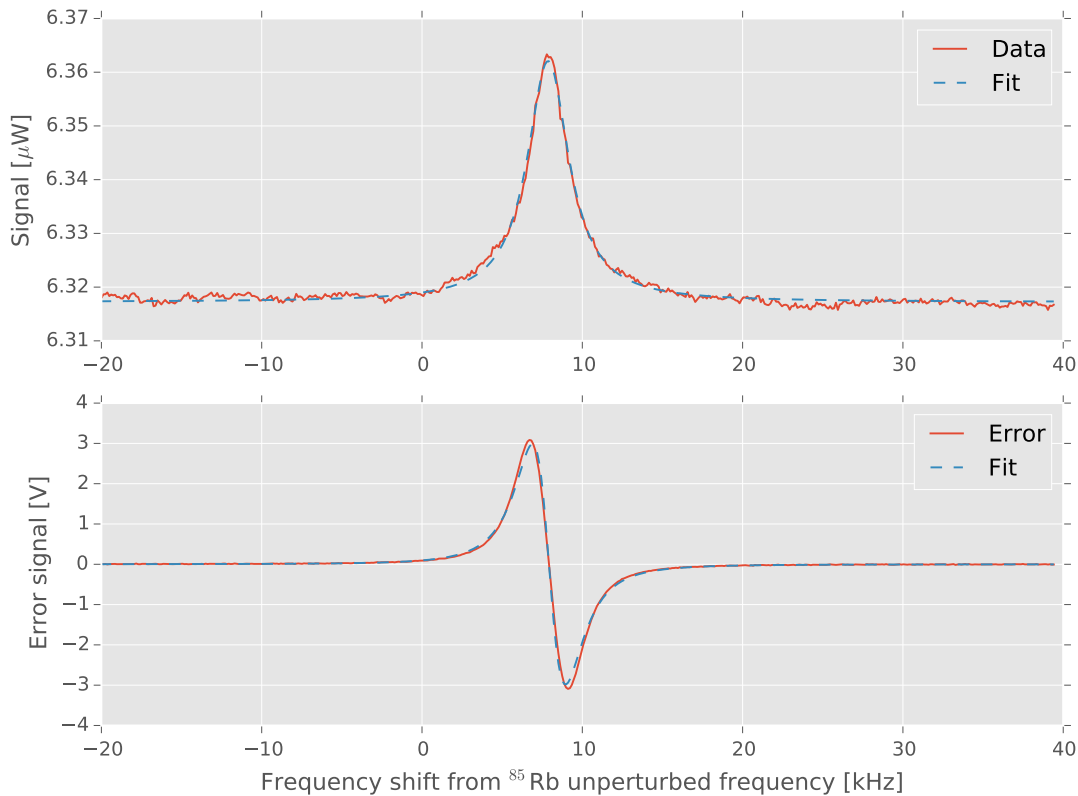
Figure 4.3: CPT signal measured on an anodic bonding, natural Rb (filled with dispensing micro-pill) Ar-Ne (100 mbar) MEMS cell with an input intensity of 15.7 μW at 95°C. The fitted linewidth is 3.577 kHz, and the contrast is 0.71%. The absorption signal is the cell output light power.

For each temperature and light intensity, the clock frequency can therefore be calculated from the quartz frequency measured against the maser reference and the multiplication factor of the RF generator. Moreover, the C-field intensity in the cell is known by fitting of the the preliminary recorded Zeeman absorption spectrum (see Fig 4.2).

4.1.2.2   Extrapolation to 0 light shift

From measurements made for each cell temperature, the 0-light intensity frequency is calculated: the magnetic field frequency shift is subtracted from the values determined by fitting of the Zeeman spectrum. The 0-light intensity extrapolation is then realized by a linear fit on the measured values. For each calculation, the 95% confidence interval is estimated taking into account the error on the

fit and on the different measurements (see Fig. 4.4).

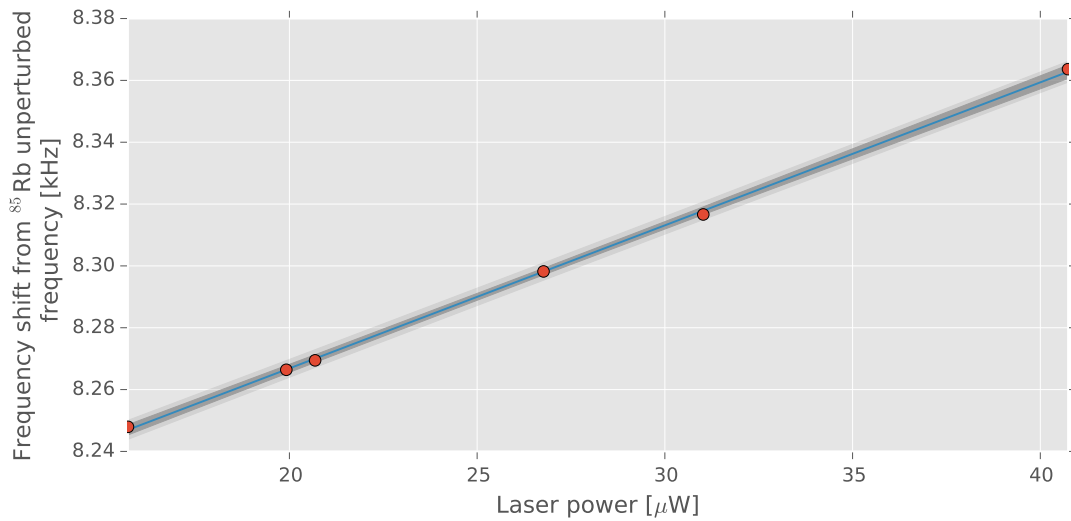Figure 4.4: 0-light shift extrapolation of CPT clock frequency shift for a natural Rb (filled with dispensing micro-pill) Ar-Ne (100 mbar) MEMS cell at 95°C. The frequency shift is given from the Rb intrinsic frequency, the light power is the power at the cell input.

4.1.3 Temperature dependence of Ar - Ne cells frequency

As presented in Chap. 3, a new buffer gas mixture had to be developed for dispensing micro-pills. Indeed, the traditionally used N_2 is not compatible with the dispensing micro-pills which act as a getter. This buffer gas is composed of a mixture of Ar and Ne at a target ratio of 27% of Ar which gives a target inversion temperature of 95.2°C. The gas mixture prepared by the gas supplier gave a effective ratio of 26.87% which corresponds to an expected inversion temperature of 89.04°C.

   Two full wafers were realized with this buffer gas mixture. The target buffer gas total pressure was respectively 150mbar at 95°C for run 1 and 100 mbar at 95°C for run 2. The cells were measured in the setup described in Sec. 4.1.1. The intrinsic cell frequency was measured in function of the temperature for both runs. The results are presented in Figs. 4.5 and 4.6. In the present case, the shift from the unperturbed ^{85}Rb hyperfine frequency is measured in natural rubidium. The total pressure and the thermal inversion point was measured. An effective inversion temperature of 89.9±1.0°C was measured for run 1 which is in accordance with the expected values. For run 2 however, an inversion temperature of 83.6°C was measured. This value is not in accordance with the expected values. Moreover, a large deviation from a quadratic dependence was observed as compared to run 1 (see Fig. 4.6).

   The total pressure of both runs was moreover computed. A value of 146.1±0.5mbar for the first run and 97.1±0.3 mbar for the second run were measured. They are given by the sum of the shift of the two gas components (Eq. 2.68) calculated for the 95°C measured value with the mixture calculated from the measurement of the inversion temperature of run 1. The measured values are close to the target values of 150 mbar and 100 mbar respectively.

   These two results show that Ar-Ne mixture can be used to tune the inversion temperature to the desired value within the operation range of MEMS cells (here 95°C). Moreover, a relative error on the filling pressure accuracy of -2.6% and -2.9% could be achieved showing the good reproducibility of the buffer gas filling method.
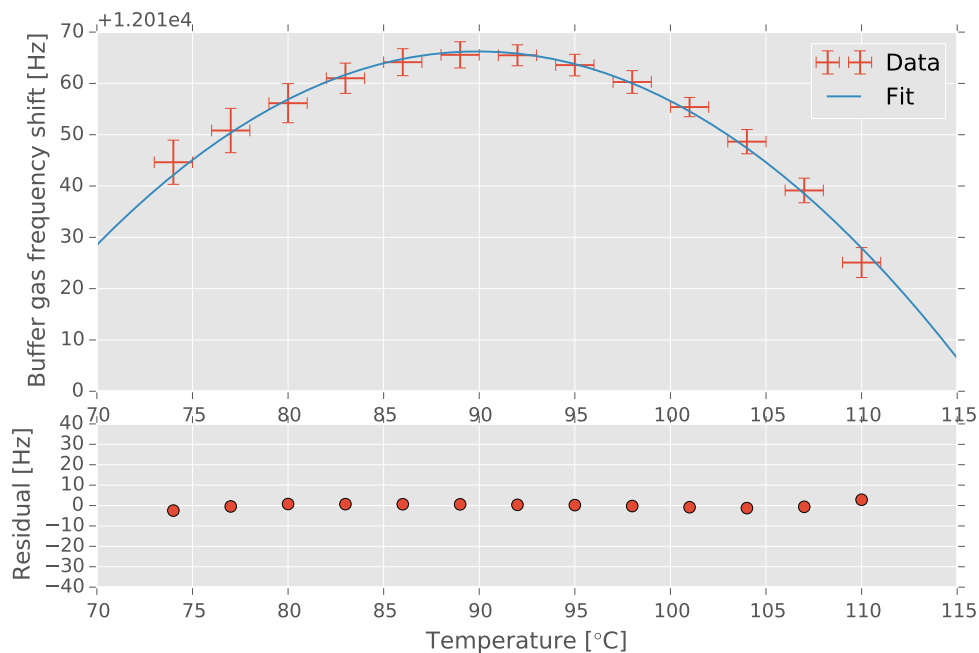
Figure 4.5: Temperature dependence of the buffer gas frequency shift for run 1 (150 mbar Ar-Ne at 95°C target pressure, measured on the [85]Rb isotope of natural Rb)
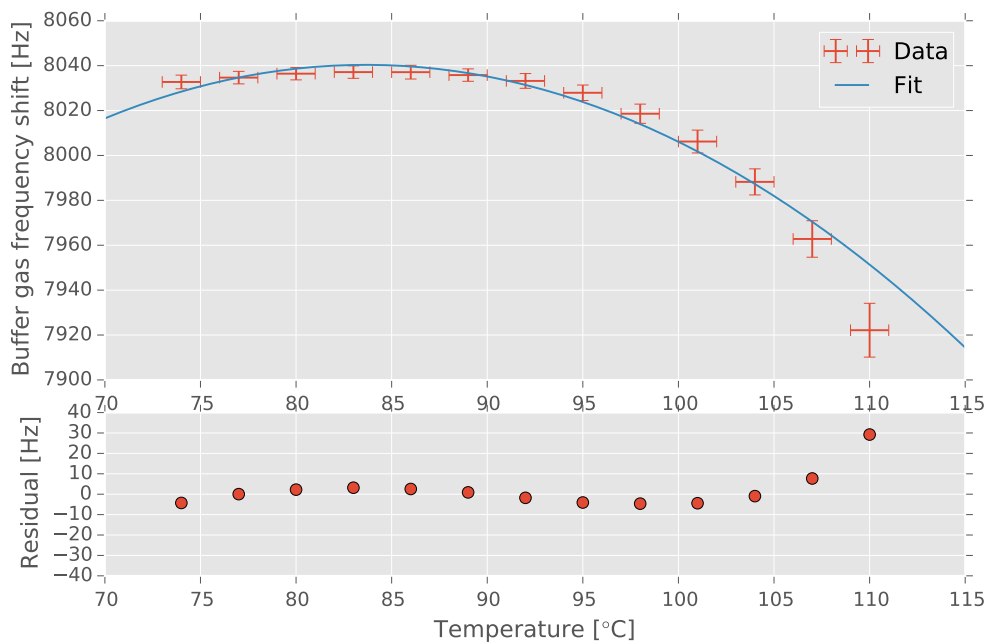

Figure 4.6: Temperature dependence of the buffer gas frequency shift for run 2 (100 mbar Ar-Ne at 95°C target pressure, measured on the [85]Rb isotope of natural Rb)

4.1.4 Contrast and FWHM of Ar - Ne cells

In addition to the thermal inversion point, the CPT contrast and FWHM of the Ar-Ne filled cells were measured for an [85]Rb interrogation in natural rubidium. These are major parameters to be tested as the clock shot-term frequency stability is determined by them (see Sec.2.5.2). During the frequency measurement procedure presented in Sec. 4.1.2.1, the CPT signal is recorded for each cell temperature and light intensity. Fig. 4.7 and 4.8 show the contrast, CPT FWHM, FoM and extrapolated short-term frequency stability for run 1 and 2 respectively and for each temperature and light power combination. The 1 s short-term frequency stability is estimated using the noise parameters given in Sec. 2.5.2. As expected, linewidth increases with the temperature and light power due to the increasing of the hyperfine relaxation rate with these two parameters(see Sec. 2.4.2). The contrast in the other hand, reaches a maximum around 105°C for the 150 mbar cell and around 100°C for the 100 mbar cell. This is as well in accordance with the expected behavior for MEMS cells. Indeed, such cells require a higher working temperature than cm-size glass-blown cells in order to reach a sufficient atomic density for the mm-size lightpath in the cell. At higher temperature however, the absorption becomes too high and the signal drops. The optimal working point is given by the FoM. For the 150 mbar cell, it is in the order of 100°C and close to or above 40 μW, which is the maximum power delivered by the VCSEL in the experimental conditions. For the 100 mbar cell, the absolute value is lower and in the order of 95°.

Figure 4.7: CPT spectroscopic parameters for a cell filled with 150 mbar Ar-Ne buffer gas (run 1), measured on the [85]Rb isotope of natural Rb - The 1 s stability is estimated with the total noise parameters given in Sec. 2.5.2 (not measured experimentally
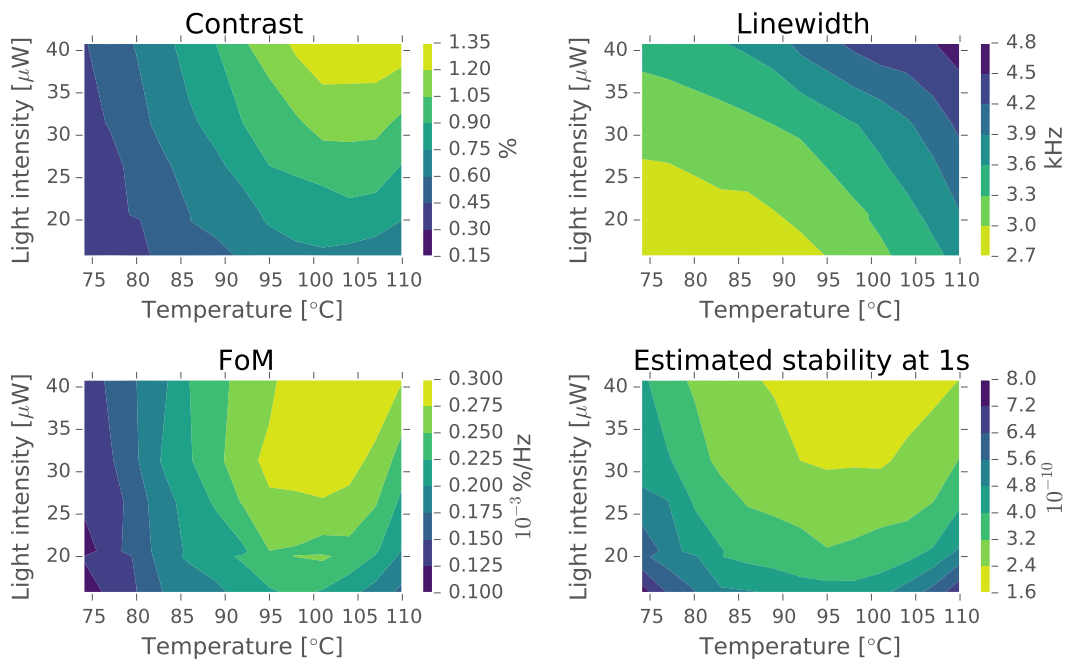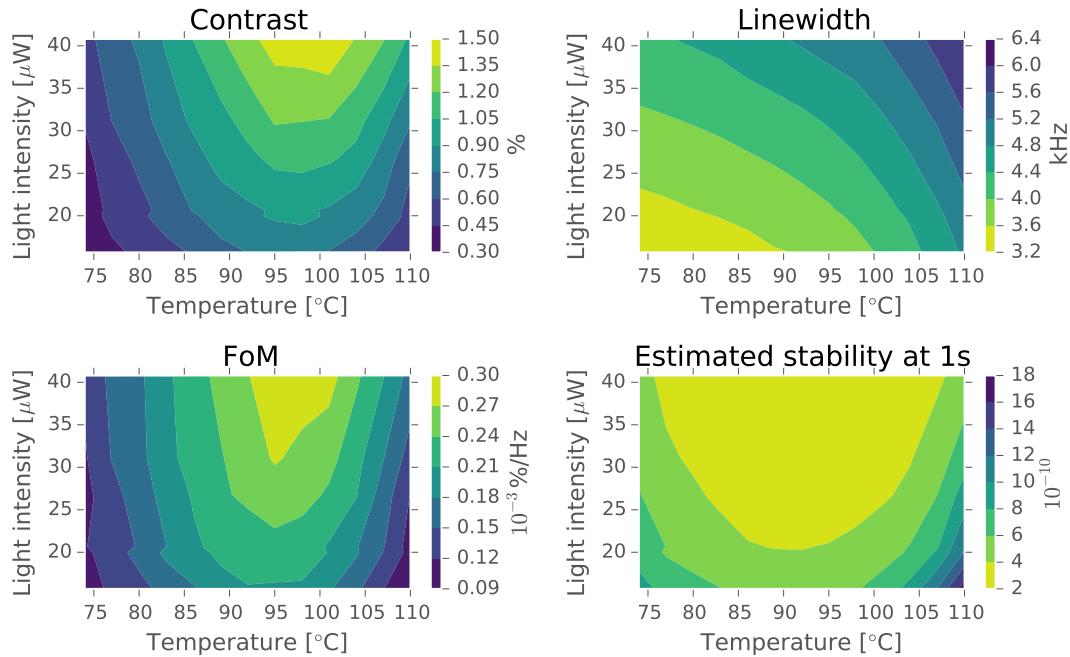
Figure 4.8: CPT spectroscoic parameters for a cell filled with 100 mbar Ar-Ne buffer gas (run 2), measured on the ^{85}Rb isotope of natural Rb - The 1 s stability is estimated with the total noise parameters given in Sec. 2.5.2 (not measured experimentally)

4.1.5   Preliminary CPT measurement in Cu - Cu thermocompression cell

A preliminary CPT measurement was realized on the ^{85}Rb D1 line of an Ar-Ne Cu-Cu thermocompression cell filled by dispensing micro-pill with natural rubidium. Its detailed fabrication process is described in Sec. 3.2.6. Due to a malfunction of the bonder during the bonding process, the exact buffer gas pressure is not known. A target value of 150 mbar Ar-Ne mixture was expected and therefore, an effective value in the 100 to 150 mbar range can be supposed. A measurement of the CPT signal of ^{85}Rb is presented on Fig. 4.9. A FWHM of 3.57 kHz with a contrast of 0.80% was measured with an input laser power of 16 μW on a cell heated at 95°C. These values are comparable to FWHM and contrast values measured for MEMS cells sealed by anodic bonding in the same conditions (See Sec. 4.1.4). Therefore, these preliminary measurements confirm the potential of Cu-Cu thermocompression bonding as an alternative method for MEMS cells sealing.
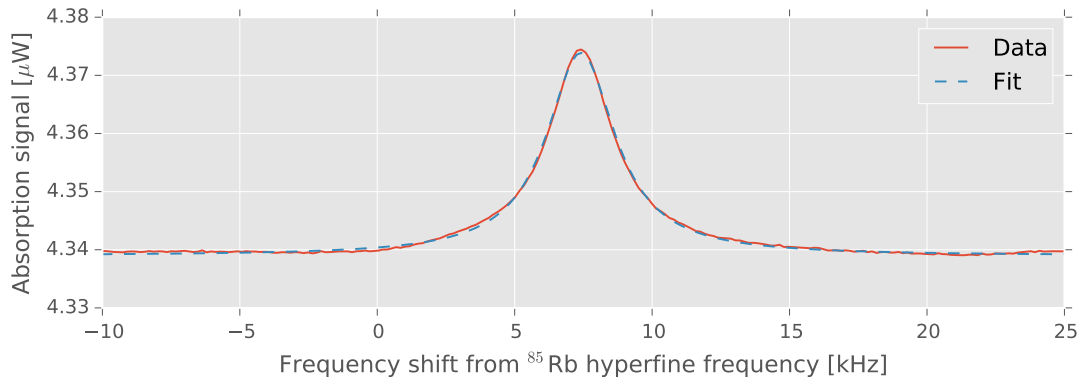
Figure 4.9: CPT signal measured on a Cu-Cu thermocompression bonding, natural Rb (filled with dispensing micro-pill) Ar-Ne MEMS cell with an input intensity of 16 μW at 95°C. The fitted linewidth is 3.57 kHz, and the contrast is 0.80%. The absorption signal is the cell output light power.

4.1.6 Pressure determination for Ar - N$_2$ cells

The partial N$_2$ and Ar pressures of MEMS atomic vapor cells filled with RbN$_3$ can determined by the buffer gas shift of the Rb hyperfine frequency and its dependence to temperature. It is given by the sum of the shift of the two gas components (Eq. 2.68). In the present case, the shift from the unperturbed ^{85}Rb hyperfine frequency in natural rubidium was measured. The method nevertheless remains the same in the case of isotopically selected^{87}Rb. The light shift was extrapolated to 0-light intensity (see Fig. 4.4) and the second order Zeeman shift was subtracted. The partial pressures of Ar and N$_2$ were finally extracted by fitting of the temperature dependence of the hyperfine frequency shift (see Fig. 4.10). Here a direct fit of Eq. 2.68 with the coefficients given in Tab. 2.6 is realized. The obtained results are compared to the results obtained by Raman spectroscopy for the estimation of N$_2$ partial pressure and serve to validate the method (see Sec. 4.2.2).

Figure 4.10: Fitting of the Ar - N$_2$ buffer gas shift example on a natural RbN$_3$ filled MEMS cell - In the present example, an Ar pressure of 8.7$\pm$2 mbar and a N$_2$ pressure of 57.6$\pm$0.3 mbar at 300 K was measured.

4.1.7 Contrast and FWHM of Ar - N$_2$ cells with isotopically selected ^{87}Rb

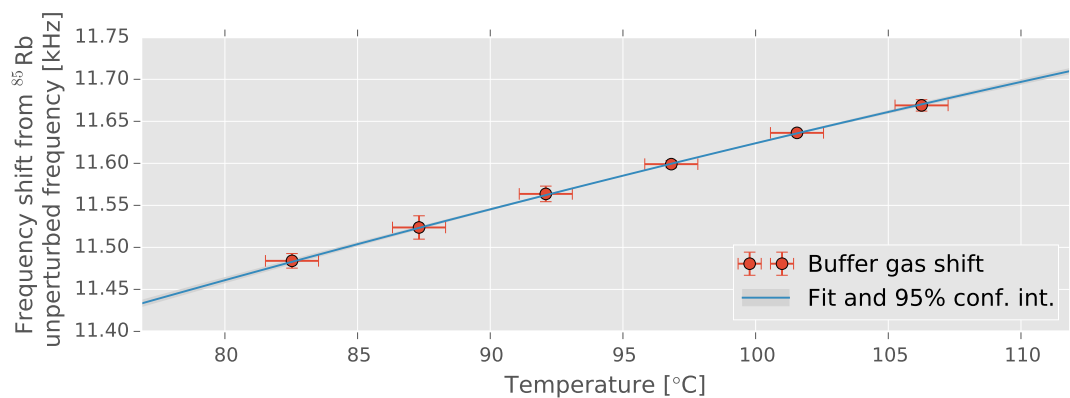The CPT contrast and FWHM of an Ar-N$_2$ cell filled by ^{87}RbN$_3$ UV-decomposition was measured with the same procedure as for Ar-Ne cells (see Sec. 4.1.4). Moreover, the buffer gases partial pressures of the cell were calculated as in Sec. 4.1.6. An Ar pressure of 74.2±1.9 mbar and a N$_2$ pressure of 35.0±0.3 mbar at 300 K was measured which gives a total pressure in the order of 110 mbar. No particular optimization of the RbN$_3$ filling and UV-decomposition was realized for that cell.

The CPT contrast and FWHM measurements results are presented on Fig. 4.11. The contrast reaches a maximum in the 115°C region, a higher temperature than for natural Rb Ar-Ne MEMS cells probed in the ^{85}Rb D1 line (see Sec. 4.1.4). Moreover, the measured contrast values are higher. This is easily explained by the fact that in the case of an isotopically selected isotope, all the atoms can participate to the signal. The measured linewidth are on the other hand larger than for natural Rb. This is an expected behavior as the buffer gas broadening coefficients are proportional to the isotope hyperfine frequency ($\approx$3.036 GHz for ^{85}Rb and $\approx$6.835 GHz for ^{87}Rb). The optimal working point given by the FoM is in the order of 105 to 110°C and at a light power in the order of 15 μW. Finally, as expected for a MEMS cell filled with an isotopically selected isotope the estimated short term frequency stability is lower than for natural Rb.
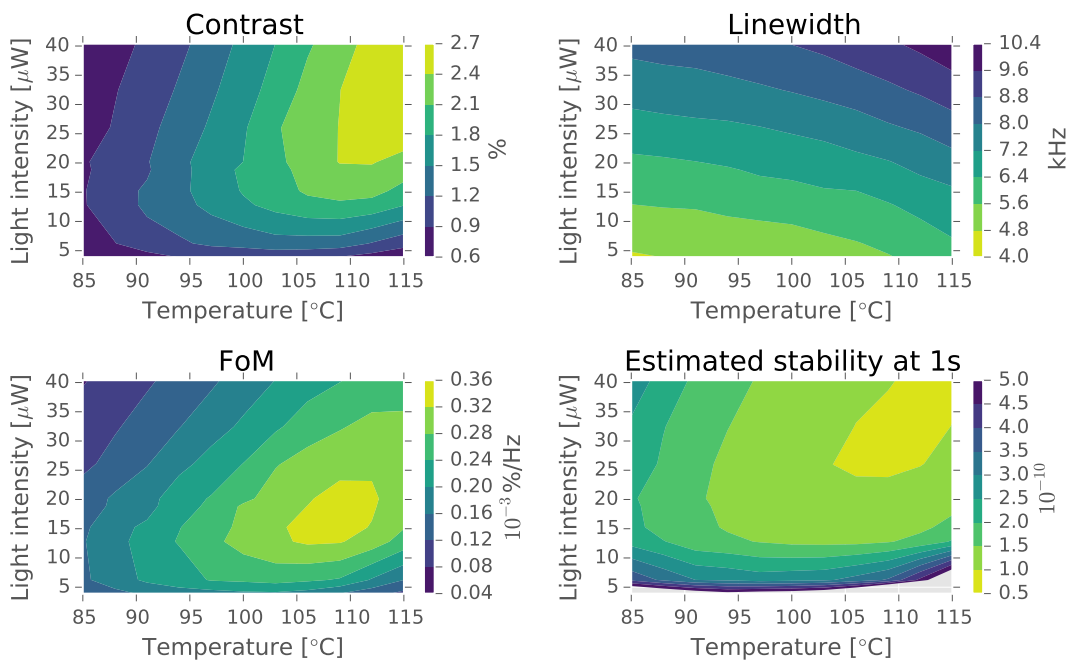

Figure 4.11: CPT spectroscopic parameters for a ^{87}Rb cell filled with $\approx$110 mbar Ar-N$_2$ buffer gas- The 1 s stability is estimated with the total noise parameters given in Sec. 2.5.2
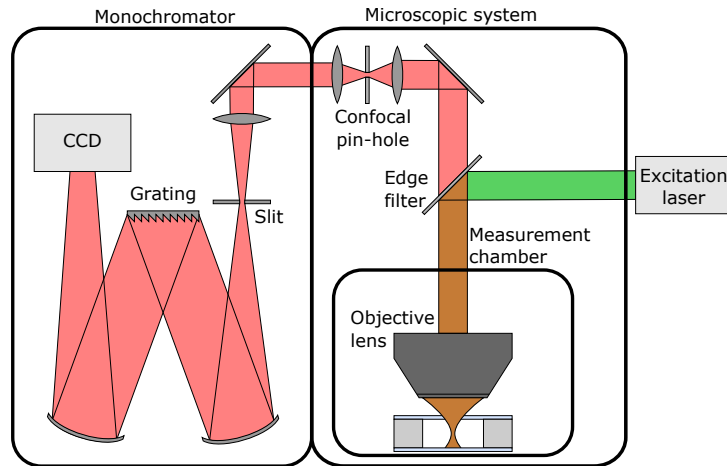
Figure 4.12: Scheme of the Raman spectroscopy experiment (CCD: charge coupled device sensor) [187] - **Copyright © 2017 SAGE Publication. Reprint by permission of SAGE Publication.**

4.2 Nitrogen partial pressure determination by Raman spectroscopy

4.2.1 Description of measurement

Raman spectroscopy is a non-invasive method, which relies on the optical measurement of molecular vibrations in order to characterize solids, liquids and gases. In this case, it has only the capability to measure molecular gases. It was proposed as a relatively fast mean of analyzing gases in devices having an optical access to the sealed cavity [186]. Here, the N_2 buffer gas partial pressure inside RbN_3 filled MEMS cells is measured with this technique. It allows to measure the N_2 pressure in a wider range than the hyperfine spectroscopy method (see Sec. 4.1.6). Moreover, it does not require the presence of metallic Rb and offers a faster acquisition time. This method is reported in [187] and relies on the following principle:

In gases, the Raman scattered intensity of a branch is given by [188]:

$$I_{\text{scat.}} = I_0 N V_{\text{P}} \frac{\pi^2}{\varepsilon_0^2 \lambda^4} \frac{d\sigma}{d\Omega} \tag{4.1}$$

where I_0 is the incident laser intensity, N is the density of the scattering species in the probed volume V_{P}, λ is the excitation laser wavelength and $\frac{d\sigma}{d\Omega}$ is the differential scattering cross-section. This value depends on the particular experimental conditions, such as the signal collecting geometry, the incident laser beam polarization and the studied species. If experimental conditions are kept constant between two measurements the difference in the measured Raman intensity is only proportional to the difference in the density of molecules in the probed volume *i.e.* $I_{\text{scat.}} \propto N$. A the molecular density is linked to the partial pressure p by the ideal gas law $pV = Nk_{\text{B}}T$, where V is the volume, T is the temperature and k_{B} is the Bolzmann constant. $I_{\text{scat.}}$ is therefore proportional to p.

The Raman spectra presented here were obtained with LabRAM ARAMIS (Jobin Yvon Horiba) micro-Raman spectrometer (see Fig. 4.12). This instrument consists in a confocal optical system, a monochromator and an excitation laser which test chamber can be purged with Ar. The experimental conditions are fixed as follows: The 532 nm, incident laser power is fixed at the cell location at 33 mW. The laser beam is focalized at the center of the cell cavity (at $\approx 500 \ \mu$m under the glass cover). A 100X
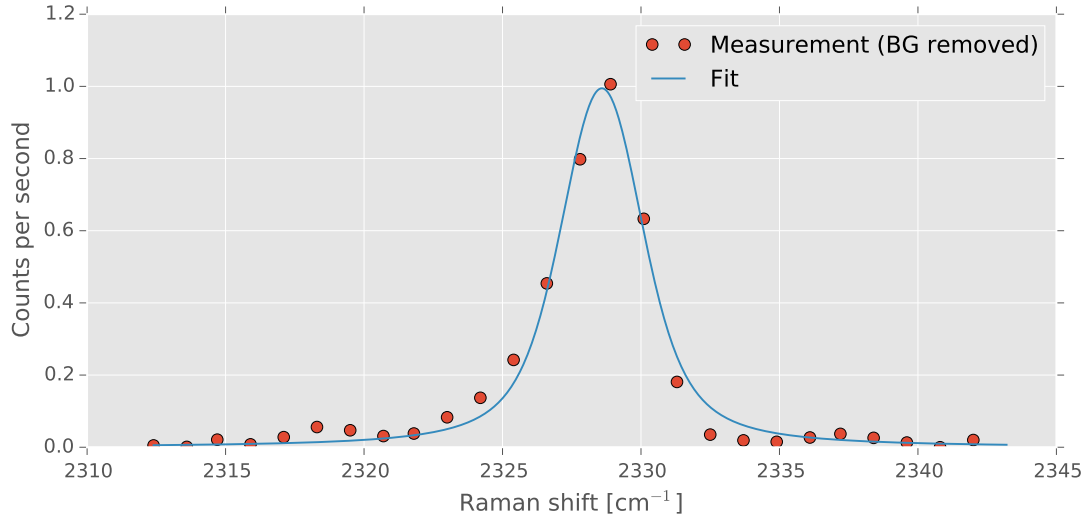
Figure 4.13: Example of Voigt profile used to fit the Q branch of N_2 (background removed) - **Experimental data: courtesy of Jean Gobet, CSEM**

long working distance objective (NA = 0.80, working distance = 3.4 mm) and a pinhole diameter of 300 μm are chosen to minimize the confocal region. The scattered signal is finally measured using a 1200 grooves/mm diffraction grating.

The Q branch of N_2 at $v = 2328$ cm^{-1} was measured (see Fig. 4.14). Prior to the actual measurement, a calibration of the measured scatter intensity is required. It is done as follows: The chamber of the instrument is filled with atmosphere. The N_2 partial pressure is therefore $p_{N_2,atm.}=761$ mbar. The scattered signal is measured over one hour integration time. The background is then removed and the scattered spectrum is fitted with a Voigt profile in order to extract Q branch of N_2 peak intensity as shown in Fig. 4.13. As the Raman frequency shifts does not need to be precisely measured, this simple fitting profile is sufficient here and the asymmetrical five-parameter Pearson line shape function used by Weber et al. [186] was not required in the present case.

The same measurement is repeated after purging the instrument's measurement chamber with Ar such that the partial pressure of N_2 is 0. In that case, the signal intensity I_{Ar} is recorded over one hour as well. The residual N_2 Raman scattering signal (see Fig. 4.14) was identified as the scattering of the laser with N_2 present in the instrument outside of the test chamber. After this calibration process, the Raman intensity I_{cell} can be measured inside the cell cavity. From Eq. 4.1, the pressure in the cell is given by:

$$p_{N_2,cell} = \frac{I_{cell} - I_{Ar}}{I_{atm.} - I_{Ar}} p_{N_2,atm.} \tag{4.2}$$
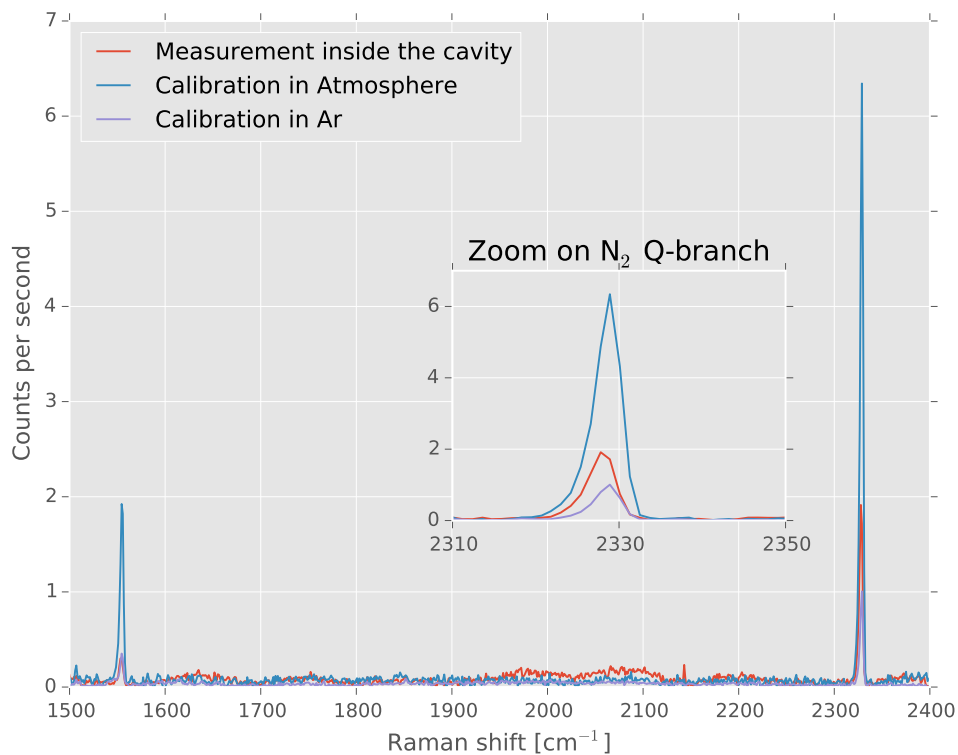
Figure 4.14: Experimental μ-Raman spectra used for N_2 pressure measurement: Calibration in atmosphere, calibration in Ar and measurement inside a sealed MEMS cell cavity - **Experimental data: courtesy of Jean Gobet, CSEM**

4.2.2 Comparison of results

The results of measurements made by the Raman method were compared with measurements made by CPT frequency shift measurements (see Sec. 4.1.6) for three cells and showed good agreement (see Fig. 4.15). An absolute difference below 2 mbar was measured and a Pearson correlation coefficient of $r = 0.99975$ and a 95% limit of agreement of -2.9 to 4.3 mbar for the Raman measurement method was computed.

In conclusion, the Raman method allows to measure the N_2 partial pressure in a much wider pressure range than the hyperfine spectroscopy method, without the required presence of Rb and with a faster acquisition time. It will be used in Chap. 5 in order to calibrate the Rb droplet size measurement in order to characterize the lifetime of Al_2O_3 coated cells.
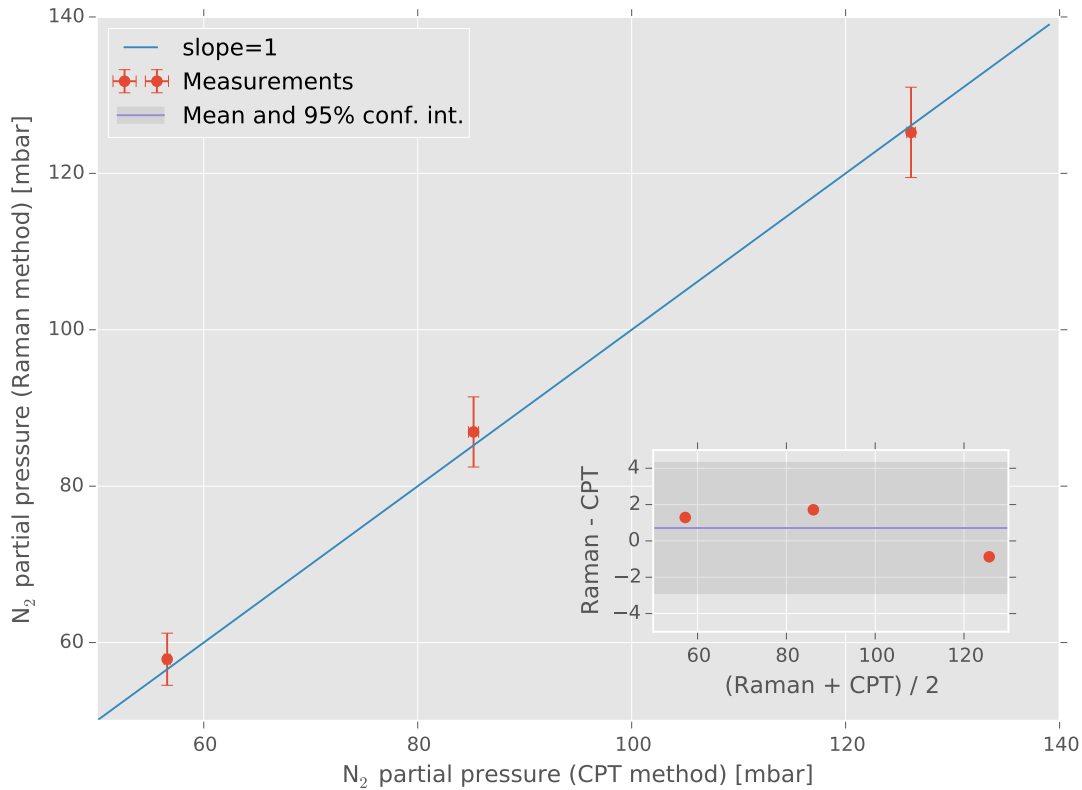
Figure 4.15: Comparison between the N_2 partial pressure determined by Raman spectroscopy and the N_2 partial pressure determined by CPT spectroscopy - [insert] Tukey mean-difference plot - **Raman experimental data: courtesy of Jean Gobet, CSEM**

4.3   Vacuum level assessment by Doppler-free absorption spectroscopy

4.3.1   Setup description

A Doppler-free absorption spectroscopic setup was designed to assess the gas contamination inside nominally pure (without buffer gas) vapor cells [84, 38]. Fig. 4.16 shows a block diagram of this setup. A DFB laser resonant with the Rb D1 line at 795 nm (Eagleyard EYP) is used in order to have a sufficiently narrow linewidth (typically in the order of 10 MHz) and a sufficient laser power. The (high power) laser beam passes through a beam splitter and is sent to the cell under test as a pump beam. It is then reflected by a mirror and crosses two times a neutral density filter which reduces its power. It is then sent to the cell in opposite propagation direction as the probe beam. The deviated portion of this beam is detected by a photo-diode. The laser injection current is swept in order to scan over the Rb D2 absorption line. The resulting spectrum presents small transmission features within the ≈500 MHz wide Doppler broadened absorption lines. These so-called Doppler-free transmission lines correspond to rubidium atom velocity classes that have been pumped and probed by the laser at the same frequency, *i.e.* with a 0 velocity in the beam direction. This frequency corresponds to a direct optical transition (direct transition dip). Transmission dips can also correspond to velocity classes that have been pumped by the blue-shifted laser beam and that are probed by the red-shifted laser

beam. In this case, the transmission dip is located at the mean between the two optical absorption frequency (cross-over dip).

The lorentzian width of these dips is only due to the natural linewidth of rubidium, to the broadening induced by the laser linewidth and saturation effects and to the buffer gas broadening. The effect of the Doppler broadening is removed. By comparison of the absorption spectrum of a MEMS cell to the reference spectrum of a cm-size cell, it is therefore possible to extract the excess broadening due to a contaminating buffer gas and to calculate the buffer gas pressure. (See Tab. 2.3 for typical broadening values of commonly used buffer gases.)
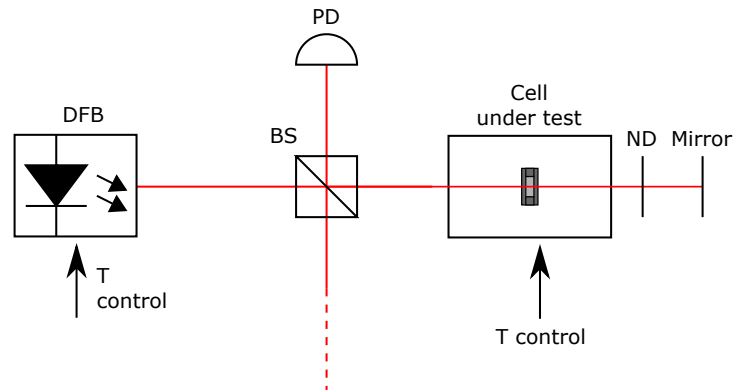

Figure 4.16: Doppler-free absorption spectroscopic setup

4.3.2 Cu-Cu thermocompression bonding cells

The vacuum level of Cu-Cu thermocompression cells filled with natural Rb dispensing micro-pills was assessed by Doppler-free absorption spectroscopy. The lorentzian width of the $5^2S_{1/2}$,F=2 → $5^2P_{3/2}$F=2 CO 3 of ^{87}Rb was measured (see Fig. 4.17). The linewidth was measured at different light power between 20 and 100μW. The linewidth was extrapolated to 0-light intensity in order to remove excess broadening (see Sec. 2.3.2.3). A liner extrapolation was chosen due to the relatively high dispersion of the measured values (see Fig. 4.18). A Lorentzian linewidth of 44.8±2.7 MHz was thereby measured. After subtraction of the natural linewidth of ^{87}Rb, the buffer gas induced broadening is 38.8±2.7 MHz.

The source of residual buffer gas is difficult to identify. The most probable candidate is argon. Indeed, this gas is used as inert medium in the forming gas mixture and is present during the last purge phase of the microfabrication. In this case, with the coefficients of Tab. 2.3, a residual pressure of 2.1±0.2 mbar of Ar can be estimated.

In order to compare these results with the values measured by Straessle et. al for In bonded cells [39], a nitrogen equivalent pressure can be computed. In the present case however, N_2 is trapped by the Zr compound of the dispensing micro-pill and its presence is unlikely inside the cell. Nevertheless, taking the coefficients of Tab. 2.3, a residual pressure of 2.4±0.2 mbar of N_2 can be computed. This contamination value is higher than the value measured in [39]. This can be explained by the higher bonding temperature of the cells (400°C vs 140°C) which implies a higher outgasing rate or by the fact that these cells are bonded at a wafer level whereas the In bonded cells were fabricated chip-scale. Indeed, in the first case, a good vacuum level is much harder to obtain due to the long diffusion path of the gas molecules between the two wafers separated by only 300 μm.
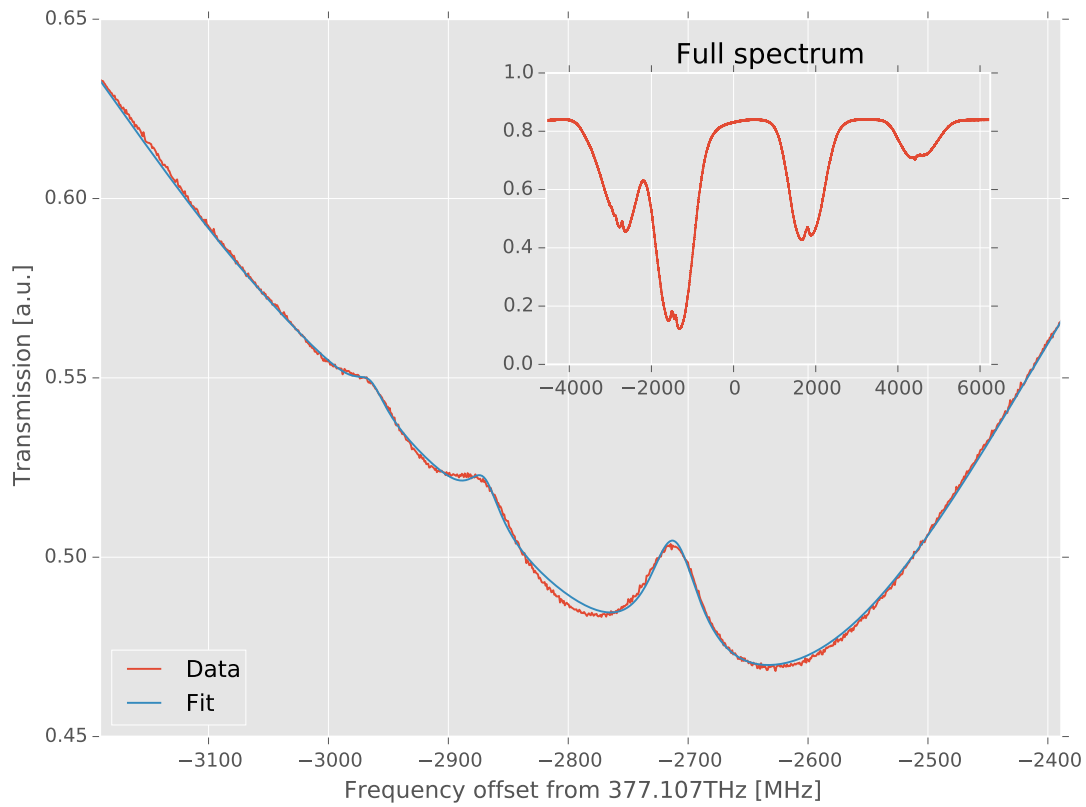
Figure 4.17: Doppler-free absorption spectrum example: data and fit - Insert: full spectrum
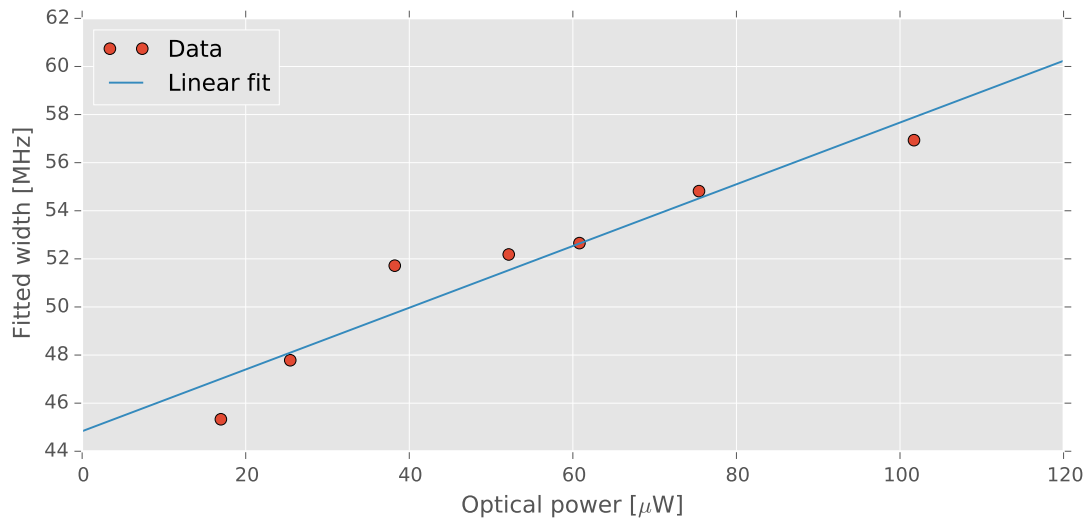

Figure 4.18: 0-light extrapolation of the selected Doppler-free fitted linewidth

4.4 Preliminary measurement of Xe relaxation

To evaluate the Xe spin relaxation time T_2^* in MEMS cells for applications in atomic gyroscopes, an experimental setup was developed in order to measure the free induced decay of Xe. The results reported here were presented in [189]. No rigorous optimization of the experimental parameters such as the magnetic field or the light intensity were performed and only preliminary results are presented. A more rigorous characterization of Xe spin relaxation time T_2^* and in particular a temperature dependence was reported recently in [190].

The field-switch technique described in 2.7 was used. A MEMS cell is placed in a 3 layer magnetic shield at the center of a 3-axis coil. (see Fig. 4.19) The Al_2O_3 coated MEMS cell consists in a circular cavity of 4 mm diameter and 1 mm thickness sealed by anodic bonding. It is filled with natural RbN_3 using UV decomposition and isotopically enriched Xe (50% ^{129}Xe, 50% ^{131}Xe). The target pressures of Xe and N_2 are 50 and 200 torr respectively. Enriched Xe is used to increase the useful atomic density and therefore the useful signal whereas N_2 is used for its quenching effect.
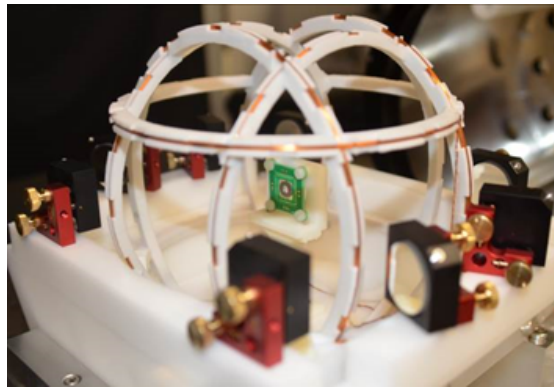
Figure 4.19: Picture of the Xe spin relaxation time measurement setup

In order to avoid any magnetic interference in the system, the thermal regulation of the cell in made by a fully optical system: An infrared temperature sensor is used to measure the cell temperature and the cell is heated by an off-resonant laser emitting at 976nm. The cell temperature is stabilized at $\approx 160°C$ bz means of a feedback loop implemented with a digital PID. The experimental procedure described in Sec. 2.7 and depicted in Fig. 2.9 is implemented. A schematic of the experiment is presented in Fig. 4.20. A DFB laser resonant at 795 nm is used to both pump the Rb atomic vapor and probe the absorption. The transmitted light intensity is measured by a photodiode. The experimental parameters used here are chosen according to [3]. The AC magnetic field frequency is fixed at 2 kHz with an amplitude of $\approx 1\mu T$. The static magnetic field is in the order of a few μT and oriented at $\phi \approx 45°$. As mentioned above, no precise control of the residual magnetic field was made before the experiment.

After switching the magnetic field, the free induction decay signal of the Xe spins is measured by demodulating of the transmitted light signal. The lock-in amplifier used for this purpose is referenced with the 2kHz frequency used for the AC magnetic field generation. An example of such measurement is shown on Fig. 4.21. The FFT of this signal shows the spectral response of the Xe. The relaxation time T_2^* can be measured from the Lorentzian FWHM of resonance lines [190]. The decay of the two Xe isotopes can be observed in two separate lines. This is due to the different gyromagnetic ratio of the two isotopes. (see Tab. 2.8) Moreover, ^{131}Xe experiences a splitting of the resonance lines in opposition to ^{129}Xe. This is due to the nuclear quadrupole interaction of the nucleus due to its higher nuclear spin (3/2 for ^{131}Xe versus 1/2 for ^{129}Xe), see [102] for details.

T_2^* values measured by Lorentzian fitting of the central ^{131}Xe line and of the ^{129}Xe line correspond
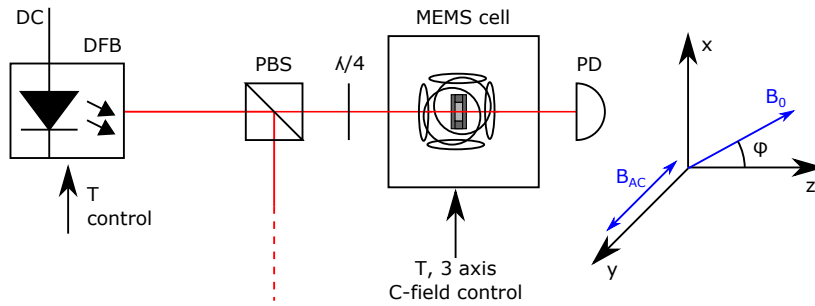
Figure 4.20: Schematic of the Xe spin relaxation time measurement

to relaxation times of 1.3 s and 9.1 s respectively. These values are in the order of magnitude of the 5 s value measured by Donley et al. in [102]. However, the difference between the linewidth of the two isotopes observed here is a probable indicator of magnetic field inhomogeneities. Nevertheless, the central frequencies are found to be respectively 2.5 Hz and 8.3 Hz which both correspond to a magnetic field of 0.71 μT (see Eq. 2.80). A detailed investigation is left to future studies.
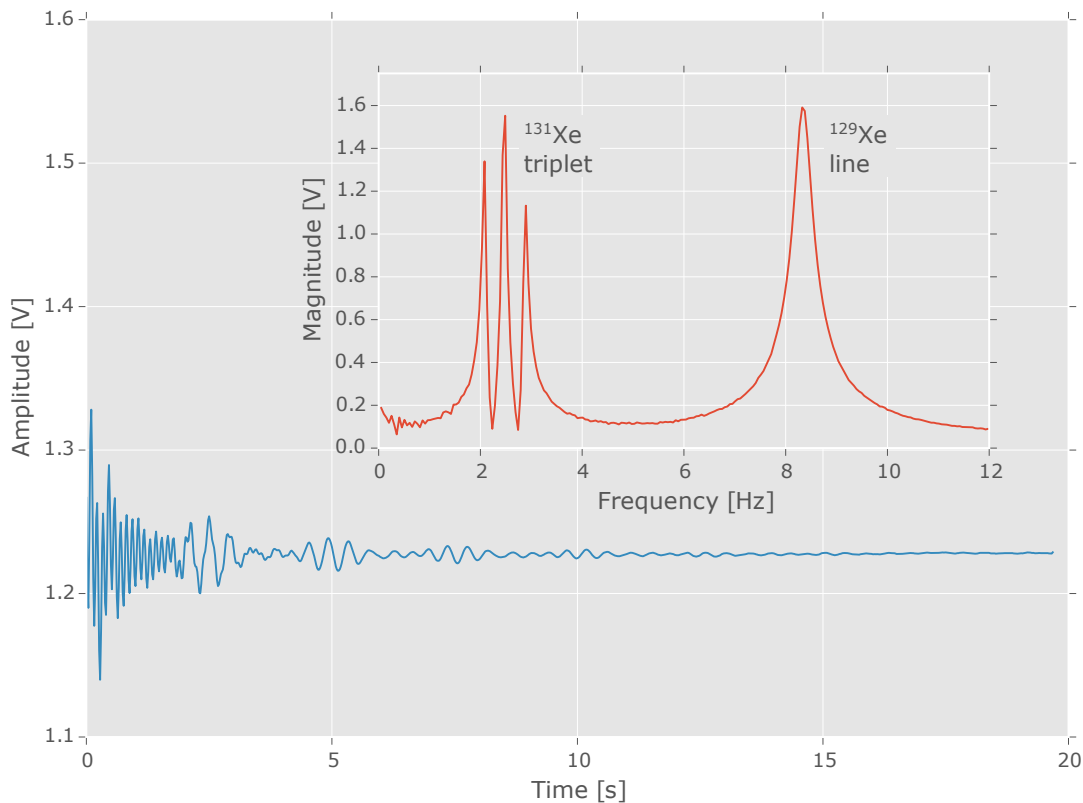
Figure 4.21: Xe NMR signal measured in a MEMS cell filled with $\approx$ 50 torr of isotopically enriched Xe (50% ^{129}Xe, 50% ^{131}Xe) and 200 torr of N_2 heated at $\approx$160°C - insert: FFT of the signal

4.5 Conclusion

A spectroscopic characterization of different MEMS atomic vapor cells was presented. First, a characterization of cells filled with natural Rb dispensing micro-pills and sealed by anodic bonding was presented. These cells contain a novel Ar-Ne buffer gas mixture as the commonly used Ar-N_2 mixture is not compatible with this filling method. An inversion temperature of 89.9°C was measured on a cell filled with 150 mbar. This value is close to the target value of 95°C. Moreover, the CPT contrast and linewidth were measured and showed properties compatible with chip-scale atomic clock applications. These two results confirm the suitability of Rb dispensing micro-pills for this application.

A second spectroscopic study was realized on MEMS cells filled with ^{87}RbN$_3$ UV decomposition and Ar buffer gas and sealed by anodic bonding. The 0-light extrapolated frequency was measured in order to extract the partial pressure of Ar and N_2 from the thermal dependence of the buffer gas frequency shift of the CPT resonance. The N_2 partial pressures was also measured by micro-Raman spectroscopy for three cells. Comparison of the results from the two methods showed a good agreement and proved the potential of Raman spectroscopy as a fast method to measure the N_2 partial pressures in order to optimize the buffer gas ratio of such cells.

A spectroscopic study was realized on evacuated MEMS cells sealed by Cu-Cu thermocompression bonding and filled with natural Rb dispensing micro-pills. In this case, a Doppler-free absorption setup was used. From the measured linewidth, a contamination of 2.1±0.2 mbar of Ar or 2.4±0.2 mbar of N_2 could be estimated.

Finally a preliminary characterization of an Al$_2$O$_3$ coated anodically bonded MEMS cell filled with ≈ 67 mbar of isotopically selected Xe (50% ^{129}Xe, 50% ^{131}Xe) and 266 mbar of N_2 was realized. The Xe free-induced decay could be measured in a dedicated setup. This measurement paves the way for future measurement of Xe T_2^* relaxation rate.

5 Analysis of RbN$_3$-filled MEMS cells lifetime

One of the critical aspects for the use of a MEMS atomic vapor cell in a commercial device is that the alkali vapor has to be maintained over the full device lifetime. In order to maintain this saturated vapor pressure of alkali, a visible amount of Rb (or Cs) has to be present at anytime inside the cell. Therefore, the initial amount of alkali present in the cell must be sufficient to compensate any consumption that could occur during the cell lifetime. Indeed, as only an extremely small amount is present in vapor phase (below 3ppm for 1mg Rb at 95°C in a 2 mm diameter cell), as soon as no liquid phase is present in the cell, if a consumption mechanism is present, the alkali vapor nearly instantaneously disappears. This is in particular the case for cells filled with alkali azide as the amount of alkali is limited by the desired amount of nitrogen buffer gas.

A study by Woetzel et al. [54] identified the consumption of alkali metal as the main failure mode of such cells filled by the UV decomposition of CsN$_3$. In this study, an Al$_2$O$_3$ coating was proposed as a solution to improve the cell lifetime by a factor of $\approx$100. Here is reported an extensive study of the lifetime of RbN$_3$ filled anodically bonded MEMS cells (see Sec. 3.3.1 and 3.4). These results were reported in [191] and [192]. First, an alkali consumption model is proposed. Then the measurement method used to estimate the amount of rubidium inside the cell is described. It is then used to measure the consumption of rubidium in accelerated aging tests. Finally, the results are discussed and a cell minimum lifetime is calculated.

5.1   Alkali consumption model

In order to estimate the cell lifetime, a consumption model is required. A comparison between coated and uncoated cells confirmed the results of Woetzel et al. [54] (see Fig. 5.1). Therefore, the following focuses on cells with Al$_2$O$_3$ coating. From observations in cells filled with low RbN$_3$ quantity it was seen that the rubidium consumption occurs in two steps: first an initial amount is consumed as the Rb is created by UV irradiation and no atomic signal can be measured by laser spectroscopy. After this initial consumption, metallic rubidium can be observed in the cell and an atomic absorption signal can be measured. This quantity nevertheless decreases over time.

The first consumption can be attributed to reaction of the rubidium with a contamination in the cell surface or volume , the second on the other hand is more difficult to determine. Two candidate were proposed in the case of uncoated cells: reduction of the sodium oxide contained in the glass or of the glass silicon dioxide by the rubidium [54] and diffusion of the rubidium in the bulk of the glass [111, 112]. In the first case, the reaction rate is constant and the consumed mass is proportional to time t. In the second case, due to diffusion laws, the consumed mass is proportional to $\sqrt{t}$. The two consumption paths remain possible for Al$_2$O$_3$ coated cells and the Rb consumption could be explained by diffusion through the membrane formed by the Al$_2$O$_3$, by an extremely slow reduction of the Al$_2$O$_3$ layer by the rubidium or by one of the two mentioned processes with the windows glass

itself through pinholes in the the Al_2O_3 layer.
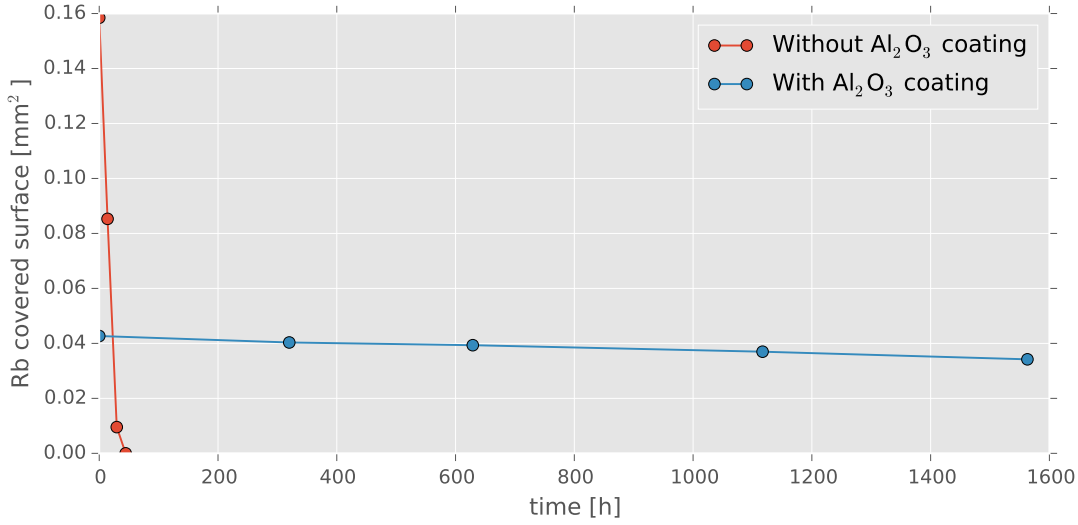
Figure 5.1: Example of the evolution of the amount of rubidium for two cells with and without Al_2O_3 coating for cells heated at 180°C. The measurement is derived from the method presented in Sec. 5.2. The surface of glass covered by metallic rubidium is presented here instead of the Rb volume as the contact angle of Rb on uncoated glass was not calibrated.

From these two possibilities, we chose to consider a consumption at a fixed rate k for the following with a consumed mass proportional to t. This is justified by the fact that no evidence of an asymptotic deviation from a linear consumption was observed in our measurements (see Fig. 5.1). Moreover, a consumption model proportional to $\sqrt{t}$ would lead to an overestimation of the cell lifetime in the case of a non-diffusive process whereas a model proportional to t would lead to a less critical underestimation of the lifetime in the case of a reaction driven process. In this case, the total amount of rubidium at a time t during the cell lifetime writes as:

$$m_{meas.}(t) = m_{prod.} - m_{init.\ cons.} - k \cdot t \tag{5.1}$$

where $m_{prod.}$ is the amount of Rb produced by the UV decomposition of RbN_3, $m_{init.\ cons.}$ is the mass of the initial consumption of Rb.

5.2   Measurement of metallic rubidium amount

The two consumptions steps are measured by an image analysis method. The metallic rubidium in the cells is migrated on the cell window by mean of a thermal gradient (see Fig. 5.2 - left). A microscope image of the droplets is then taken on inner the surface of the cell window. The droplets radius a are measured using an image recognition software (see Fig. 5.2 - right). Figure 5.3 illustrate the evolution of the droplets size over time. A comparable imaging techniques were used by Zhao and Wu in [193] however no image recognition software and no thermal gradient were used.

The droplet volume can be estimated as the volume of a spherical cap from the diameter, with an unknown contact angle θ (see Fig. 5.4). That last parameter depends on the wettability of the
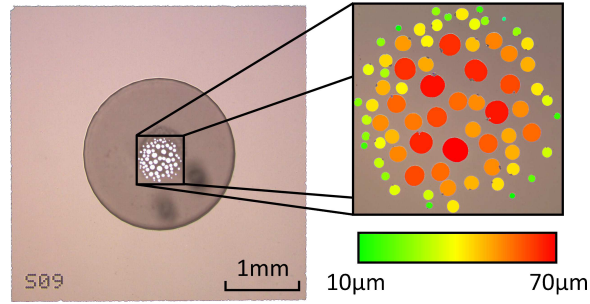
Figure 5.2: Image recognition of Rb droplets size in MEMS atomic vapor cell: [left] Microscope image of a cell - [right] Extraction of drop radius by image recognition software - **Microscope image: courtesy of Jean Gobet, CSEM - Copyright © 2017 Optical Society of America. Reprint by permission of Optical Society of America.**

| start | 276h | 506h | 1352h | 2013h | 2924h | 4851h |

Figure 5.3: Example of the droplets evolution over time for a cell heated at 196°C. Small black dots can be observed on each drop. These particles of unknown composition are likely the nucleation sites of the droplets. - **Microscope image: courtesy of Jean Gobet, CSEM - Copyright © 2017 Optical Society of America. Reprint by permission of Optical Society of America.**

rubidium on the Al_2O_3 coating and must be measured (see Sec. 5.3) :

$$V = \frac{\pi h}{6}(3a^2 + h^2) \tag{5.2}$$

with $h = a\tan(\theta/2)$.
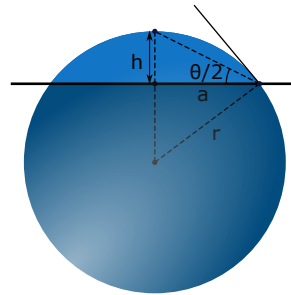
Figure 5.4: Spherical cap model used for Rb drop volume estimation

5.3 Calibration of droplets volume and measurement of the initial consumption

The contact angle, and the initial consumption ($m_{init.cons.}$) are estimated at the same time. The image recognition method is combined with N_2 partial pressure measurements realized by micro-Raman spectroscopy (see Sec. 4.2). A batch of cells was filled with different natural RbN_3 quantities and UV decomposed. They are then measured with the two methods. As N_2 and Rb are stoichiometrically

linked, the measure of the N_2 pressure gives the produced amount of rubidium. For cells filled with the smallest quantities of RbN_3, a small N_2 pressure was measured but no metallic Rb imaged. This indicates that an initial metallic Rb consumption occurs. The observed Rb mass $m_{meas.}$ can then be written as:

$$m_{meas.} = \begin{cases} m_{prod.} - m_{init.\ cons.} & \text{if } m_{prod.} > m_{init.\ cons.} \\ 0 & \text{if } m_{prod.} < m_{init.\ cons.} \end{cases} \tag{5.3}$$

where $m_{prod.}$ is the the produced Rb mass calculated from the N_2 measurement. Using Eq. 5.2 to calculate the measured mass ($m_{meas.}$) and Eq. 5.3, the contact angle θ can be adjusted such that the slope between $m_{meas.}$ and $m_{prod.}$ is 1 for non-0 values of $m_{meas.}$ (see Fig. 5.5). A values of $\theta = 57 \pm 6°$ was found from this optimization and the initial consumption is therefore $m_{init.\ cons.} = 0.50 \pm 0.08 \ \mu$g.
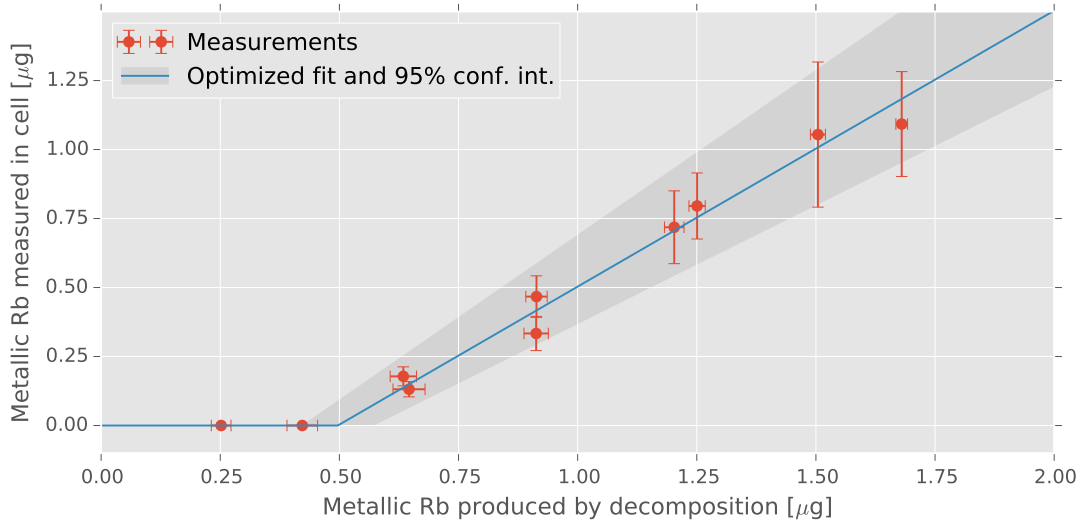
Figure 5.5: Estimation of Rb initial consumption: The contact angle θ is adapted such that the slope is 1 for the non-0 values of the measured Rb quantity

5.4   Cell lifetime estimation

We suppose that the rubidium consumption rate is temperature dependent following an Arrhenius equation:

$$k = Ae^{\frac{-E_a}{RT}} \tag{5.4}$$

where k is the Rb consumption rate, A the prefactor with the same unit as k, R is the ideal gas constant in [J mol^{-1} K^{-1}], T the temperature in [K] and E_a the activation energy in [J mol^{-1}].

Three batches of 4 to 6 cells from the same wafer were placed in a thermoregulated oven at different temperatures (171, 180, and 196°C) for up to 7 months. Image recognition was used to monitor the droplets radius over time and the rubidium quantity was calculated with the determined contact angle θ to extract the cell lifetime. The metallic rubidium in the cells was migrated on the cell window by mean of a thermal gradient prior to each measurement. The remaining amount of rubidium in the cells was measured at regular intervals and the average consumption rates k_i were extracted by linear fitting for each cell. They are displayed in an Arrhenius graph in Fig. 5.6. A linear

fit was then realized on the k_i values in order to extract the activation energy. An experimental value of $E_a = 60 \pm 24$ kJ/mol was found.
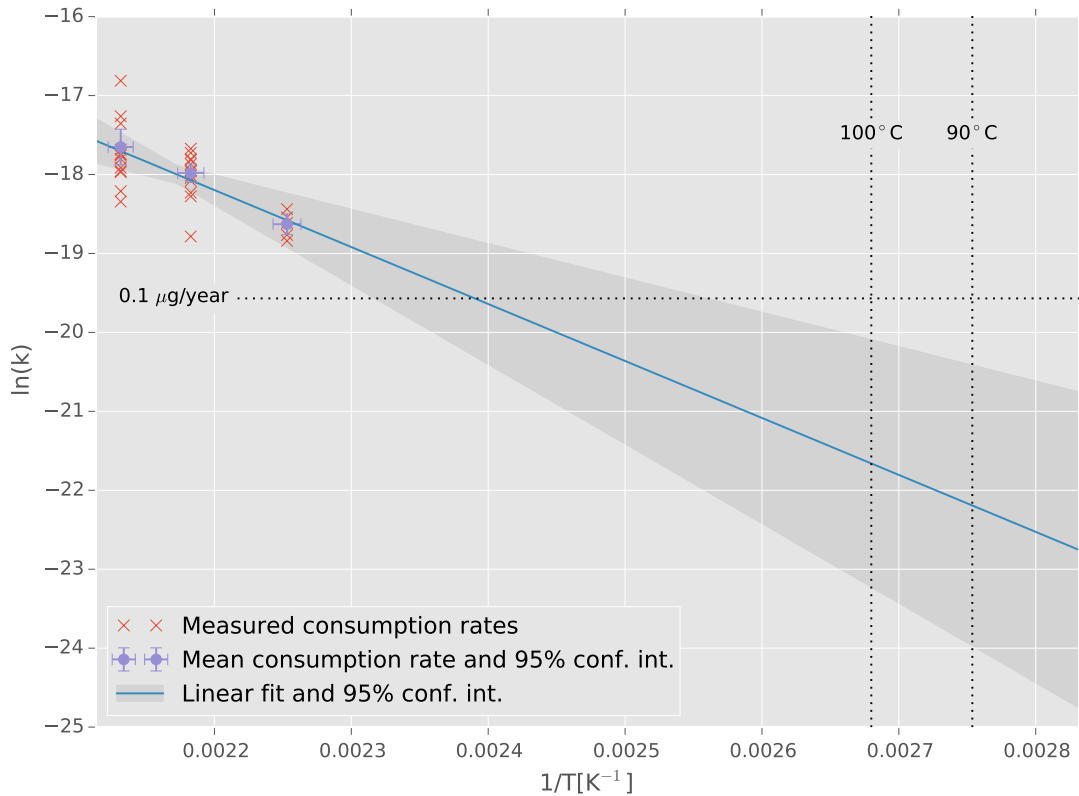
Figure 5.6: Estimation of the activation energy by fitting of the rubidium consumption rates of cells at different temperatures (k is given here in μg/s)

For a desired lifetime of 10 years at 95°C, a minimal required rubidium quantity of $0.60^{+0.59}_{-0.10}$ μg at t_0 can be calculated from Eq. 5.1 and 5.4. This quantity corresponds to the creation of 83^{+81}_{-14} mbar N_2 by the RbN$_3$ UV-decomposition. In order to suppress the first order dependence of the cell frequency to the temperature at 95°C, an Ar backfilling pressure of 108^{+105}_{-18} mbar is required (see Sec. 2.5.3.1) which gives a total buffer gas pressure of 191^{+186}_{-32} mbar.

This pressure is above the value typically used in rubidium MEMS cells. However, as the limiting factor for the total buffer gas pressure is the overlapping between the optical absorption lines. (see Sec. 2.5.4.2) This is particularly the case for cells filled with natural rubidium where the two isotopes absorption lines overlap. However, in the case of cells filled with isotropically selected ^{87}Rb, the absorption lines are separated by ≈ 6.835 GHz which allows for a larger buffer gas pressure before overlapping occurs.

5.5 Conclusion

The lifetime assessment of MEMS atomic vapor cells filled with RbN$_3$ UV-decomposition and with an Al$_2$O$_3$ coating was realized. A novel method based on image analysis was developed in order to measure the amount of metallic Rb inside the cell cavity. It is based on the condensation of the

Rb droplets on a cell window and on the estimation of the formed spherical caps radius by image analysis. The contact angle between the Rb droplet and the Al_2O_3 coated window being calibrated by Raman spectroscopy of the buffer gas pressure created by the RbN_3 decomposition, the total amount of Rb could be monitored in accelerated aging test. An activation of 60 ± 24 kJ/mol was found which corresponds to a quantity of $0.60^{+0.59}_{-0.10}$ μg of metallic rubidium for a desired lifetime of 10 years at 95°C. This quantity corresponds to a total buffer gas pressure of 191^{+186}_{-32} mbar in the case of Ar backfilling. For ^{87}Rb this pressure is potentially compatible with CSAC application, showing the potential of RbN_3 filled, Al_2O_3 coated cells in actual devices.

6 Clock measurement of long-term stability

This chapter describes the long-term frequency stability measurement realized on MEMS atomic vapor cells. As explained in Chap. 2, the long-term stability of a clock mainly relies on the stability of physical parameters that shift the frequency of CPT resonance, *i.e.* the light shift, the buffer gas shift and the second order Zeeman effect. In this chapter, a specific setup dedicated to long-term frequency measurement in clock operation is described and used to monitor these parameters over extended time periods. In particular, a characterization of two different cells is presented: the setup is first used to evidence that the main source of long-term frequency instability is the migration of alkali droplets on the cell window and the induced change of the power light-shift. This is realized by measuring an $^{87}RbN_3$-filled anodically bonded MEMS cell with Al_2O_3 coating. The setup is then used to show the effect of the CSEM patent pending Au micro-disc described in Chap. 3 on this issue and on the clock long-term frequency stability. In particular it is proven that this technology allows to circumvent the droplets migration limitation. This second measurement is realized on an anodically bonded MEMS cell with Al_2O_3 coating filled by dispensing micro-pill which fabrication is described in Sec. 3.5.

6.1 Clock setup

6.1.1 Description of the setup

The setup described here is designed such that it allows for the long term characterization of MEMS atomic vapor cells in clock operation. In order to control the stability of the experimental condition, a monitoring of the relevant experimental parameters is implemented (see Fig. 6.1). The C-field current, the cell temperature, the laser power and the RF power are therefore measured and recorded during the experiment. The full setup is moreover placed in a room with stable temperature and the relevant parts of the experience (*i.e.* the cell in its magnetic shielding and the laser) are placed in a thermally insulated box.

The experimental setup is presented in Fig. 6.2. An Oclaro 795 nm Single mode VCSEL is thermally controlled at a temperature T_{Laser}. An injection current I_{Laser} and a RF modulation at a power P_{RF} can be applied to the laser. The laser beam is sent through a beam splitter to a powermeter (Thorlabs S130C) in order to monitor the laser power sent to the rest of the setup. The beam crosses a neutral density filter and a "$\lambda/2$ - polarized beam splitter system" whose function is to tune the optical power and to precisely control the polarization. The remaining power of the beam crosses a $\lambda/4$ wave-plate in order to apply a σ-polarization to the cell under test placed right after. The cell under test is temperature controlled and placed in a double magnetic shielding. The C-field is applied by a solenoid. Finally, the absorption signal is detected by a photodiode.

In operation, the setup is controlled by laboratory electronics: The laser temperature is controlled
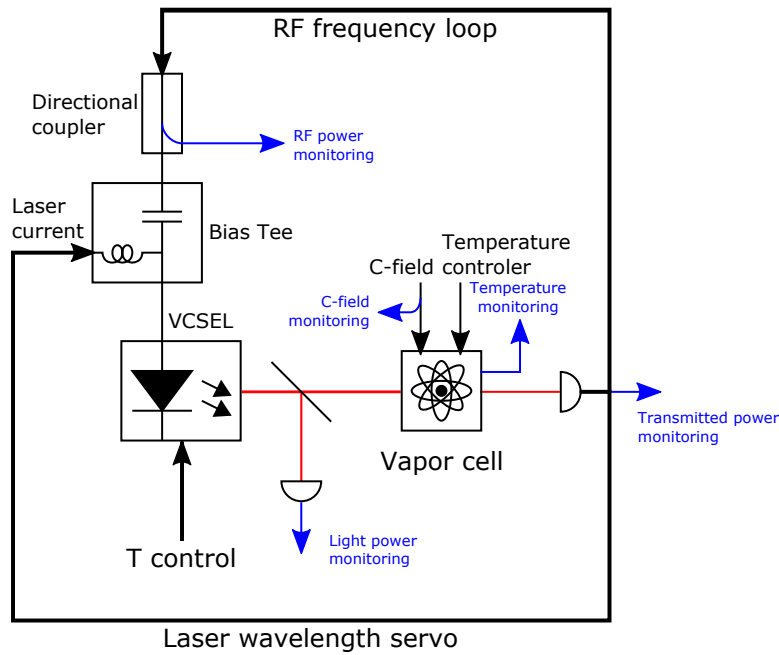
Figure 6.1: Schematic view of the long-term measurement setup: laser power and frequency servo loops and parameters monitoring
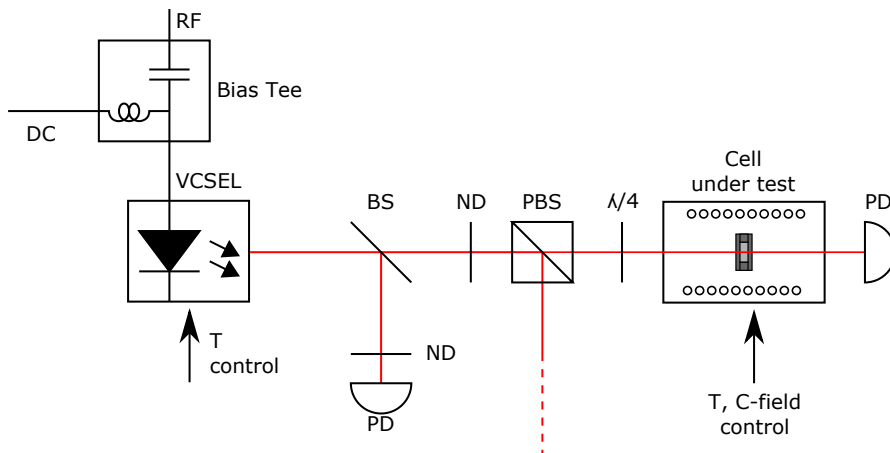
Figure 6.2: Schematic view of the physical implementation of the long-term measurement setup

using a numerical controller (SRS PTC10) and an NTC. The laser frequency is controlled by a laser locking system (TEM LaseLock) which drives a laboratory current source. It is locked on an absorption line of the cell under test by modulation of the laser current at 50kHz and synchronous detection. The laser RF modulation is applied through a bias-tee (Mini-circuit ZFBT-6GW+) with a RF generator (SRS SG384). This generator is frequency referenced to an OCXO (Oscilloquartz OCXO 8788). The modulation of the RF frequency, which can be fixed at any frequency $f_{\text{Mod.}}$ and depth $\Delta\nu_{\text{RF}}$, is synchronously detected using a lock-in amplifier (SRS SR 850). The resulting error signal is used to control the OCXO through a PID system (SRS SIM960). Finally, the cell under test is temperature controlled using a numerical controller (SRS PTC10) and an NTC. The C-field current is delivered by a laboratory current source.

6.1.2 Laser head characterization

This section presents a detailed characterization of the VCSEL laser head of the long-term clock setup for use with the ^{87}Rb D1 line (*i.e.* RF modulation at $\approx$3.417GHz, half the hyperfine frequency). The resonance temperature, the side-mode suppression ratio, the linewidth, the beam width, the polarization as well as the RF modulation capabilities are investigated. From these study, the optimal working-point of the laser were determined to be 1.7mA injection current at 70°C with a RF power of 3dBm at the output of the synthesizer. The exact power coupled to the laser diode was however not measured. A similar study (partial) was realized with a modulation frequency at $\approx$3.035GHz for use of the ^{85}Rb D1 line in natural Rb. From this study, which is not presented here, the optimal RF power was found to be 0dBm for the laser RF modulation power.

6.1.2.1 Measurement setup

The measurement setup used to characterize the VCSEL is presented in figure 6.3. Two different instruments are used in order to make a frequency characterization of the laser. An optical spectrum analyzer (OSA) (Ando AQ6317B) allowing a wavelength resolution of 0.05 nm and a Fabry-Pérot interferometer (Toptica DL100) with a free spectral range (FSR) of 1GHz and a typical finesse above 400 are used.

These two instruments are complementary as the OSA allows for an absolute measurement of the wavelength with a high dynamic range while the Fabry-Pérot interferometer allows for a precise relative wavelength measurement.
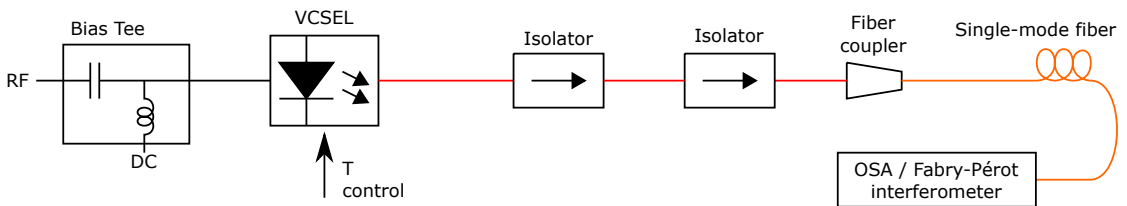
Figure 6.3: Fabry-Pérot and Optical spectrum analyzer setup

6.1.2.2 Resonance temperature

As the final goal is to use the VCSEL as a laser source for CPT experiment on the D1 line of ^{87}Rb, the laser temperature necessary to reach the resonant frequency was measured as a function of the laser injection current and is presented in Fig. 6.4. Resonant temperature are found to be in the 60 to 75°C range for an injection current in the 1 to 3 mA.

6.1.2.3 Side-mode suppression ratio

The side mode suppression ratio (SMSR) was measured as a function of the laser injection current and temperature using the OSA setup presented above. An example of a typical observed spectrum is presented in Fig. 6.5. No dependence on the temperature was observed. However, an important dependence on the laser injection current was observed and is presented in Fig. 6.6. Typical values expected for the use of such VCSEL for CPT atomic clock experiments are in the order of 40 dB [194] which is reached in a range from 1.2 to 1.7 mA injection current. Therefore, as a first approximation, the working current I_{Laser} was set at 1.7 mA which corresponds to a resonance temperature of approximately $T_{\mathrm{Laser}} \approx 70°C$. This temperature is chosen such that the SMSR remains sufficiently low but the output power remains sufficiently important to realize further CPT experiments in a wide light intensity range.
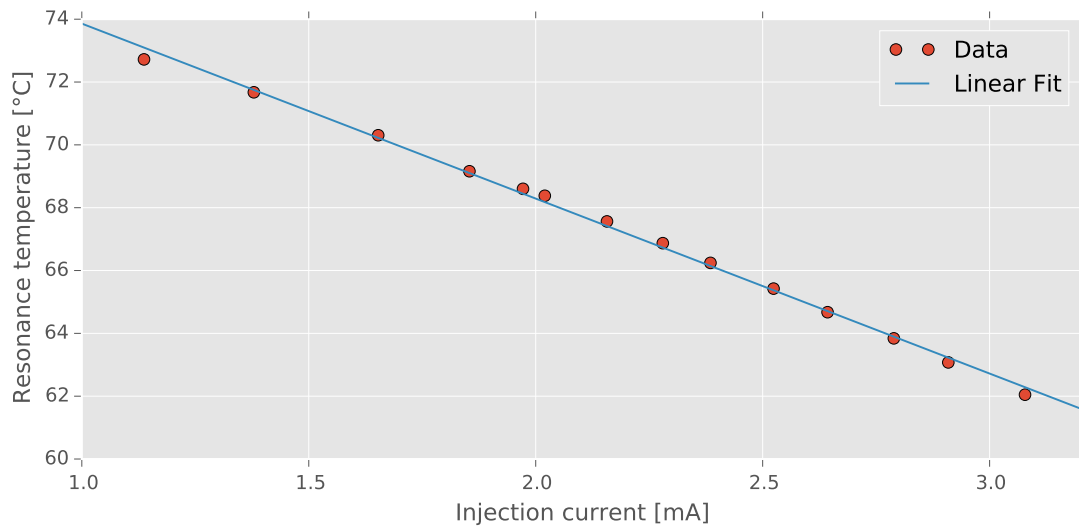
Figure 6.4: Laser temperature necessary to reach the ^{87}Rb D1 line as a function of the laser injection current for the long-term setup laser. The fitted parameters are: $T[°\text{C}]=79.43-5.57\cdot I[\text{mA}]$
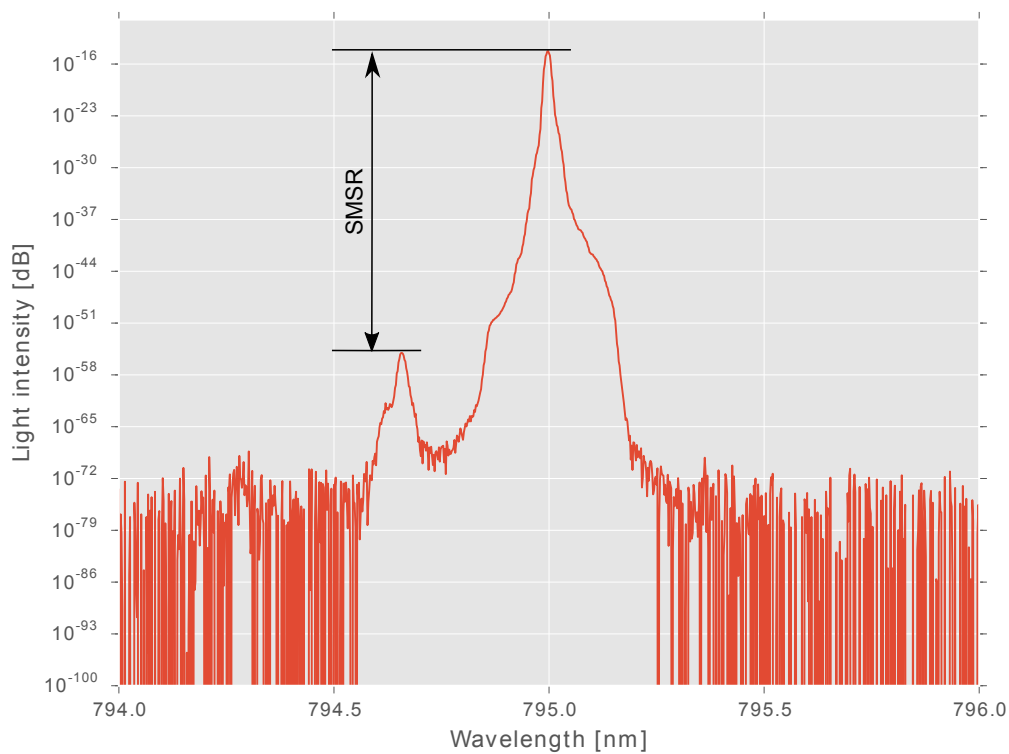
Figure 6.5: Laser spectrum and SMSR definition. $I_{\text{Laser}}=1.7\text{mA}$, $T_{\text{Laser}}=70°C$
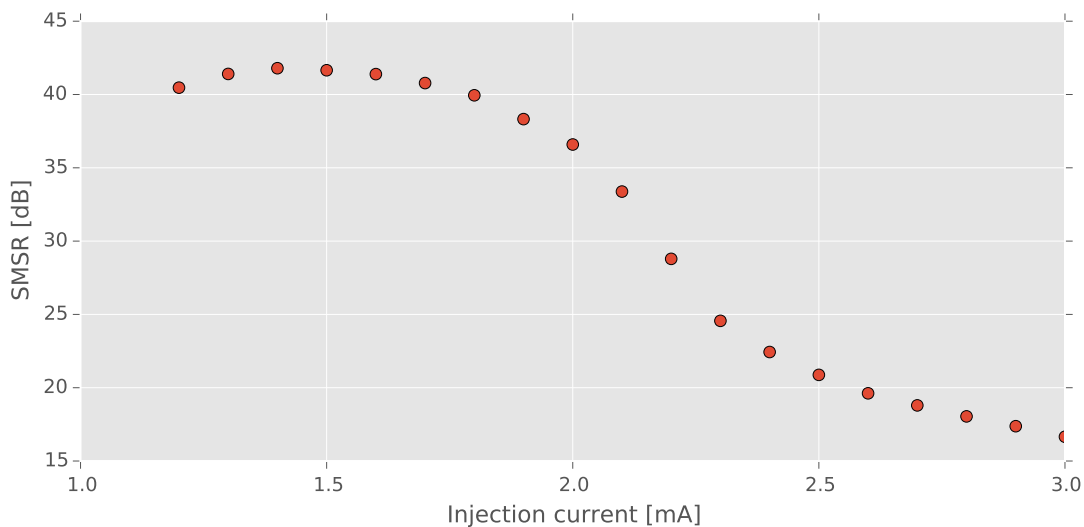
Figure 6.6: SMSR dependency to the laser injection current for the long-term setup laser

6.1.2.4 Laser frequency linewidth

The laser linewidth is a relevant parameter for two reasons: It defines the optical spectral resolution and whether or not it is possible to resolve sub-Doppler peaks [195] and it plays a role in the AM to FM conversion of the laser phase noise [89]. A shorter linewidth therefore allows to obtain a better clock short term frequency stability. A Lorentzian fit was realized on the Fabry-Pérot interferometer data and a FWHM in the order of 38 MHz was measured (see Fig. 6.7).

6.1.2.5 Laser beam size

The laser beam width and shape is an important parameter in a CPT experiment as it dictates the light distribution inside the vapor cell. A wide beam allows to reduce the contribution of the time-of-flight broadening (or transit time broadening) to the spectral width of the resonance [29]. Moreover, it is a necessary parameter to calculate the light intensity from the measured light power of the laser. In the current experiment, the laser beam was measured to be Gaussian at the cell position with a FWHM of 673 μm in the horizontal direction and 573 μm in the vertical direction (see Fig. 6.8). These measurements were realized with a beam profiler (Thorlabs BP109-VIS).

6.1.2.6 Polarization

A precise control of the laser polarization is required in a CPT experiment in order to address the desired transitions. In the setup presented above, the laser polarization is controlled after the laser source by a polarized beam splitter. The laser polarization extinction ratio (PER) was therefore not measured. Moreover, no evidence of laser polarization jumps were observed over time.

6.1.2.7 Laser intensity

The dependance of the laser power to the laser injection current and temperature was analyzed. The results are presented on Figures 6.9 and 6.10. A dependance of 257.8 μW/mA to the injection current and of -3.164 μW/K to the temperature was measured around the laser working point.
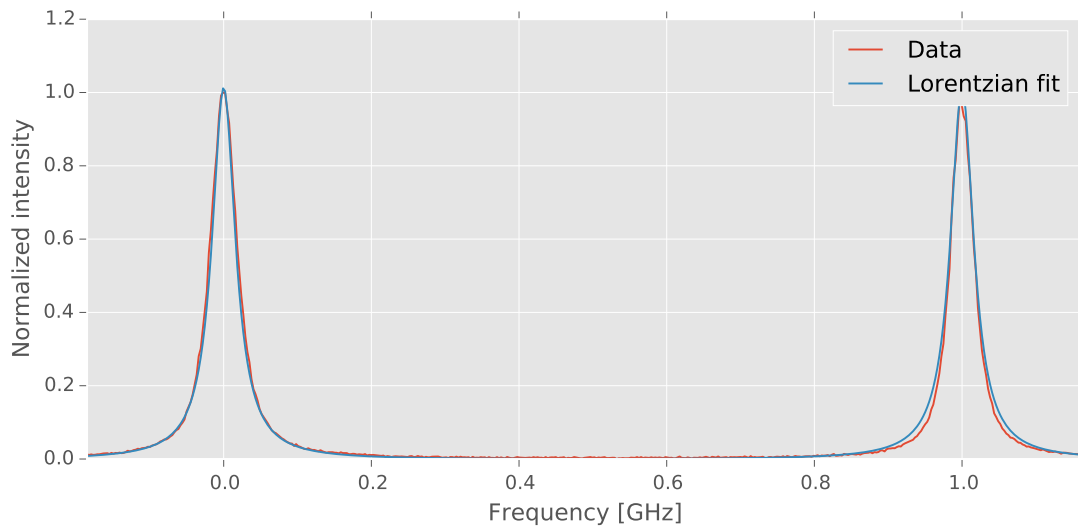
Figure 6.7: Laser linewidth measurement: data from the Fabry-Pérot interferometer and Lorentzian fit.
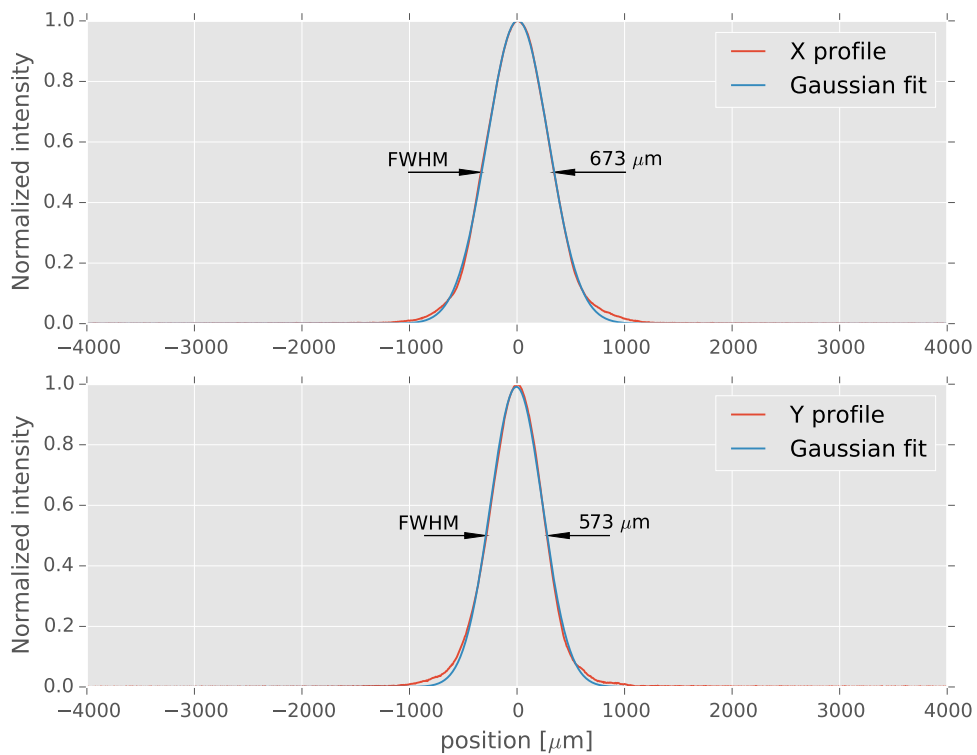
Figure 6.8: Laser beam profiles at cell position for the long-term setup laser with $T_{\mathrm{Laser}} = 70°C$, $I_{\mathrm{Laser}} = 1.7$ mA
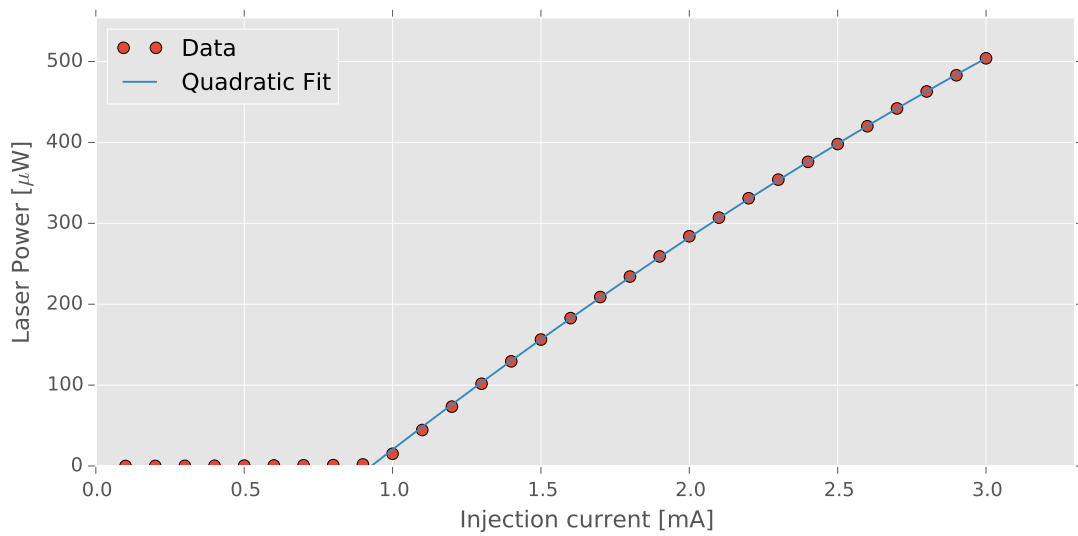
Figure 6.9: Laser power dependance to the injection current for the long-term setup laser with $T_{\mathrm{Laser}} = 70°\mathrm{C}$

Figure 6.10: Laser power dependance to the temperature for the long-term setup laser with $I_{\mathrm{Laser}} = 1.7$ mA

6.1.2.8 Laser frequency

The dependance of the laser frequency to the laser injection current and temperature was analyzed. The results are presented on Figures 6.11 and 6.12. A dependance of 0.261 nm/mA (124 GHz/mA) to the injection current and of 0.0531 nm/K (25.2 GHz/K) to the temperature was measured around the laser working point of $I_{\mathrm{Laser}} = 1.7$ mA, $T_{\mathrm{Laser}} = 70°$C.
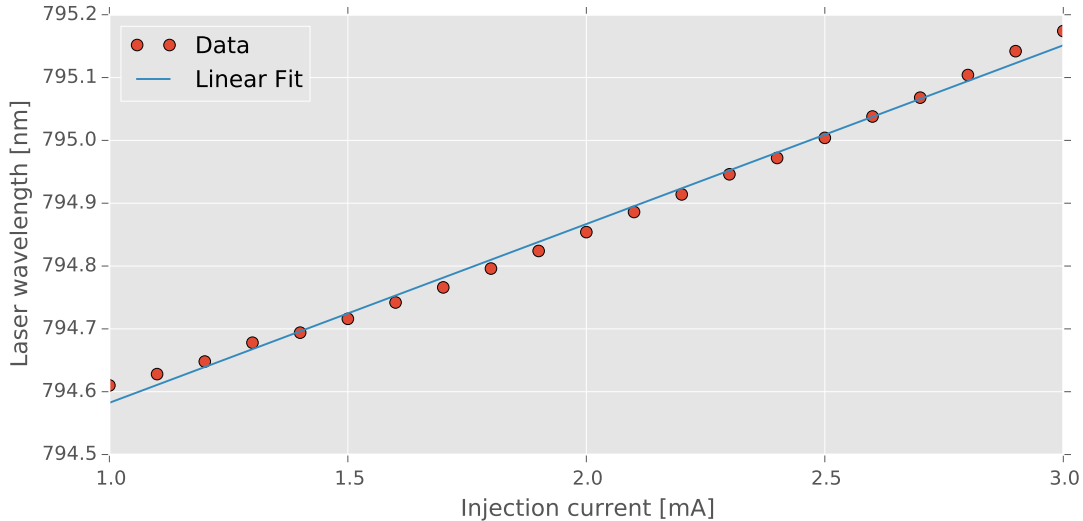
Figure 6.11: Laser wavelength dependance to the injection current for the long-term setup laser with $T_{\mathrm{Laser}} = 70°$C

6.1.2.9 Laser RF modulation

When used with ^{87}Rb, the VCSEL is RF modulated at a frequency of approximately 3.417 GHz. As an effect, this creates sidebands which are brought in resonance with the absorption lines and create the dual-frequency field required by the CPT interrogation. However, in the case considered here, only the two first sidebands (m=+1 and m=-1) contribute to the signal. It is therefore necessary to find the optimal modulation condition such that a maximum of the laser power is placed into these two bands. In the following, the relative sideband intensity will be measured as a function of the modulation power, the laser temperature and the laser injection current.

Injected RF power dependency The relative intensity of the sidebands and of the carrier were analyzed as a function of the RF power by fitting of the signal obtained by the Fabry-Pérot interferometer. The RF power is measured at the output of the RF generator. The results are presented on Figure 6.13 for $I_{\mathrm{Laser}} = 1.7$ mA, $T_{\mathrm{Laser}} = 70°$C. One can see that the behavior of the two first sidebands is not completely symmetrical. The m-1 sideband presents a maximum at approximately 4 dBm whereas the m=+1 sideband presents a maximum at 5 dBm. The two sidebands have however approximately the same intensity at 3 dBm. Therefore this intensity was chosen for the next experiments.

Laser injection current dependency The relative intensity of the sidebands and of the carrier were analyzed as a function of the laser injection current with $T_{\mathrm{Laser}} = 70°$C, $P_{\mathrm{RF}} = 3$ dBm and is presented in Fig. 6.14. The relative power in the m=+1 and m=-1 sidebands shows a maximum for
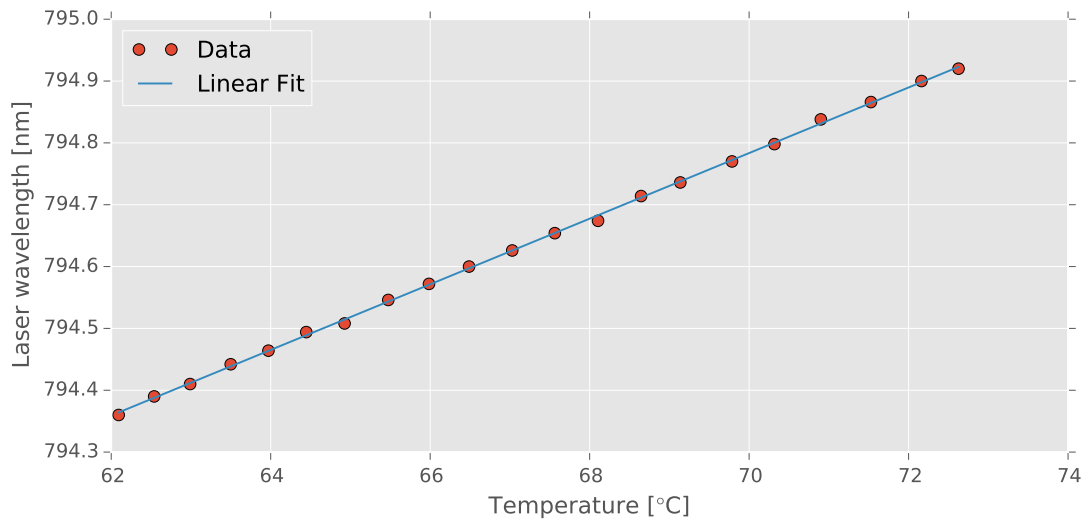
Figure 6.12: Laser wavelength dependance to the temperature for the long-term setup laser with $I_{\text{Laser}} = 1.7\text{mA}$
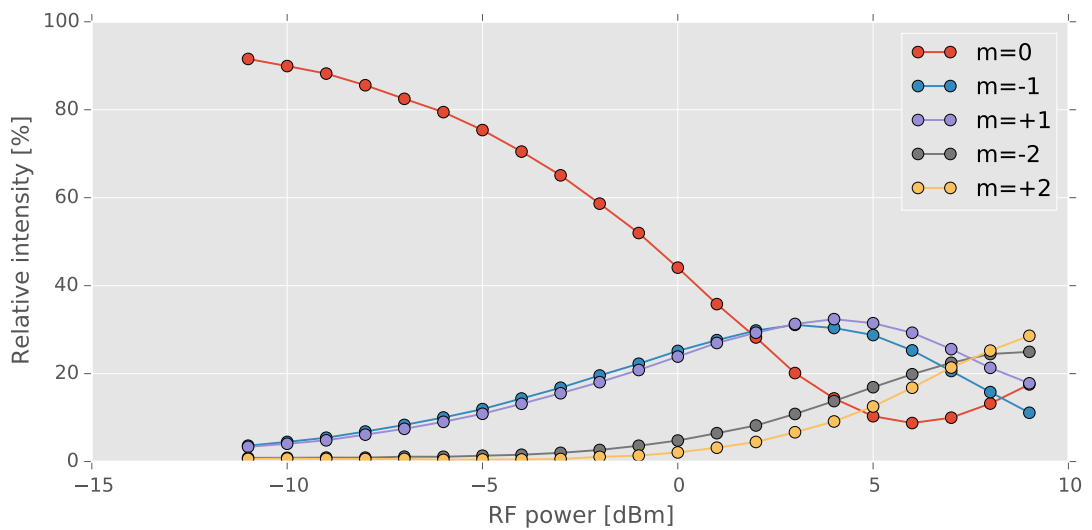
Figure 6.13: Dependance of the Laser sidebands intensity to the injected RF power for the long-term setup laser with $I_{\text{Laser}} = 1.7$ mA, $T_{\text{Laser}} = 70°\text{C}$

a laser injection current in the order of 1.6 to 1.7 mA. As the RF power of 3 dBm was fixed slightly below the optimal power for the injection current of 1.7 mA, this results is consistent with the fact that the RF power optimizing the relative intensity in the first sidebands depends on the injection current and increases with it.
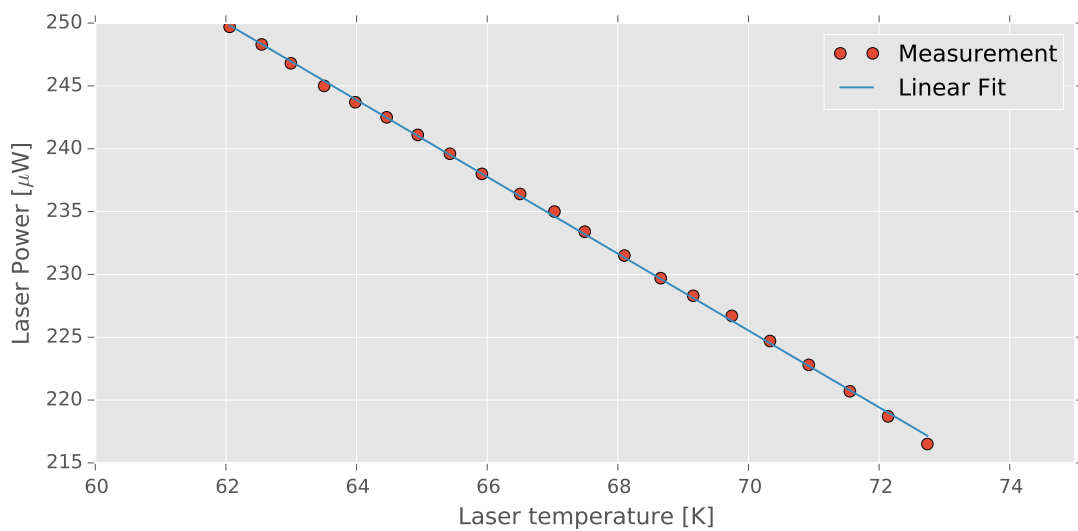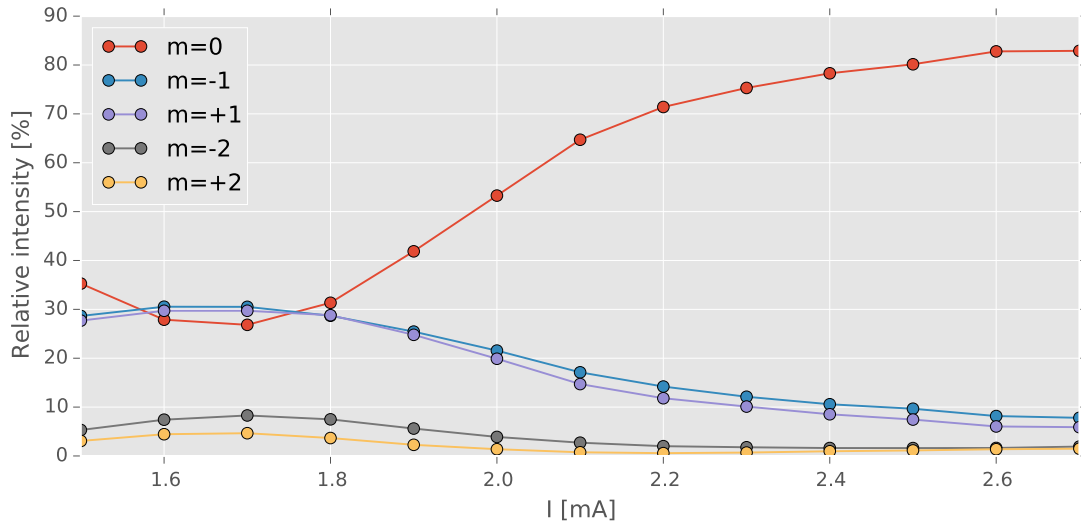

Figure 6.14: Dependance of the Laser sidebands intensity to the injection current for the long-term setup laser with $T_{\text{Laser}} = 70°\text{C}$, $P_{\text{RF}} = 3$ dBm

Laser temperature dependency The relative intensity of the sidebands and of the carrier were analyzed as a function of the laser temperature with with $I_{\text{Laser}} = 1.7$ mA, $P_{\text{RF}} = 3$ dBm and is presented in Fig. 6.15. In a first approximation, the laser temperature does not influence the RF modulation of the cell.
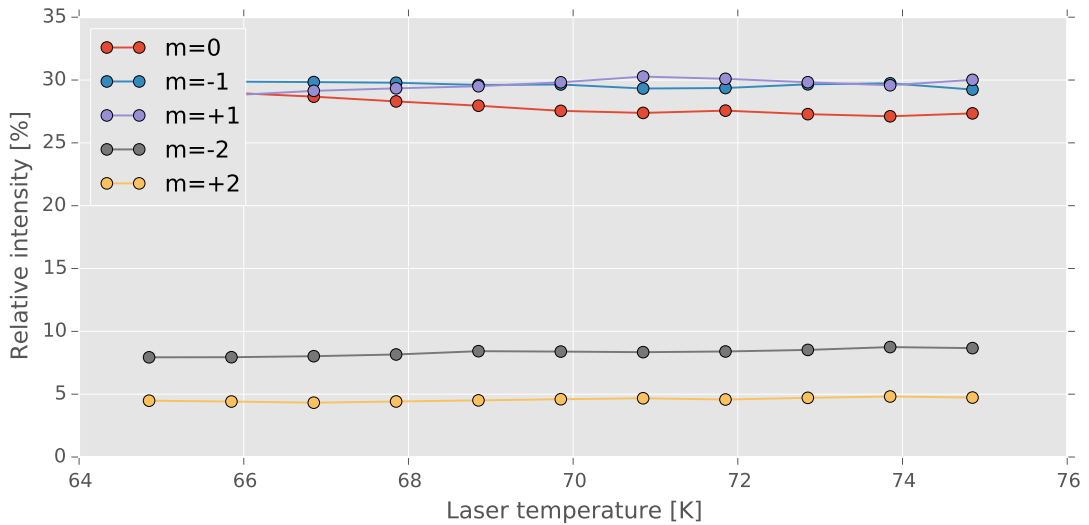
Figure 6.15: Dependance of the Laser sidebands intensity to the temperature for the long-term setup laser with $I_{\mathrm{Laser}} = 1.7$ mA, $P_{\mathrm{RF}} = 3$ dBm

6.2 Long term measurement on cells with and without gold micro-discs

Long-term frequency measurement are realized on MEMS atomic vapor cells with Al_2O_3 coating filled with $^{87}RbN_3$ and sealed by anodic bonding. The goal was to evidence the dominant source of clock instability. The relevant clock parameters were recorded during the measurement using the setup presented above. The effect of each parameter was extrapolated in term of clock frequency stability. The dominant instability parameter was determined to be the change of laser light transmission through the cell and its influence on the frequency through the power light-shift. This change in transmission was attributed to migration of Rb droplets on the cell window. A solution to limit this effect was proposed with the CSEM patent pending gold micro-discs which concentrate the rubidium at the desired spots. The effect of these microstructures on the cell clock long-term frequency stability is investigated in the following.

6.2.1 Evidence of instabilities due to Rb droplets migration

A measurement on a MEMS atomic vapor cells filled with $^{87}RbN_3$ and sealed by anodic bonding without Au micro-discs was first realized in order to evidence the dominant frequency instability parameter for the long-term. The influence of the clock parameters on the clock frequency were first measured. The clock frequency was then measured over a long period along with the different clock parameters and the corresponding Allan variances were computed and their effects on the clock stability extracted.

6.2.1.1 Experimental conditions

The laser temperature is fixed at 70°C and the injection current is adjusted such that it is resonant with the D1 line of Rb, *i.e.* ≈1.7 mA which correspond to the optimal experimental parameters determined above. The RF frequency is tuned to the center of the CPT line. It is modulated at an arbitrary frequency $f_{\mathrm{Mod.}}$=345 Hz and depth $\Delta\nu_{\mathrm{RF}} = 2 \cdot f_{\mathrm{Mod.}}$=690 Hz. The RF power is fixed at

3 dBm. The cell temperature is fixed at 95°C. The C-field is fixed at a value of $\approx$300 mG. Finally the input laser power is fixed at 15 μW, close to the optimal power determined in Sec. 4.1.7.

6.2.1.2 Measurement of clock parameters

In order to compute the influence of the parameters that impact the long term frequency stability of the clock, the frequency dependency of each of them was recorded. That is to say the dependence of the clock frequency to the cell temperature, RF power, optical intensity and C-field intensity. They were measured by varying the target values around the clock operating point and recording the clock frequency. The frequency dependance to the different parameters is presented in Tab. 6.1. The optical light shift coefficient is computed in term of light intensity from the measured input power and the measured laser Gaussian beam width as the σ-radius mean intensity as follow:

$$\alpha_{LS}[\text{cm}^2\mu\text{W}^{-1}] = \alpha_{LS}[\mu\text{W}^{-1}] \cdot \pi \cdot (2.35 \cdot FWHM[\text{cm}])^2 \tag{6.1}$$

where $FWHM = 2\sigma\sqrt{2\ln(2)} \approx 2.35\sigma$ is the mean value between the X and Y measured FWHM (see Sec. 6.1.2.5).

Clock parameter	Frequency dependence
Cell temperature shift	$1.93 \cdot 10^{-9}$/°C
RF power	$-1.08 \cdot 10^{-8}$ /dB
Intensity light shift	$7.88 \cdot 10^{-9}$/μW ($1.74 \cdot 10^{-11}$ cm^2/μW)
C-field intensity shift	$5.16 \cdot 10^{-8}$/mG

Table 6.1: Clock frequency dependance to parameters for a MEMS atomic vapor cells filled with ^{87}RbN$_3$ and sealed by anodic bonding

The dependence of the clock frequency to the laser light frequency was nevertheless not measured as it is referenced (locked) to the cell itself. Indeed, in-loop measurement are more difficult to realize as the frequency must be compared to another more stable reference. The order of magnitude of the relative clock frequency instabilities due to the frequency light shift was nevertheless estimated to be in the order of $2.92 \cdot 10^{-12}$. Indeed, this value can be extrapolated taking a relative laser frequency stability in the order of 10^{-9} as estimated in [196], for a VCSEL locked on a Doppler-broadened Rb D1 absorption line without buffer gas above 1000 s integration time, and a β_{LS} in the order of 20 mHz/MHz as measured in [98] for Cs D1 line. In the present case, the relative laser frequency stability in extrapolated to be in the order of $4 \cdot 10^{-9}$ because of the $\approx$1.7 GHz excess optical broadening due to the 100 mbar Ar-N$_2$ buffer gas mixture (See Eq. 2.68) and its effect on the laser lock discrimination slope.

A few comments can be made on the measured coefficients. First the intensity light shift coefficient α_{LS} is superior to the typical relative frequency shift value of 10^{-12}cm^2/μW cited, for example, in [197]. However, it is in the same order of magnitude as the coefficient measured by Ermak et al.[27] in MEMS cells filled with 200 to 400 mbar Ne as buffer gas which value is between $1.5 \cdot 10^{-12}$ and 1.510^{-11}cm^2/μW. The RF power coefficient, on the other hand, is in the same order of magnitude as the coefficient measured by Lutwak et al. in [6]. The cell temperature shift coefficient corresponds to the value measured on a similar natural RbN$_3$ filled cell with 0-light extrapolation in Sec. 4.1.2.2. Finally, the C-field intensity shift coefficient corresponds to the 2$^{\text{nd}}$ order Zeeman shift derivative for a C-field intensity of $\approx$300 mG.

6.2.1.3 Long term clock measurement

The clock frequency of the clock was recorded over a long period (>15 days) along with the relevant clock parameters. From these data, the Allan variance of the clock as well as the influence of each parameters on the clock frequency stability were computed. They are presented on Fig. 6.17. The $\tau^{-1/2}$ noise behavior goes only up to ≈100 s averaging time from the $7.3 \cdot 10^{-11}$ 1 s averaging time value. After this, a large deviation is measured and the Allan variance crosses the 10^{-10} limit at 10'000 s averaging time.
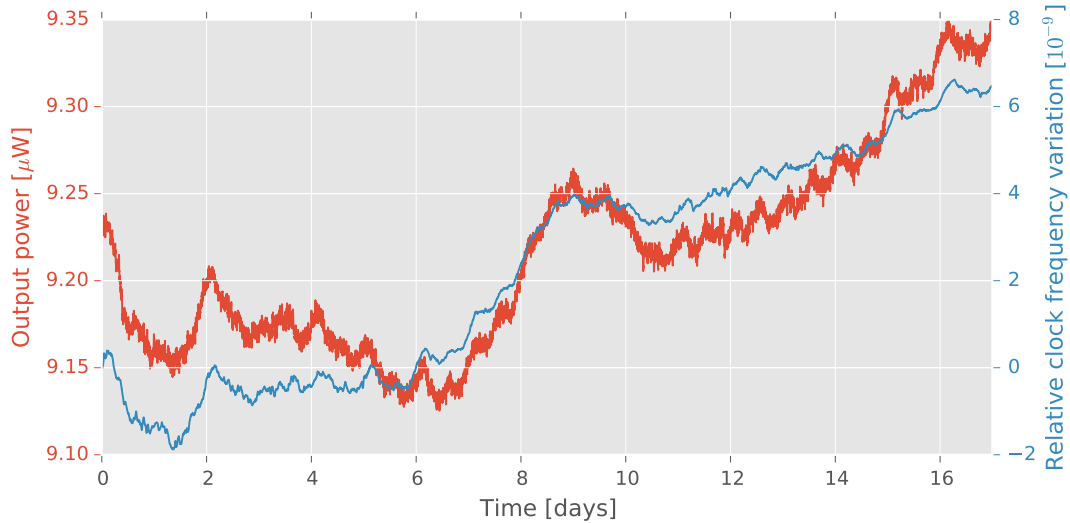
Figure 6.16: Comparison between the output power and the relative clock frequency for the MEMS cell without Au micro-disc

6.2.1.4 Discussion of the observations

The poor long term frequency stability cannot be explained by the variation of the clock input parameters (*i.e.* the cell temperature, the RF power, the input optical intensity or the C-field intensity). However, a variation of the light intensity inside the cell due to change in transmission of the cell input window and the induced power light shift are not taken into account in that estimation. However, as change in the input window transmission directly influence the cell output power, by recording this parameter and extrapolating the corresponding input variation, it is possible to extrapolate the corresponding instabilities. Such a measurement of the output power is compared on Fig. 6.16 to the clock relative frequency variation. The effect on the Allan variance is moreover added on Fig. 6.17.

As it can be seen, these variations can explain the observed frequency instability. It can be noted that the variation of the transmission on the output window can affect the laser output power by the same effect without having any effect on the clock frequency. However, in this case, the effect on the light transmission are of the same amplitude as for the input window and only affect the extrapolated frequency stability by the same order of magnitude as variations on the input window. Nevertheless, this effect explains that small difference in the behavior of the two curves in Fig. 6.16. From these observations, it can be concluded that the main parameter affecting the long term frequency stability of clocks realized with a cell similar as the one presented here is the variation of light intensity due to change in the windows transmission. This effect is likely due to the condensation of Rb droplets on the cell windows. Indeed, changes due to the Rb vapor density, which could also affect the

Figure 6.17: Allan Variance measured for the MEMS cell without Au micro-disc and calculated influence of the different experimental parameters

cell transmission can only arise from a change in the temperature as the rubidium vapor is always maintained at a saturated vapor density by the presence of metallic droplets. Therefore this effect would be discriminated by the measured cell temperature shift. A potential solution to alkali droplets variation was found with the CSEM patent pending gold micro-discs presented in Chap. 3. The effect of these microstructures will be assessed in the following.

6.2.2 Comparison between measurement with and without gold micro-discs

A cell with Au micro-disc (see Sec. 3.5) was measured in the same setup as above in order to compare the long-term frequency performances with the cell previously tested (without micro-discs). The cell tested here is sealed by anodic bonding, coated with Al_2O_3 and filled by natural Rb microdispensing pills (see Sec. 3.5). The 150 mbar Ar-Ne buffer gas mixture filling presented in Sec. 4.1.3 and 4.1.4 was used.

6.2.2.1 Experimental conditions

Experimental conditions similar to Sec.6.2.1.1 were implemented. The same laser temperature, light intensity, C-field, cell temperature and RF modulation were used. The cell temperature of 95°C, is close to the optimal experimental parameter determine in Sec. 4.1.4 for the Ar-Ne cell. The input laser power of 15 μW is below the optimal power determined in Sec. 4.1.4. However it corresponds to the light intensity that can be expected in a chip-scale atomic clock [198]. The RF frequency was tuned to the ^{85}Rb CPT line around 3.035GHz. In this case, the carrier and laser first modulation sideband are used to create the CPT effect. The RF power was tuned to the determined optimal parameter of 0dBm at the synthesizer output.

6.2.2.2 Measurement of clock parameters

As above, the clock parameters were measured. That is to say, the dependency of the clock frequency to the cell temperature, RF power, optical intensity and C-field intensity. They were measured by varying the target values around the clock operating point and recording the clock frequency. They are presented on Tab. 6.1. The frequency light shift is estimated from Cs data with the same procedure as above. Here, the relative laser frequency stability in extrapolated to be in the order of $3 \cdot 10^{-9}$ because of the $\approx$1.4 GHz excess optical broadening due to the 150 mbar Ar-Ne buffer gas mixture. The order of magnitude of the relative clock frequency instabilities due to the frequency light shift are therefore estimated to be in the order of $2.19 \cdot 10^{-12}$.

Clock parameter	Frequency dependence
Cell temperature shift	$-1.27 \cdot 10^{-9}$/°C
RF power	$2.40 \cdot 10^{-8}$/dB
Intensity light shift	$7.95 \cdot 10^{-9}$/μW ($1.76 \cdot 10^{-11}$cm^2/μW)
C-field intensity shift	$1.16 \cdot 10^{-8}$/mG

Table 6.2: Clock frequency dependance to parameters for a MEMS atomic vapor cells with Au micro-discs filled with natural Rb dispensing micro-pill and sealed by anodic bonding

The measured parameters are in the same order of magnitude as the one measured for the cell filled with ^{87}RbN$_3$ (see Tab. 6.2). The higher C-field dependency can be explained by the higher Zeeman 2nd order frequency dependency for ^{85}Rb (see Tab. 2.1).

6.2.2.3 Long term clock measurement

As for cells without gold micro-discs, the clock frequency was recorded over a long period of time (>15 days) along with the relevant clock parameters. From these data, the Allan variance of the clock as well as the influence of each parameters on the clock frequency stability were computed and are presented on Fig. 6.18.
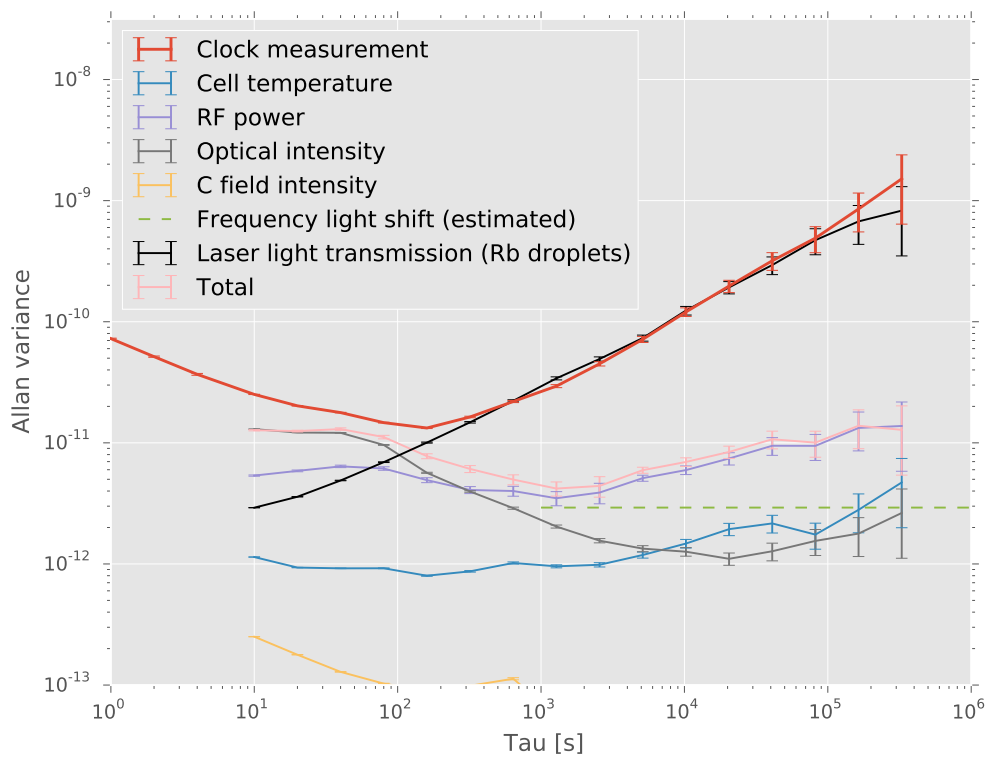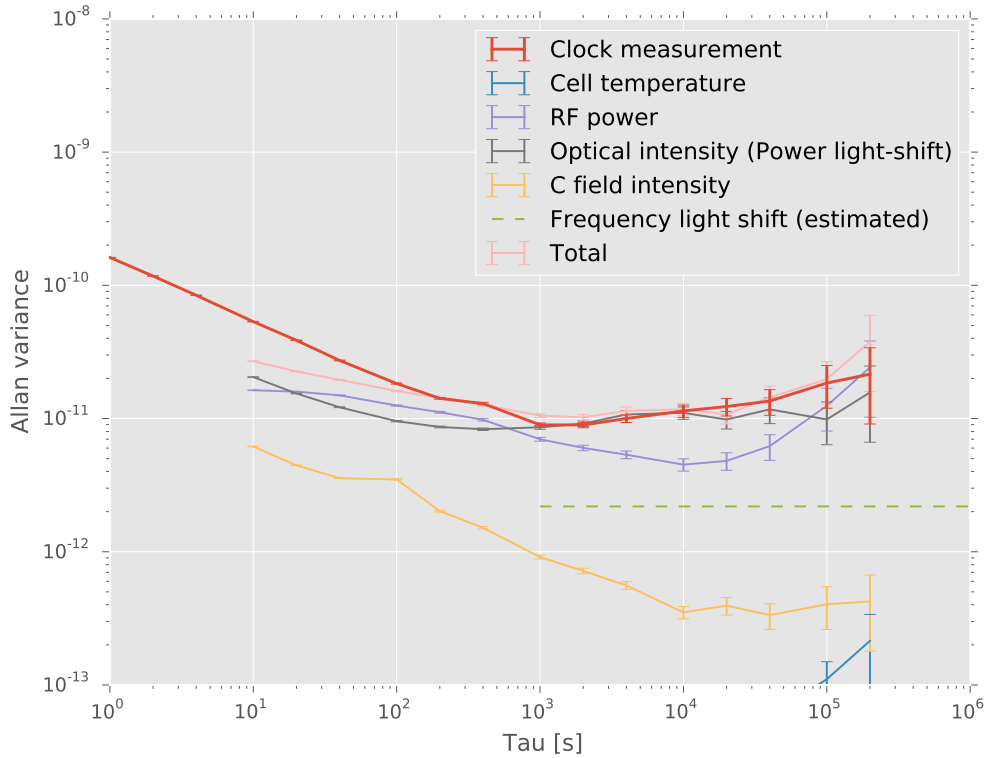

Figure 6.18: Allan Variance measured for the MEMS cell with Au micro-discs and calculated influence of the different experimental parameters

6.2.2.4 Comparison with previous measurement

The Allan variance of the two long-term measurement are compared on Fig. 6.19. Moreover, the clock frequency of the two measurements is compared in Fig. 6.20. The short term frequency stability performance of the clock filled with ^{87}RbN$_3$ UV-decomposition is superior to the performance of the clock realized with natural Rb dispensing pills ($7.3 \cdot 10^{-11}\tau^{-1/2}$ vs $1.6 \cdot 10^{-10}\tau^{-1/2}$). This is in accordance with the expectations derived from the FWHM and contrast measurements realized in Sec. 4.1.4 and 4.1.7 and can be attributed to the better signal to noise ratio achievable with a pure ^{87}Rb selected isotope. Moreover, the short-term frequency stability being lower than the expected values in both cases, it can be assumed that the real noise budget of the laser used here is lower than the estimation realized in Sec. 2.5.2. Finally, the values measured on the cell filled with ^{87}RbN$_3$ UV-decomposition is in agreement with previous measurement realized on similar cells [44].

The long-term performance of the clock made with a cell having a gold micro-disc is, as expected, superior to the performances of the clock without the Au micro-discs. The limitation in the mid to

long-term (>1000 s) of the clock with gold micro-discs can be attributed to variation of the input parameters. Indeed, the optical and RF power variation at this timescale can be identified as the dominant effect for the clock stability (see Fig. 6.18). The cell intrinsic frequency drift, as measured in 0-light shift condition in [33] cannot be accessed in these experimental conditions due to the level of these instabilities. Nevertheless, by comparison with the measurement made on the cell without gold micro-discs, the measurement realized on cell with Au micro-disc does not suffer from instabilities due to tranmission variation which is a good hint that these microstructures remove the effect of frequency instabilities due to migration of the rubidium on the cell window and the implied transmission change. As it can be seen on Fig. 6.19 by comparison of the measurements with the target frequency stability values for a full chip-scale atomic clock, this technology potentially provides a large step forward in order to create a full clock within the specification.
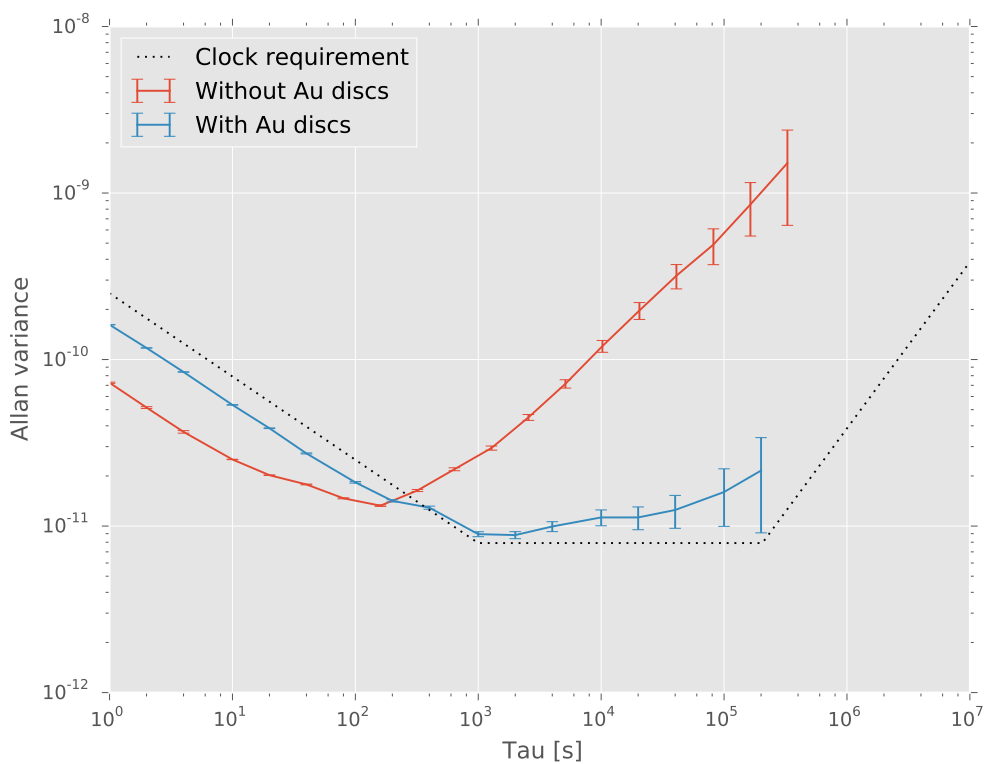
Figure 6.19: Comparison between two clocks realized with cells containing or not gold micro-discs
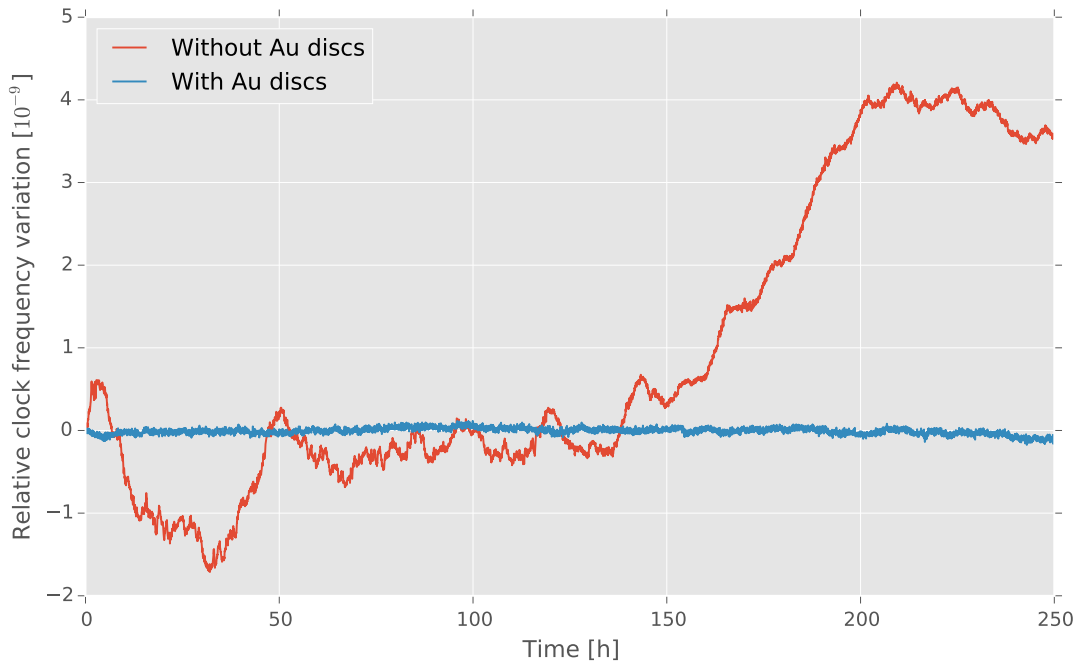
Figure 6.20: Comparison between the two clock frequency along the long-term measurement (100 s averaging)

6.3   Conclusion

The long-term frequency stability of MEMS atomic vapor cells was assessed with the help of a dedicated long-term measurement setup. The main source of long-term instabilities was attributed to light shift in the cell due to transmission variation of the input cell window caused by migration of Rb droplets. As a solution Au micro-discs were proposed and tested. The long term frequency stability were drastically improved on measurement made on cells using this technology. This paves the way for improvement of the full chip-scale atomic clock long-term frequency stability. However, for a formal proof of the effect of Au micro-discs, a direct comparison between identical cells with and without this technology would be required. Finally, as the long-term frequency stability of the clock is now dominated by the light intensity and RF power fluctuations, the next step for use of a MEMS cell in a chip-scale atomic clock would be to minimize these coefficients. For example, Lutwark et al. demonstrated in [6] a minimization of the light-shift by adjusting the RF-power such that the effect of the CPT-participating laser frequencies as well as the unsuppressed carrier and the second-order sidebands on the light-shift coefficient suppress each-other. However this work is left to further study.

7 Conclusion

7.1 Major results

Various technological aspects related to the fabrication and the characterization of MEMS atomic vapor cells for atomic clocks and atomic gyroscopes were addressed in the present thesis. Here recalled are the major results concerning each of these subjects:

- Cu-Cu thermocompression bonding as an innovative sealing method

- Al_2O_3 inner coating for cell lifetime improvement

- Ar-Ne buffer gas mixture for cells filled with Rb dispensing micro-pills

- Au micro-disc as Rb preferential condensation zones

- Preliminary measurement of Xe nuclear spin relaxation

Cu-Cu thermocompression was demonstrated as an effective sealing method for MEMS atomic vapor cells. An optimization of the fabrication and bonding process was first realized. Fabrication of cells sealed with this method was then demonstrated. The vacuum level inside such cells filled by dispensing micro-pills was assessed and an Ar residual pressure value of 2.9±0.4 mbar was measured. Finally, a first CPT signal was measured on such a cell and preliminary tests for the realization of a sapphire cell was reported.

Lifetime measurement on Al_2O_3 coated cells filled with RbN_3 decomposition was realized. This measurement was realized with the help of image analysis of Rb droplets on the cell window surface. The contact angle of these droplets was calibrated thanks to N_2 partial pressure measurements realized with a novel Raman micro-spectroscopy method and a value of 57±6° was found. From these measurements, a minimal quantity of $0.60^{+0.59}_{-0.10}$ μg of metallic rubidium for a desired lifetime of 10 years at 95°C was computed. This quantity corresponds to a total buffer gas pressure of 191^{+186}_{-32} mbar, a pressure compatible with CSAC application.

Ar-Ne was tested as a novel buffer gas mixture for cells filled with dispensing micro-pills. This mixture was developed to circumvent the limitation due reaction of N_2 with the Zr compound of the pills. A buffer gas frequency shift inversion temperature of 89.9°C was measured on a mixture with a target inversion point of 95°C. Moreover, the CPT contrast and linewidth were measured and showed properties compatible with chip-scale atomic clock applications. The suitability of Rb dispensing micro-pills with Ar-Ne buffer gas was therefore confirmed for this application.

CSEM patent pending Au micro-disc were tested as a solution to improve the long-term frequency stability of MEMS atomic vapor cells. Indeed, the main source of long-term instabilities being attributed to light shift in the cell due to transmission variation of the input cell window attributed

to migration of Rb droplets, they were proposed as a solution of preferential condensation spots. The long term frequency stability was drastically improved on cells using this technology.

Finally a preliminary characterization of an RbN_3 filled Al_2O_3 coated anodic bonded MEMS cell filled with ≈ 67 mbar of isotopically selected Xe (50% ^{129}Xe, 50% ^{131}Xe) and 266 mbar of N_2 was realized. The Xe free-induced decay could be measured in a dedicated setup. This measurement paves the way for future measurement of Xe T_2^* relaxation rate.

7.2 Future outlook

The results presented here represent an important step in view of the fabrication of the first Swiss commercial chip-scale atomic clock. Such a device has applications in, for example, GNSS or communication systems. The main criteria for its production are a reduced size, a low production cost, an extended lifetime, a low power consumption and a good short and long-term frequency stability. It is clear that such performances can only be achieved if the cell that is at the heart of the clock meets the requirements. Each of the technologies presented here addresses one on more of these aspects.

Indeed, the characterization work linked to RbN_3 allows to push this promising filling method for low-cost, high-volume production. The work realized on the subject of Al_2O_3 coating allows then to address the lifetime issue of such cells. On the other hand, the characterization work realized on dispensing micro-pill allows to explore this alternative filling solution and to prove its compatibility with CSACs applications. The development of Cu-Cu thermocompression bonding potentially enables, for its part, the fabrication of cells fully made of sapphire and to lower the contamination during the fabrication process. Therefore, this technology addresses the cell long-term intrinsic frequency stability and the lifetime issues. Finally, the characterization work made on Au micro-discs allows to improve the frequency stability of clocks realized with MEMS cells and to address the problem of light-shift induced long-term instabilities due to alkali droplets migration on the cell window. Moreover, this technology could be applied to cells of bigger dimension and could potentially remove the necessity of a cold condensation spot in any type of cell clock.

The future steps for integration of a MEMS atomic vapor cells in an actual device is to select the best combination among these techniques. The implemented cell will benefit from the work presented here in order to meet all necessary requirement for integration in a CSAC. Based on the observation made in the present the following deductions can be drawn:

- The adventage of Cu-Cu thermocompression in term of purity and diversity of bondable materials are compensated by a higher processing complexity and are therefore to be preferred for high end cells used in applications where the cost and production complexity and yield is not an issue. Anodic bonding on the other hand is a more cost-effective method that presents a simpler processing. It is therefore to be preferred for low-cost mass production.

- Whereas dispensing micropills combined with Ar-Ne buffer gas mixture present a solution which meets the requirements for CSAC applications in term of short-term frequency stability and thermal sensitivity, the cell remains of higher dimension and production cost remains higher than for RbN_3. On the other hand, RbN_3 filling combined with Al_2O_3 coating still needs some developments and characterization in order to meet the requirements in term thermal sensitivity. A detailed assessment of each method has therefore to be done prior considering one or the other cell for integration.

- The capability of Au microdiscs to localize the Rb droplets out of the laser lightpath and the indication of their effects on the cell long-term frequency stability of give a clear indication that this technology has a great potential for CSAC application.

Finally, besides their CSACs applications, MEMS atomic vapor cells and their related technologies have applications in other atomic devices and these subjects also benefit of the developments realized

here. The preliminary Xe spin relaxation measurement realized on MEMS cells filled With RbN$_3$ and coated with Al$_2$O$_3$ presented here is a good example of such benefit.

Bibliography

[1] S. Knappe, V. Shah, P. Schwindt, L. Hollberg, J. Kitching, L. Liew, and J. Moreland. A microfabricated atomic clock. *Applied Physics Letters*, 85(9):1460–1462, 2004.

[2] P. Schwindt, S. Knappe, V. Shah, L. Hollberg, J. Kitching, L. Liew, and J. Moreland. Chip-scale atomic magnetometer. *Applied Physics Letters*, 85(26):6409–6411, 2004.

[3] E. Donley, J. Long, T. Liebisch, E. Hodby, T. Fisher, and J. Kitching. Nuclear quadrupole resonances in compact vapor cells: The crossover between the NMR and the nuclear quadrupole resonance interaction regimes. *Physical Review A*, 79(1):013420, 2009.

[4] J. Vanier and C. Mandache. The passive optically pumped Rb frequency standard: the laser approach. *Applied Physics B*, 87(4):1346–1351, 2007.

[5] A. Godone, S. Micalizio, and F. Levi. Pulsed optically pumped frequency standard. *Physical Review A*, 70(2):1–11, 2004.

[6] R. Lutwak, D. Emmons, W. Riley, and R. Garvey. The chip-scale atomic clock - coherent population trapping vs. conventional interrogation. In *34th Annual Precise Time and Time Interval Systems Applications Meeting*, Reston, VA, United States, 2002.

[7] L. Liew, S. Knappe, J. Moreland, H. Robinson, L. Hollberg, and J. Kitching. Microfabricated alkali atom vapor cells. *Applied Physics Letters*, 84(14):2694–2696, 2004.

[8] S. Knappe, V. Gerginov, P. Schwindt, V. Shah, H. Robinson, L. Hollberg, and J. Kitching. Atomic vapor cells for chip-scale atomic clocks with improved long-term frequency stability. *Optics letters*, 30(18):2351–2353, 2005.

[9] L. Liew, J. Moreland, and V. Gerginov. Wafer-level filling of microfabricated atomic vapor cells based on thin-film deposition and photolysis of cesium azide. *Applied Physics Letters*, 90(11):114106, 2007.

[10] R. Lutwak, D. Emmons, T. English, W. Riley, C. Stark, D. Serkland, and G. Peake. The chip-scale atomic clock - recent development progress. In *35th Annual Precise Time and Time Interval (PTTI) Meeting*, pages 467–478, San Diego, CA, United States, 2003.

[11] R. Lutwak, J. Deng, W. Riley, M. Varghese, J. Leblanc, G. Tepolt, M. Mescher, D. Serkland, K. Geib, and G. Peake. The chip-scale atomic clock - low-power physics package. In *36th Annual Precise Time and Time Interval (PTTI) Meeting*, page 14, Washington, DC, United States, 2004.

[12] R. Lutwak, PI Vlitas, M. Varghese, M. Mescher, D. Serkland, and G. Peake. The MAC - A miniature atomic clock. In *International Frequency Control Symposium and Exposition*, pages 752–757, Vancouver, BC, Canada, 2005. IEEE.

[13] R. Lutwak, A. Rashed, D. Serkland, G. Peake, M. Varghese, G. Tepolt, J. Leblanc, and M. Mescher. The miniature atomic clock - pre-production results. In *International Frequency Control Symposium (IFCS), Joint with the 21st European Frequency and Time Forum (EFTF)*, pages 1327–1333, Geneva, Switzerland, 2007. IEEE.

[14] R. Lutwak. The chip-scale atomic clock - recent developments. In *International Frequency Control Symposium (IFCS), Joint with the 23rd European Frequency and Time Forum (EFTF)*, pages 573–577, Besançon, France, 2009. IEEE.

[15] A. Stern, B. Levy, C. Levy, U. Arad, Y. Barash, R. Mann, and A. Gorelik. The NAC - A miniature CPT rubidium clock. In *30th European Frequency and Time Forum (EFTF)*, York, United Kingdom, 2016.

[16] J. DeNatale, P. Stupar, C. Tsai, R. Borwick, K. Garrett, L. Cutler, M. Zhu, J. Berbarian, and R. Newgard. Micromachined Chip-scale Atomic Clock. In *SEM X International Congress & Exposition on Experimental & Applied Mechanics*, Costa Mesa, CA, United States, 2004.

[17] J. DeNatale, R. Borwick, C. Tsai, P. Stupar, Y. Lin, R. Newgard, R. Berquist, and M. Zhu. Compact, low-power chip-scale atomic clock. In *Position, Location and Navigation Symposium*, pages 67–70, Monterey, CA, United States, 2008. IEEE/ION.

[18] A. Douahi, L. Nieradko, J. Beugnot, J. Dziuban, H. Maillote, S. Guerandel, M. Moraja, C. Gorecki, and V. Giordano. Vapour microcell for chip scale atomic frequency standard. *Electronics Letters*, 43(5):279–280, 2007.

[19] A. Douahi, L. Nieradko, J.-C. Beugnot, J. Dziuban, H. Maillote, R. Boudot, S. Guérandel, M. Moraja, C. Gorecki, and V. Giordano. New vapor cell technology for chip scale atomic clock. In *International Frequency Control Symposium (IFCS), Joint with the 21st European Frequency and Time Forum (EFTF)*, pages 58–61, Geneva, Switzerland, 2007. IEEE.

[20] L. Nieradko, C. Gorecki, A. Douahi, V. Giordano, J.-C. Beugnot, J. Dziuban, and M. Moraja. New approach of fabrication and dispensing of micromachined cesium vapor cell. *Journal of Micro/Nanolithography, MEMS, and MOEMS*, 7(3):033013, 2008.

[21] D. Miletic, C. Affolderbach, E. Breschi, C. Schori, G. Mileti, M. Hasegawa, R. Chutani, P. Dziuban, R. Boudot, V. Giordano, and C. Gorecki. Fabrication and spectroscopy of Cs vapor cells with buffer gas for miniature atomic clock. In *24th European Frequency and Time Forum (EFTF)*, pages 1–6, Noordwijk, The Netherlands, 2010.

[22] P. Knapkiewicz, J. Dziuban, R. Walczak, L. Mauri, P. Dziuban, and C. Gorecki. MEMS caesium vapour cell for european micro-atomic-clock. *Procedia Engineering*, 5:721–724, 2010.

[23] C. Gorecki. Development of First European Chip-scale Atomic Clocks:Technologies, Assembling and Metrology. *Procedia Engineering*, 47:898–903, 2012.

[24] V. Maurice, J. Rutkowski, E. Kroemer, S. Bargiel, N. Passilly, R. Boudot, C. Gorecki, L. Mauri, and M. Moraja. Microfabricated vapor cells filled with a cesium dispensing paste for miniature atomic clocks. *Applied Physics Letters*, 110(16):164103, 2017.

[25] V. Maurice, J. Rutkowski, E. Kroemer, S. Bargiel, N. Passilly, R. Boudot, R. Chutani, S. Galliou, and C. Gorecki. Microfabricated vapor cells for miniature atomic clocks based on post-sealing activated cesium dispensers. In *International Frequency Control Symposium (IFCS), Joint with the 31st European Frequency and Time Forum (EFTF)*, pages 636–637, Besançon, France, 2017.

[26] S. Ermak, V. Semenov, E. Piatyshev, A. Kazakin, I. Komarevtsev, E. Velichko, V. Davydov, and M. Petrenko. Microfabricated cells for chip-scale atomic clock based on coherent population trapping: Fabrication and investigation. *St. Petersburg Polytechnical University Journal: Physics and Mathematics*, 1(1):37–41, 2015.

[27] S. Ermak, V. Semenov, M. Petrenko, and E. Pyatyshev. Coherent population trapping in small- and chip-scale ^{87}Rb vapor cells with buffer gas. *International Journal of Modern Physics: Conference Series*, 41(2):1660138, 2016.

[28] M. Fedorov, S. Ermak, M. Petrenko, E. Pyatyshev, and V. Semenov. Investigation of coherent population trapping signals in ^{87}Rb cells with buffer gas. *Journal of Physics: Conference Series*, 769:012046, 2016.

[29] R. Boudot, P. Dziuban, M. Hasegawa, R. K. Chutani, S. Galliou, V. Giordano, and C. Gorecki. Coherent population trapping resonances in Cs-Ne vapor microcells for miniature clocks applications. *Journal of Applied Physics*, 109(1):014912, 2011.

[30] M. Hasegawa, R. K. Chutani, C. Gorecki, R. Boudot, P. Dziuban, V. Giordano, S. Clatot, and L. Mauri. Microfabrication of cesium vapor cells with buffer gas for MEMS atomic clocks. *Sensors and Actuators A: Physical*, 167(2):594–601, 2011.

[31] R. Boudot, X. Liu, P. Abbé, R. Chutani, N. Passilly, S. Galliou, C. Gorecki, and V. Giordano. A high-performance frequency stability compact CPT clock based on a Cs-Ne microcell. *IEEE Transactions on Ultrasonics, Ferroelectrics and Frequency Control*, 59(11):2584–2587, 2012.

[32] M. Hasegawa, R. Chutani, R. Boudot, L. Mauri, C. Gorecki, X. Liu, and N. Passilly. Effects of getters on hermetically sealed micromachined cesium–neon cells for atomic clocks. *Journal of Micromechanics and Microengineering*, 23(5):055022, 2013.

[33] S. Abdullah, C. Affolderbach, F. Gruet, and G. Mileti. Aging studies on micro-fabricated alkali buffer-gas cells for miniature atomic clocks. *Applied Physics Letters*, 106(16):163505, 2015.

[34] A. Dellis, V. Shah, E. Donley, S. Knappe, and J. Kitching. Low helium permeation cells for atomic microsystems technology. *Optics Letters*, 41(12):2775, 2016.

[35] Y. Petremand, C. Schori, R. Straessle, G. Mileti, N. de Rooij, and P. Thomann. Low temperature indium-based sealing of microfabricated alkali cells for chip scale atomic clocks. In *24th European Frequency and Time Forum (EFTF)*, pages Noordwijk, The Netherlands, 2010.

[36] F. Vecchio, V. Venkatraman, H. Shea, T. Maeder, and P. Ryser. Dispensing and hermetic sealing Rb in a miniature reference cell for integrated atomic clocks. *Sensors and Actuators A: Physical*, 172(1):330–335, 2011.

[37] F. Vecchio. *Integrated packaging solutions and hotplates for a miniature atomic clock and other microsystems.* PhD thesis, EPFL, 2013.

[38] R. Straessle, M. Pellaton, Y. Pétremand, D. Briand, C. Affolderbach, G. Mileti, and N. De Rooij. Low-temperature indium hermetic sealing of alkali vapor-cells for chip-scale atomic clocks. In *25th International Conference on Micro Electro Mechanical Systems (MEMS)*, pages 361–364, Paris, France, 2012. IEEE.

[39] R. Straessle, M. Pellaton, C. Affolderbach, Y. Pétremand, D. Briand, G. Mileti, and N. De Rooij. Low-temperature indium-bonded alkali vapor cell for chip-scale atomic clocks. *Journal of Applied Physics*, 113(6):064501, 2013.

[40] R. Straessle, M. Pellaton, C. Affolderbach, Y. Pétremand, D. Briand, G. Mileti, and N. De Rooij. Microfabricated alkali vapor cell with anti-relaxation wall coating. *Applied Physics Letters*, 105(4):043502, 2014.

[41] J. Haesler, T. Overstolz, R. James, J. Pierer, M. Contaldo, D. Ruffieux, and S. Lecomte. Driving an eXtra Small Atomic Resonator with low-power integrated RF frequency and laser locked loops. In *International Frequency Control Symposium (IFCS), Joint with the 13th European Frequency and Time Forum (EFTF)*, San Francisco, CA, United States, 2011. IEEE.

[42] J. Haesler, J. Bennès, T. Overstolz, J. Pierer, R. James, D. Ruffieux, and S. Lecomte. Swiss miniature atomic clock: First prototype and preliminary results. In *26th European Frequency and Time Forum (EFTF)*, pages 312–315, Gothenburg, Sweden, 2012.

[43] J. Haesler, L. Balet, J.-A Porchet, T. Overstolz, J. Pierer, R. James, S. Grossmann, D. Ruffieux, and S. Lecomte. The integrated swiss miniature atomic clock. In *International Frequency Control Symposium (IFCS), Joint with the 15th European Frequency and Time Forum (EFTF)*, pages 579–581, Prague, Czech republic, 2013. IEEE.

[44] T. Overstolz, J. Haesler, G. Bergonzi, A Pezous, P. Clerc, S. Ischer, J. Kaufmann, and M. Despont. Wafer scale fabrication of highly integrated rubidium vapor cells. In *27th International Conference on Micro Electro Mechanical Systems (MEMS)*, pages 552–555, San Francisco, CA, United States, 2014. IEEE.

[45] D. Ruffieux, J. Haesler, L. Balet, T. Overstolz, J. Pierer, R. James, and S. Lecomte. *Frequency References, Power Management for SoC, and Smart Wireless Interfaces*, chapter Towards Portable Miniature Atomic Clocks, pages 83–99. Springer International Publishing, 2014.

[46] M. Perez, U. Nguyen, S. Knappe, E. Donley, J. Kitching, and A. Shkel. Rubidium vapor cell with integrated nonmetallic multilayer reflectors. In *21st International Conference on Micro Electro Mechanical Systems (MEMS)*, pages 790–793, Wuhan, China, 2008. IEEE.

[47] M. Perez, U. Nguyen, S. Knappe, E. Donley, J. Kitching, and A. Shkel. Rubidium vapor cell with integrated Bragg reflectors for compact atomic MEMS. *Sensors and Actuators A: Physical*, 154(2):295–303, 2009.

[48] Y. Pétremand, C. Affolderbach, R. Straessle, M. Pellaton, D. Briand, G. Mileti, and N. De Rooij. Microfabricated rubidium vapour cell with a thick glass core for small-scale atomic clock applications. *Journal of Micromechanics and Microengineering*, 22(2):025013, 2012.

[49] R. Chutani, V. Maurice, N. Passilly, C. Gorecki, R. Boudot, M. Abdel Hafiz, P. Abbé, S. Galliou, J. Rauch, and E. de Clercq. Laser light routing in an elongated micromachined vapor cell with diffraction gratings for atomic clock applications. *Scientific reports*, 5:14001, 2015.

[50] M. Giraud-Carrier. *Perforated Hollow Core Waveguides for Alkali Vapor-cells and Slow Light Devices*. PhD thesis, Brigham Young University, 2016.

[51] M. Giraud-Carrier, T. Decker, and A. Hawkins. Perforated Hollow-Core Waveguide Devices for Atomic Spectroscopy with Alkali Vapor. In *Conference on Lasers and Electro-Optics (CLEO)*, page JTh2A.32., San Jose, CA, United States, 2016.

[52] S. Knappe, O. Alem, D. Sheng, and J. Kitching. Microfabricated Optically-Pumped Magnetometers for Biomagnetic Applications. *Journal of Physics: Conference Series*, 723:012055, 2016.

[53] S. Woetzel, V. Schultze, R. IJsselsteijn, T. Schulz, S. Anders, R. Stolz, and H. Meyer. Microfabricated atomic vapor cell arrays for magnetic field measurements. *Review of Scientific Instruments*, 82(3):033111, 2011.

[54] S. Woetzel, F. Talkenberg, T. Scholtes, R. Ijsselsteijn, V. Schultze, and H. Meyer. Lifetime improvement of micro-fabricated alkali vapor cells by atomic layer deposited wall coatings. *Surface and Coatings Technology*, 221:158–162, 2013.

[55] S. Woetzel, E. Kessler, M. Diegel, V. Schultze, and H. Meyer. Low-temperature anodic bonding using thin films of lithium-niobate-phosphate glass. *Journal of Micromechanics and Microengineering*, 24(9):095001, 2014.

[56] E. Eklund and A. Shkel. Glass Blowing on a wafer level. *Journal of Microelectromechanical Systems*, 16(2):232–239, 2007.

[57] Y. Ji, Q. Gan, L. Wu, and J. Shang. Improvement of polarization lifetime by using wafer-level micro spherical rubidium vapor cells for chip-scale atomic magnetometers. In *30th International Conference on Micro Electro Mechanical Systems (MEMS)*, pages 1018–1021, Las Vegas, United States, 2017. IEEE.

[58] Y. Ji, Q. Gan, L. Wu, and J. Shang. Geometry influence of the micro alkali vapor cell on the sensitivity of the chip-scale atomic magnetometers. In *30th International Conference on Micro Electro Mechanical Systems (MEMS)*, pages 342–345, Las Vegas, United States, 2017. IEEE.

[59] Y. Ji, J. Shang, Q. Gan, and L. Wu. Wafer-level micro alkali vapor cells with anti-relaxation coating compatible with MEMS packaging for chip-scale atomic magnetometers. In *67th Electronic Components and Technology Conference (ECTC)*, Orlando, FL, United States, 2017. IEEE.

[60] K. Tsujimoto, K. Ban, Y. Hirai, K. Sugano, T. Tsuchiya, N. Mizutani, and O. Tabata. On-chip fabrication of alkali-metal vapor cells utilizing an alkali-metal source tablet. *Journal of Micromechanics and Microengineering*, 23(11):115003, 2013.

[61] K. Tsujimoto, Y. Hirai, K. Sugano, T. Tsuchiya, and O. Tabata. Analytical investigation of the feasibility of sacrificial microchannel sealing for Chip-Scale Atomic Magnetometers. *Microsystem Technologies*, 20(3):357–365, 2014.

[62] K. Ban, K. Tsujimoto, Y. Hirai, A. Terao, N. Mizutani, T. Kobayashi, O. Tabata, K. Tsujimoto, Y. Hirai, T. Kobayashi, and O. Tabata. Alkali metal source tablet for vapor cells of atomic magnetometers. In *International Frequency Control Symposium (IFCS), Joint with the 29th European Frequency and Time Forum (EFTF)*, pages 174–179, Denver, CO, United States, 2015. IEEE.

[63] K. Ban, Y. Hirai, K. Tsujimoto, A. Terao, N. Mizutani, T. Kobayashi, and O. Tabata. Characterization of alkali-metal vapor cells fabricated with an alkali-metal source tablet. *Journal of Vacuum Science & Technology A: Vacuum, Surfaces, and Films*, 34(6):061601, 2016.

[64] Y. Hirai, K. Terashima, K. Nakamura, T. Tsuchiya, and O. Tabata. Low temperature, wafer-level process of alkali-metal vapor cells for micro-fabricated atomic clocks. In *19th International Conference on Solid-State Sensors and Actuators and Microsystems (TRANSDUCERS'17)*, pages 431–434, Kaohsiung, Taiwan, 2017.

[65] K. Tsujimoto, Y. Hirai, K. Sugano, T. Tsuchiya, and O. Tabata. Sacrificial microchannel sealing by glass-frit reflow for Chip Scale Atomic Magnetometer. In *24th International Conference on Micro Electro Mechanical Systems (MEMS)*, pages 368–371, Cancun, Mexico, 2011. IEEE.

[66] M. Kwakernaak, S. Lipp, S. McBride, P. Zanzucchi, W. Chan, V. Khalfin, H. An, R. Whaley, B. Willner, and A. Ulmer. Components for batch-fabricated chip-scale atomic clocks. In *36th Annual Precise Time and Time Interval (PTTI) Meeting*, Washington, DC, United States, 2004.

[67] F. Gong, Y. Jau, K. Jensen, and W. Happer. Electrolytic fabrication of atomic clock cells. *Review of Scientific Instruments*, 77(7):711–714, 2006.

[68] S. Radhakrishnan and A. Lal. Alkali metal-wax micropackets for chip-scale atomic clocks. In *13th International Conference on Solid-State Sensors and Actuators and Microsystems (TRANSDUCERS'05)*, volume 1, pages 23–26, Seoul, South Korea, 2005. IEEE.

[69] S. Losev, D. Sevostianov, V. Vassiliev, and V. Velishansky. Production of Miniature Glass Cells with Rubidium for Chip Scale Atomic Clock. *Physics Procedia*, 71:242–246, 2015.

[70] S. Juan, D. Ke, G. Deng-Zhu, W. Zhong, C. Jing, Z. Geng-Min, and C. Xu-Zong. Stable ^{85}Rb micro vapour cells: fabrication based on anodic bonding and application in chip-scale atomic clocks. *Chinese Physics B*, 19(11):110701, 2010.

[71] W. Wei, J. Shang, W. Kuai, S. Qin, T. Wang, and J. Chen. Fabrication of wafer-level spherical Rb vapor cells for miniaturized atomic clocks by a chemical foaming process. In *13th International Conference on Electronic Packaging Technology & High Density Packaging (ICEPT-HDP)*, pages 1639–1641, Guilin, Guangxi, China, 2012. Ieee.

[72] Y. Chen, J. Shang, and Y. Ji. Fabrication of low cost spherical alkali atom vapor cells by combining a low temperature anodic bonding and a Chemical Foaming Process (CFP). In *15th Electronics Packaging Technology Conference (EPTC)*, pages 809–812, Singapore, 2013. IEEE.

[73] Y. Chen, J. Shang, and Y. Ji. Microfabricated low cost wafer-level spherical alkali atom vapor cells for chip-scale atomic clock by a Chemical Foaming Process (CFP). In *14th International Conference on Electronic Packaging Technology (ICEPT)*, pages 720–723, Beijing, China, 2013.

[74] Y. Ji, J. Shang, Y. Chen, and C. Wong. Preparation of a Micro Rubidium vapor cell and its integration in a chip-scale atomic magnetometer. In *64th Electronic Components and Technology Conference (ECTC)*, pages 1488–1491, Orlando, FL, United States, 2014. IEEE.

[75] S. Li, J. Xu, Z. Zhang, L. Zhao, L. Long, and Y. Wu. Integrated physics package of a chip-scale atomic clock. *Chinese Physics B*, 23(7):074302, 2014.

[76] E Arimondo. Coherent population trapping in laser spectroscopy. *Progress in Optics*, 35:257–354, 1996.

[77] J. Vanier and C. Audoin. *The quantum physics of atomic frequency standards*. Adam Hilger, 1989.

[78] D. Steck. Rubidium 87 D line data, January 2015. Version 2.1.5.

[79] G. Breit and I. Rabi. Measurement of nuclear spin. *Physical Review*, 38(11):2082–2083, 1931.

[80] D. Steck. Rubidium 85 D line data, September 2013. Version 2.1.6.

[81] P. Siddons, C. Adams, C. Ge, and I. Hughes. Absolute absorption on the rubidium D lines: comparison between theory and experiment. *Journal of Physics B: Atomic, Molecular and Optical Physics*, 41(15), 2008.

[82] X. Zeng. *Perspectives of Active Atomic Clock Based on Modelocked Semiconductor Laser with Rubidium Vapor Cell Saturable Absorber*. PhD thesis, EPFL, 2015.

[83] M. Rotondaro and G. Perram. Collisional broadening and shift of the rubidium D1 and D2 lines ($5^2S_{12} \rightarrow 5^2P_{12}, 5^2P_{32}$) by rare gases, H_2, D_2, N_2, CH_4 and CF_4. *Journal of Quantitative Spectroscopy and Radiative Transfer*, 57(4):497–507, 1997.

[84] W. Demtröder. *Laser Spectroscopy*. Springer, 2008.

[85] J. Vanier. Atomic clocks based on coherent population trapping: a review. *Applied Physics B*, 81(4):421–442, 2005.

[86] R. Dicke. The effect of collisions upon the Dopper width of spectral lines. *Physical Review*, 89(2):472–473, 1953.

[87] M. Rosenberry, J. Reyes, D. Tupa, and T. Gay. Radiation trapping in rubidium optical pumping at low buffer-gas pressures. *Physical Review A*, 75(2):023401, 2007.

[88] G. Mileti and P. Thomann. Study of the S/N performance of passive atomic clocks using a laser pumped vapour. In *9th European Frequency and Time Forum (EFTF)*, pages 271–276, Besançon, France, 1995.

[89] J. Camparo and J. Coffer. Conversion of laser phase noise to amplitude noise in a resonant atomic vapor: The role of laser linewidth. *Physical Review A*, 59(1):728–735, 1999.

[90] J. Kitching, S. Knappe, M. Vukicevic, L. Hollberg, R. Wynands, and W. Weidmann. A microwave frequency reference based on VCSEL-driven dark line resonances in Cs vapor. *IEEE Transactions on Instrumentation and Measurement*, 49(6):1313–1317, 2000.

[91] S. Micalizio, A. Godone, F. Levi, and J. Vanier. Spin-exchange frequency shift in alkali-metal-vapor cell frequency standards. *Physical Review A - Atomic, Molecular, and Optical Physics*, 73(3):1–5, 2006.

[92] O. Kozlova. *Caractérisation d'une horloge à piégeage cohérent de population dans une vapeur thermique de césium. Principaux effets pouvant affecter la stabilité de fréquence à moyen-long terme.* PhD thesis, Université Paris VI Pierre et Marie Curie, 2012.

[93] J. Vanier, R. Kunski, N. Cyr, J. Y. Savard, and M. Têtu. On hyperfine frequency shifts caused by buffer gases: Application to the optically pumped passive rubidium frequency standard. *Journal of Applied Physics*, 53(8):5387–5391, 1982.

[94] B. Bean and R. Lambert. Temperature dependence of hyperfine density shifts. IV. ^{23}Na, ^{39}K, and ^{85}Rb in He, Ne, Ar, and N_2 at low temperatures. *Physical Review A*, 13(1):492–494, 1976.

[95] S. Timoshenko and S. Woinowsky-Krieger. *Theory of plates and shells*. McGraw-Hill Book Company, 1959.

[96] F. Levi, A. Godone, and J. Vanier. The light shift effect in the coherent population trapping cesium maser. *IEEE Transactions on Ultrasonics, Ferroelectrics and Frequency Control*, 47(2):466–470, 2000.

[97] Z. Wang. Review of chip-scale atomic clocks based on coherent population trapping. *Chinese Physics B*, 23(3):030601, 2014.

[98] S. Knappe, R. Wynands, J. Kitching, H. Robinson, and L. Hollberg. Characterization of coherent population-trapping resonances as atomic frequency references. *Journal of the Optical Society of America B*, 18(11):1545, 2001.

[99] D. Miletic, C. Affolderbach, M. Hasegawa, R. Boudot, C. Gorecki, and G. Mileti. AC Stark-shift in CPT-based Cs miniature atomic clocks. *Applied Physics B*, 109(1):89–97, 2012.

[100] J. Norton. Permeation of gases through solids. *Journal of Applied Physics*, 28(1):34–39, 1957.

[101] K. Liu, W. Zhang, W. Chen, K. Li, F. Dai, F. Cui, X. Wu, G. Ma, and Q. Xiao. The development of micro-gyroscope technology. *Journal of Micromechanics and Microengineering*, 19(11):113001, 2009.

[102] E. Donley. Nuclear magnetic resonance gyroscopes. In *SENSORS*, Waikoloa, HI, United States, 2010. IEEE.

[103] E. Kanegsberg. A nuclear magnetic resonance (NMR) gyro with optical magnetometer detection. In *Laser Inertial Rotation Sensors*, volume 0157, pages 73–80, San Diego, USA, 1978. SPIE.

[104] T. Walker and W. Happer. Spin-exchange optical pumping of noble-gas nuclei. *Reviews of Modern Physics*, 69(2):629–642, 1997.

[105] H. Dehmelt. Modulation of a light beam by precessing absorbing atoms. *Physical Review*, 105(6):1924–1925, 1957.

[106] A. Bloom. Principles of Operation of the Rubidium Vapor Magnetometer. *Applied Optics*, 1(1):61–68, 1962.

[107] B. Grover. Noble-Gas NMR Detection through Noble-Gas-Rubidium Hyperfine Contact Interaction. *Physical Review Letters*, 40(6):391–392, 1978.

[108] K. Jousten. *Handbook of Vacuum Technology*, volume 24. John Wiley & Sons, 2008.

[109] V. Altemose. Helium diffusion through glass. *Journal of Applied Physics*, 32(7):1309–1316, 1961.

[110] R. Frueholz and M. Wun-Fogle. Lamp reliability studies for improved satellite rubidium frequency standard. In *13th Annual Precise Time and Time Interval (PTTI) Meeting*, Washington, DC, United States, 1981.

[111] C. Volk, R. Frueholz, T. English, T. Lynch, and W. Riley. Lifetime and Reliability of Rubidium Discharge Lamps for Use in Atomic Frequency Standards. In *38th Annual Symposium on Frequency Control*, pages 387 – 400, Philadelphia, PA, United States, 1984. IEEE.

[112] R. Cook and R. Frueholz. An improved rubidium consumption model for discharge lamps used in rubidium frequency standards. In *42nd Annual Frequency Control Symposium*, pages 525–531, Baltimore, MD, United States, 1988. IEEE.

[113] A. Dellis, S. Knappe, E. Donley, and J. Kitching. Low He Permeation Cells for CSACs. In *International Frequency Control Symposium (IFCS), Joint with the 19th European Frequency and Time Forum (EFTF)*, Denver, CO, United States, 2015. IEEE.

[114] J. Neuman, P. Wang, and A. Gallagher. Robust high-temperature sapphire cell for metal vapors. *Review of Scientific Instruments*, 66(4):3021–3023, 1995.

[115] K.R. Williams, K. Gupta, and M. Wasilik. Etch rates for micromachining processing-Part II. *Journal of Microelectromechanical Systems*, 12(6):761–778, 2003.

[116] C. Addison. *The chemistry of the liquid alkali metals*. John Wiley and Sons, 1984.

[117] H. Borgstedt and C. Mathews. *Applied chemistry of the alkali metals*. Plenum Publishing Corporation, 1987.

[118] J. Songster and A. D. Pelton. The Al-Rb (Aluminum-Rubidium) system. *Journal of phase equilibria*, 14(3):367–367, 1993.

[119] A Pelton. The Au-Rb (Gold-Rubidium) system. *Bulletin of Alloy Phase Diagrams*, 7(2):139–142, 1986.

[120] A. Pelton. The Cu-Rb (Copper-Rubidium) System. *Bulletin of Alloy Phase Diagrams*, 7(1):28, 1986.

[121] A. Pelton and S. Larose. The In-Rb (Indium-Rubidium) System. *Journal of phase equilibria*, 12(3):377–379, 1991.

[122] J. Sangster and C. Bale. The Rb-Sn (Rubidium-Tin) System. *Journal of Phase Equilibria*, 19(1):82–84, 1998.

[123] A. Van Wieringen and N. Warmoltz. On the permeation of hydrogen and helium in single crystal silicon and germanium at elevated temperatures. *Physica*, 22(6-12):849–865, 1956.

[124] V. Lindroos, S. Franssila, M. Tilli, M. Paulasto-Krockel, A. Lehto, T. Motooka, and V. Airaksinen. *Handbook of Silicon Based MEMS Materials and Technologies*. Elsevier, 2009.

[125] S. Theppakuttai, D. Shao, and S. Chen. Localized Laser Transmission Bonding for Microsystem Fabrication and Packaging. *Journal of Manufacturing Processes*, 6(1):24–31, 2004.

[126] G. Wallis and D. Pomerantz. Field assisted glass-metal sealing. *Journal of Applied Physics*, 40(10):3946–3949, 1969.

[127] P. Ramm, J. Lu, and M. Taklo. *Handbook of Wafer Bonding*. John Wiley & Sons, 2012.

[128] H. Henmi, S. Shoji, Y. Shoji, K. Yoshimi, and M. Esashi. Vacuum packaging for microsensors by glass-silicon anodic bonding. *Sensors and Actuators A: Physical*, 43(1–3):243–248, 1994.

[129] S. Mack, H. Baumann, U. Gösele, H. Werner, and R. Schlögl. Analysis of Bonding-Related Gas Enclosure in Micromachined Cavities Sealed by Silicon Wafer Bonding. *Journal of The Electrochemical Society*, 144(3):1106–1111, 1997.

[130] T. Corman, P. Enoksson, and G. Stemme. Low-pressure-encapsulated resonant structures with integrated electrodes for electrostatic excitation and capacitive detection. *Sensors and Actuators A: Physical*, 66(1–3):160–166, 1998.

[131] S. Mack, H. Baumann, and U. Gosele. Gas tightness of cavities sealed by silicon wafer bonding. In *10th Annual International Workshop on Micro Electro Mechanical Systems*, pages 488–493, Nagoya, Japan, 1997. IEEE.

[132] S. Tanaka, S. Matsuzaki, M. Mohri, A Okada, H. Fukushi, and M. Esashi. Wafer-level hermetic packaging technology for MEMS using anodically-bondable LTCC wafer. In *24th International Conference on Micro Electro Mechanical Systems (MEMS)*, pages 376–379, Cancun, Mexico, 2011. IEEE.

[133] A. Berthold, L. Nicola, P. M. Sarro, and M. J. Vellekoop. Glass-to-glass anodic bonding with standard IC technology thin films as intermediate layers. *Sensors and Actuators A: Physical*, 82(1):224–228, 2000.

[134] T. Hsu. *MEMS Packaging*. IET, 2004.

[135] M. Baum, C. Jia, M. Haubold, M. Wiemer, A. Schneider, H. Rank, A. Trautmann, and T. Gessner. Eutectic wafer bonding for 3-D integration. In *Electronics System Integration Technology Conference (ESTC)*, Berlin, Germany, 2010.

[136] N. Lorenz. *Laser-based packaging of micro-devices*. PhD thesis, Heriot-Watt University, 2011.

[137] N. Budraa, H. Jackson, M. Barmatz, W. Pike, and J. Mai. Low pressure and low temperature hermetic wafer bonding using microwave heating. In *2th International Conference on Micro Electro Mechanical Systems (MEMS)*, pages 490–492, Orlando, FL, United States, 1999. IEEE.

[138] H. Noh, K.-S. Moon, A. Cannon, P. Hesketh, and C. Wong. Wafer bonding using microwave heating of parylene intermediate layers. *Journal of Micromechanics and Microengineering*, 14(4):625, 2004.

[139] H. Noh, K. Moon, A. Cannon, P. Hesketh, and C. Wong. Wafer bonding using microwave heating of parylene for MEMS packaging. In *54th Electronic Components and Technology Conference (ECTC)*, volume 1, pages 924–930, Las Vegas, NV, United States, 2004.

[140] Y. Cheng, L. Lin, and K. Najafi. Localized silicon fusion and eutectic bonding for MEMS fabrication and packaging. *Journal of Microelectromechanical Systems*, 9(1):3–8, 2000.

[141] Y. Cheng, L. Lin, and K. Najafi. A hermetic glass-silicon package formed using localized aluminum/silicon-glass bonding. *Journal of Microelectromechanical Systems*, 10(3):392–399, 2001.

[142] Y. Cheng, W. Hsu, K. Najafi, C. Nguyen, and L. Lin. Vacuum packaging technology using localized aluminum/silicon-to-glass bonding. *Journal of Microelectromechanical Systems*, 11(5):556–565, 2002.

[143] L. Lin. MEMS post-packaging by localized heating and bonding. *IEEE Transactions on Advanced Packaging*, 23(4):608–616, 2000.

[144] Hsueh-An Y., Mingching W., and Weileun F. Localized induction heating solder bonding for wafer level MEMS packaging. *Journal of Micromechanics and Microengineering*, 15(2):729–732, 2005.

[145] C. Hu, S. Wen, C. Hsu, C. Chang, C. Shih, and H. Lee. Solder bonding with a buffer layer for MOEMS packaging using induction heating. *Microsystem Technologies*, 12(10-11):1011–1014, 2006.

[146] M. Chen, X. Yi, L. Yuan, Z. Gan, and S. Liu. Rapid and Selective Induction Heating for Sensor Packaging. In *6th International Conference on Electronic Packaging Technology*, pages 1–4, Dameisha, Shenzhen, China, 2005. IEEE.

[147] M. Chen, L. Yuan, and S. Liu. Research on low-temperature anodic bonding using induction heating. *Sensors and Actuators A: Physical*, 133(1):266–269, 2007.

[148] M.J. Wild, A. Gillner, and R. Poprawe. Locally selective bonding of silicon and glass with laser. *Sensors and Actuators A: Physical*, 93(1):63–69, 2001.

[149] M. Wild, A. Gillner, and R. Poprawe. Advances in silicon-to-glass bonding with laser. In Uwe F. W. Behringer and Deepak G. Uttamchandani, editors, *Microelectronic and MEMS Technologies*, volume SPIE 4407, pages 135–141, Edinburgh, United Kingdom, 2001.

[150] A. Gillner, M. Wild, and R Poprawe. Laser bonding of micro-optical components. In *Laser Micromachining for Optoelectronic Device Fabrication*, volume SPIE 4941, pages 112–120, Bruges, Belgium, 2003. SPIE.

[151] A. Gillner, J. Holtkamp, C. Hartmann, A. Olowinsky, J. Gedicke, K. Klages, L. Bosse, and A. Bayer. Laser applications in microtechnology. *Journal of Materials Processing Technology*, 167(2-3):494–498, 2005.

[152] E. Haberstroh, W. Hoffmann, R. Poprawe, and F. Sari. Laser transmission joining in microtechnology. *Microsystem Technologies*, 12(7):632–639, 2006.

[153] U. Mescheder, M. Alavi, K. Hiltmann, C. Lietzau, C. Nachtigall, and H. Sandmaier. Local laser bonding for low temperature budget. *Sensors and Actuators A: Physical*, 97-98:422–427, 2002.

[154] C. Luo and L. Lin. The application of nanosecond-pulsed laser welding technology in MEMS packaging with a shadow mask. *Sensors and Actuators A: Physical*, 97-98:398–404, 2002.

[155] A. Tan and F. Tay. Localized laser assisted eutectic bonding of quartz and silicon by Nd:YAG pulsed-laser. *Sensors and Actuators A: Physical*, 120(2):550–561, 2005.

[156] A. Tan, F. Tay, and J. Zhang. Characterization of localized laser assisted eutectic bonds. *Sensors and Actuators A: Physical*, 125(2):573–585, 2006.

[157] W. Watanabe, S. Onda, T. Tamaki, and K. Itoh. Direct joining of glass substrates by 1 kHz femtosecond laser pulses. *Applied Physics B*, 87(1):85–89, 2006.

[158] W. Watanabe, S. Onda, T. Tamaki, K. Itoh, and J. Nishii. Space-selective laser joining of dissimilar transparent materials using femtosecond laser pulses. *Applied Physics Letters*, 89(2):021106, 2006.

[159] A. Määttänen, V. Hautala, and J. Vihinen. Precise online auto-focus system in high speed laser micromachining applications. *Physics Procedia*, 39:807–813, 2012.

[160] H. Lundén, T. Kumpulainen, A. Määttänen, and J. Vihinen. Novel glass welding technique for hermetic encapsulation. In *5th Electronics System-integration Technology Conference (ESTC)*, Helsinki, Finland, 2014. IEEE.

[161] R. Witte, H. Herfurth, and S. Heinemann. Laser Joining of Glass with Silicon. In *Photon Processing in Microelectronics and Photonics*, volume SPIE 4637, pages 487–495, San Jose, CA, United States, 2002. SPIE.

[162] L. Bosse, A. Schildecker, A. Gillner, and R. Poprawe. High quality laser beam soldering. *Microsystem Technologies*, 7(5-6):215–219, 2002.

[163] C.-H Lee, H. Guo, S. Radhakrishnam, A. Lal, C. Szekely, T. McClellan, and A. Pisano. A batch fabricated rubidium–vapor resonance cell for chip-scale atomic clocks. In *Solid-State Sensors, Actuators and Microsystems Workshop*, Hilton Head Island, SC, United States, 2005.

[164] L. Hackspill. Recherches sur les métaux alcalins. *Annales de chimie et de physique*, 28:613–696, 1913.

[165] L. Hackspill. Sur quelques propriétés des métaux alcalins. *Helvetica Chimica Acta*, 11(1):1003–1026, 1928.

[166] L. Hackspill. Sur une nouvelle préparation du rubidium et du caesium. In *Comptes rendus hebdomadaires des séances de l'Académie des sciences*, pages 106–107, Paris, France, 1835. Gauthier-Villars (Paris).

[167] M. Bick, H. Prinz, and A. Steinmetz. *Ullmann's Encyclopedia of Industrial Chemistry*, chapter Cesium and Cesium Compounds. Wiley Online Library, 2000.

[168] G. Missout and J. Vanier. Pressure and Temperature Coefficients of the More Commonly Used Buffer Gases in Rubidium Vapor Frequency Standards. *IEEE Transactions on Instrumentation and Measurement*, 24(2):180–184, 1975.

[169] A. Pelton. The Ca-Rb (Calcium-Rubidium) system. *Bulletin of Alloy Phase Diagrams*, 6(1):37, 1985.

[170] J. Ma, A. Kishinevski, Y.-Y. Jau, C. Reuter, and W. Happer. Modification of glass cell walls by rubidium vapor. *Physical Review A*, 79(4):042905, 2009.

[171] M. Hirashima and M. Asano. Effects of Caesium Vapour upon the Target Glass of Image Orthicons. In D. McMullan E. Kahan J.D. McGee and B. L. Morgan, editors, *Fourth Symposium on Photo-Electronic Image Devices*, volume 28A, pages 309–321, London, United Kingdom, 1969. Academic Press.

[172] M. Bouchiat, P. Jacquier, M. Lintz, and A. Papoyan. Electrical conductivity of glass and sapphire cells exposed to dry cesium vapor. *Applied Physics B*, 68(6):1109–1116, 1999.

[173] S. Rothman, T. Marcuso, L. Nowicki, P. Baldo, and A. McCormick. Diffusion of Alkali Ions in Vitreous Silica. *Journal of the American Ceramic Society*, 65(11):578–582, 1982.

[174] M. Stephens, R. Rhodes, and C. Wieman. Study of wall coatings for vapor-cell laser traps. *Journal of Applied Physics*, 76(6):3479, 1994.

[175] K. Chen, A. Fan, and R. Reif. Microstructure examination of copper wafer bonding. *Journal of Electronic Materials*, 30:331–335, 2001.

[176] K. Chen, A. Fan, C.-S. Tan, R. Reif, and Y. Wen. Microstructure evolution and abnormal grain growth during copper wafer bonding. *Applied Physics Letters*, 81(20):3774–3776, 2002.

[177] K. Chen, A. Fan, C. Tan, and R. Reif. Temperature and duration effects on microstructure evolution during copper wafer bonding. *Journal of Electronic Materials*, 32(12):1371–1374, 2003.

[178] R. Tadepalli and C. Thompson. Quantitative characterization and process optimization of low-temperature bonded copper interconnects for 3-D integrated circuits. In *International Interconnect Technology Conference (IITC)*, pages 36–38, Burlingame, CA, United States, 2003. IEEE.

[179] K. Chen, C. Tan, A. Fan, and R. Reif. Morphology and Bond Strength of Copper Wafer Bonding. *Electrochemical and Solid-State Letters*, 7(1):G14, 2004.

[180] C. Tan, K. Chen, A. Fan, and R. Reif. The Effect of Forming Gas Anneal on the Oxygen Content in Bonded Copper Layer. *Journal of Electronic Materials*, 34(12):1598–1602, 2005.

[181] K. Chen, A. Fan, C. Tan, and R. Reif. Bonding parameters of blanket copper wafer bonding. *Journal of Electronic Materials*, 35(2):230–234, 2006.

[182] C.-T. Ko and K.-N. Chen. Wafer-level bonding/stacking technology for 3D integration. *Microelectronics Reliability*, 50(4):481–488, 2010.

[183] E. Kroemer, M. Abdel Hafiz, V. Maurice, B. Fouilland, C. Gorecki, and R. Boudot. Cs vapor microcells with Ne-He buffer gas mixture for high operation-temperature miniature atomic clocks. *Optics Express*, 23(14):18373, 2015.

[184] B. Kobrin, V. Fuentes, S. Dasaradhi, R. Yi, R. Nowak, and J. Chinn. Molecular Vapor Deposition – An Improved Vapor-Phase Deposition Technique of Molecular Coatings for MEMS Devices. In *SEMI Technical Symposium: Innovations in Semiconductor Manufacturing (SEMICON West)*, San Francisco, CA, United States, 2004.

[185] R Matthey, W Moreno, F Gruet, P Brochard, S Schilt, and G Mileti. Rb-stabilized laser at 1572 nm for CO_2 monitoring. *Journal of Physics: Conference Series*, 723:012034, 2016.

[186] W. Weber, M. Zanini-Fisher, and M. Pelletier. Using Raman Microscopy to Detect Leaks in Micromechanical Silicon Structures. *Applied Spectroscopy*, 51(1):123–129, 1997.

[187] S. Karlen, J. Gobet, T. Overstolz, J. Haesler, and S. Lecomte. Quantitative micro-Raman spectroscopy for partial pressure measurement in small volumes. *Applied Spectroscopy*, 71(12):2707–2713, 2017.

[188] P. Bernath. *Spectra of Atoms and Molecules*. Oxford University Press, 2005.

[189] S. Karlen, G. Buchs, T. Overstolz, N. Torcheboeuf, E. Onillon, J. Haesler, and D. Boiko. MEMS atomic vapor cells for gyroscope applications. In *International Frequency Control Symposium (IFCS), Joint with the 31st European Frequency and Time Forum (EFTF)*, pages 315–316, Besançon, France, 2017.

[190] G. Buchs, S. Karlen, T. Overstolz, N. Torcheboeuf, E. Onillon, J. Haesler, and D. Boiko. Nuclear spin decoherence time in MEMS atomic vapor cells for applications in quantum technologies. In *4th International Conference on Quantum Technologies (ICQT)*, Moscow, Russia, 2017.

[191] S. Karlen, J. Gobet, T. Overstolz, J. Haesler, and S. Lecomte. Lifetime assessment of RbN_3-filled MEMS atomic vapor cells with Al_2O_3 coating. *Optics express*, 25(3):2187–2194, 2017.

[192] S. Karlen, J. Gobet, T. Overstolz, and J. Haesler. Non-destructive MEMS atomic vapor cells characterization by Raman spectroscopy and image analysis. In *29th European Frequency and Time Forum (EFTF)*, York, United Kingdom, 2016. IEEE.

[193] K. Zhao and Z. Wu. Atomic resonance behavior in laser-induced Rb atom desorption - The effect of ambient gas atoms and molecules. *Physics Letters A*, 299(1):73–78, 2002.

[194] F. Gruet, A. Al-Samaneh, E. Kroemer, L. Bimboes, D. Miletic, C. Affolderbach, D. Wahl, R. Boudot, G. Mileti, and R. Michalzik. Metrological characterization of custom-designed 894.6 nm VCSELs for miniature atomic clocks. *Optics express*, 21(5):5781–92, 2013.

[195] C. Affolderbach, R. Matthey, F. Gruet, T. Bandi, and G. Mileti. Realisation of a compact laser-pumped Rubidium frequency standard with $<1\mathrm{x}10^{-12}$ stability at 1 second. In *24th European Frequency and Time Forum (EFTF)*, Noordwijk, The Netherlands, 2010. IEEE.

[196] J. Di Francesco, F. Gruet, C. Schori, C. Affolderbach, R. Matthey, G. Mileti, Y. Salvadé, Y. Petremand, and N. De Rooij. Evaluation of the frequency stability of a VCSEL locked to a micro- fabricated Rubidium vapour cell. In *Semiconductor Lasers and Laser Dynamics IV*, page 77201T, Brussels, Belgium, 2010. SPIE.

[197] D. Miletic. *Light-shift and temperature-shift studies in atomic clocks based on coherent population trapping*. PhD thesis, Université de Neuchâtel, 2013.

[198] J. Haesler, K. Kautio, L. Balet, S. Karlen, T. Overstolz, and B. Gallinet. Ceramic based flat form factor miniature atomic clock physics package (C-MAC). In *ESA Workshop on Microwave Technology and Techniques (MTT)*, Noordwijk, The Netherlands, 2017.

Sylvain KARLEN

Av. d'Echallens 123
1004 Lausanne
+41 79 248 78 11
sylvain.karlen@alumni.epfl.ch
12.12.1987
Swiss
Single

Applied Physics engineer, specialized in microsystems, optics and time and frequency

Education

University of Neuchâtel, Time and Frequency Laboratory (LTF), *Switzerland*

2014 - 2017	PhD in Physics

> Thesis entitled *"Fabrication and characterization of MEMS alkali vapor cells used in chip-scale atomic clocks and other atomic devices"*
> Work performed at CSEM SA under the supervision of the University of Neuchâtel

EPFL, Swiss Federal Institute of Technology in Lausanne, *Switzerland*

2012 – 2014	Master of Science in Applied Physics

> Master project *"Experimental demonstration of a secure relativistic coin flipping protocol"* performed at the University of Geneva in the Group of Applied Physics : Optics
> Several semester experimental projects carried out in quantum optics and photonics subjects

2008 – 2012	Bachelor of Science in Physics

Gymnase de Beaulieu, *Lausanne*

2003 – 2007	Swiss Federal Maturity in Mathematics and Physics orientation

Work experience

CSEM S.A., (R&D), Time and Frequency department, Systems division, *Neuchâtel, Switzerland*

01/2018 (present)	R&D Engineer
08/2014 – 12/2017	PhD Student

> Conception, design and micro-fabrication of MEMS atomic vapor cells for chip-scale atomic clocks
> Atomic spectroscopy, SEM and micro-Raman characterization of such cells
> Contribution to the packaging of a LTCC atomic chip-scale clock with optical waveguides
> Participation to diverse other R&D projects
> Participation to conferences and publishing of scientific articles

08/2013 - 01/2014	R&D engineering trainee

ESA – ESTEC, RF Equipment and Technology Section (TEC-EFE), *Noordwijk, the Netherlands*

08/2017 - 11/2017	PhD student trainee

> Characterization work on Galileo satellite passive hydrogen maser
> Automatization of a time transfer protocol between ESOC and ESTEC for UTC(ESA) calculation

EPFL, Swiss Federal Institute of Technology in Lausanne, *Switzerland*

09/2009 - 07/2014	Teaching assistant (Tutor)

> Responsible for a group of students during the exercise sessions of numerical and general physics

Technical and computer skills

Scientific and technical competences:

Design of (micro) systems (*e.g.* thermal, electrical and mechanical design, packaging, testing)

Expertise in photonics, integrated optics and lase physics (*e.g.* design of optical systems, fibre optics, laser frequency lock, atomic spectroscopy)

Design and fabrication process of MEMS and semiconductor devices (*e.g.* photolithography, lift-off, sputtering, wafer bonding) and use of specific characterization techniques (*e.g.* SEM, optical microscopy, Raman spectroscopy, mechanical and electrical characterization)

Good knowledge in analogic and digital electronics

General laboratory skills (*e.g.* optics, vacuum technology, RF electronics, cryogenics)

Computer skills:
> Programming: Python, C/C++/C#, Matlab, LabVIEW
> CAD and IC design : SolidWorks, DraftSigth, Menthor graphics
> Numerical simulation: Comsol
> Graphical design; Photoshop, Adobe Illustrator, InkScape
> Office and OS : MS office, Latex, Windows, Linux, Mac OS X

Scientific publications

Peer reviewed articles:
> S. Karlen, J. Gobet, T. Overstolz, J. Haesler, and S. Lecomte, "Quantitative micro-Raman spectroscopy for partial pressure measurement in small volumes," *Appl. Spectrosc.*, 2017.
> S. Karlen, J. Gobet, T. Overstolz, J. Haesler, and S. Lecomte, "Lifetime assessment of RbN_3-filled MEMS atomic vapor cells with Al_2O_3 coating," *Opt. Express*, vol. 25, no. 3, pp. 2187–2194, 2017.

Conference proceedings:
> S. Karlen et al., "MEMS atomic vapor cells sealed by Cu-Cu thermocompression bonding," *European Frequency and Time Forum & International Frequency Control Symposium (EFTF-IFCS)*, 2017.
> S. Karlen et al. "MEMS atomic vapor cells for gyroscope applications," *European Frequency and Time Forum & International Frequency Control Symposium (EFTF-IFCS)*, 2017.
> J. Haesler, et al., "Low-Power and Low-Profile Miniature Atomic Clock Ceramic based flat form factor miniature atomic clock physics package (C-MAC)," *European Frequency and Time Forum & International Frequency Control Symposium (EFTF-IFCS)*, 2017.
> J. Haesler et al., "Ceramic based flat form factor miniature atomic clock physics package (C-MAC). In 6th International Colloquium on Scientific and Fundamental Aspects of GNSS / Galileo, 2017
> G. Buchs, et al., "Nuclear spin decoherence time in MEMS atomic vapor cells for applications in quantum technologies," *Fourth International Conference on Quantum Technologies (ICQT)*, 2017.
> S. Karlen et al., "Cu-Cu thermocompression bonding as an innovative sealing method for MEMS atomic vapor cells," *ESA Workshop on Microwave Technology and Techniques (MTT)*, 2017.
> J. Haesler, et al., "Ceramic based flat form factor miniature atomic clock physics package (C-MAC)," *ESA Workshop on Microwave Technology and Techniques (MTT)*, 2017.
> S. Karlen, et al., "Non-destructive MEMS atomic vapor cells characterization by Raman spectroscopy and image analysis," *European Frequency and Time Forum, (EFTF)*, 2016.

Languages

French	**mother tongue**
English	**C1**
German	**B1**

Hobbies

Mountain sports:	Rock climbing, alpinism and skiing (Member of the Swiss alpine club)
Cinema:	Science-fiction, comedy, adventure